

國立交通大學

材料科學與工程學系

博士論文

介孔洞二氧化矽超低介電薄膜在積體電路技術之
應用

Mesoporous Silica Thin Films as Ultralow- k Dielectrics for ULSI
Applications

研究生：陳致宇

指導教授：潘扶民 教授

張 立 教授

中華民國九十五年七月

介孔洞二氧化矽超低介電薄膜在積體電路技術之應用

Mesoporous Silica Thin Films as Ultralow- k Dielectrics for ULSI Applications

研究生：陳致宇

Student: Jr-Yu Chen

指導教授：潘扶民 教授

Advisors: Prof. Fu-Ming Pan

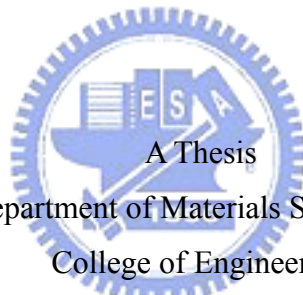
張 立 教授

Prof. Li Chang

國立交通大學

材料科學與工程學系

博士論文



Submitted to Department of Materials Science and Engineering
College of Engineering

National Chiao Tung University

in partial Fulfillment of the Requirements

for the Degree of

Doctor of Philosophy

in

Materials Science and Engineering

July 2005

Hsinchu, Taiwan, Republic of China

中華民國九十五年七月

介孔洞二氧化矽超低介電薄膜在積體電路技術之應用

研究生：陳致宇

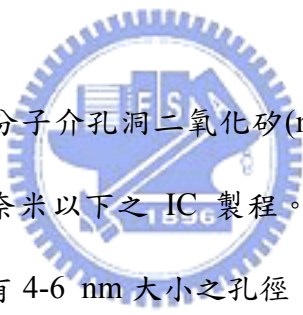
指導教授：潘扶民 教授

張 立 教授

國立交通大學

材料科學與工程學系博士班

摘 要



本研究將進行有機模板分子介孔洞二氧化矽(mesoporous SiO₂)超低介電薄膜之製備，期能應用於半導體 65 奈米以下之 IC 製程。研究中乃利用模板分子之自我組裝(self-assembly)方式製備出具有 4-6 nm 大小之孔徑，且呈高規則孔道結構的介孔洞二氧化矽薄膜。由於其孔洞呈現規則性排列且孔洞尺寸具有一致性，因此經由此種方法可以製作出具有較佳之機械性質與介電特性的多孔性二氧化矽薄膜。此薄膜若再經由三甲基矽化作用(trimethylsilylation)之疏水化改質，不但可使多孔性二氧化矽薄膜具有 $k \sim 2.1$ 之超低介電常數，且因薄膜內有序性的微孔洞結構，以及孔洞表面上的三甲基矽化結構所產生的回彈效應(spring-back effect)，因此利用此一方式亦能有效地提升多孔性二氧化矽薄膜之機械強度。

此外，本研究亦對於多孔性二氧化矽薄膜以及其與非晶相氮化碳化矽(α -SiC:H)薄膜的疊層，進行薄膜應力方面的研究與探討。在多孔性二氧化矽薄膜的製備過程中，因薄膜內所含有的溶劑與模板分子，於烘烤與煅燒階段不斷地被移除，使得二氧化矽薄膜產

生體積收縮，衍生張應力。研究中發現，薄膜經過 HMDS (Hexamethyldisilazane) 蒸氣處理後，在回彈效應的作用下，薄膜張應力將可得以舒緩。非晶相氫化碳化矽薄膜本身具高壓應力，與多孔性二氧化矽薄膜形成疊層後，藉由應力補償與其鍍膜時烷氧基化誘生的回彈效應，同樣可舒緩多孔性二氧化矽薄膜的張應力，甚至形成輕微的壓應力。

最後，金屬化後多孔性二氧化矽薄膜疊層的熱穩定性與化學結構的穩定性亦將被探討。研究結果顯示以 HMDS 蒸氣處理過後，薄膜內的三甲基矽化結構其熱穩定性可達 400°C，並能持續穩定保持極佳之疏水性與介電特性達 50 天以上。然而經高溫(>400°C) 退火後，三甲基矽化薄膜的化學結構被發現有劣化的現象，位於孔洞表面上的甲基會因高溫而產生裂解脫附。不過在高溫退火之下並未發現到有金屬離子穿隧過 Ta(N) 阻障層到介電層中，薄膜疊層也顯示具有很好的附著性。本研究之結果顯示經三甲基矽化改質後的多孔性二氧化矽薄膜具有卓越的熱與介電穩定性，利於將來進行銅鑲嵌之後段製程整合。



Mesoporous Silica Thin Films as Ultralow- k Dielectrics for ULSI Applications


Student: Jr-Yu Chen

Advisors: Prof. Fu-Ming Pan

Prof. Li Chang

Department of Materials Science and Engineering
National Chiao Tung University

Abstract



Organic templated mesoporous silica ultralow- k films were prepared as the intermetal dielectric for sub-65 nm IC technology nodes. The films have a pore size of 4-6 nm and a well-ordered pore channel structure formed in a self-assembly process of the surfactant. The self-assembled molecularly templated mesoporous silica films have better mechanical and dielectric properties than many other porous low- k dielectrics, because of an ordered pore structure and uniform pore size distribution. Trimethylsilylation of the mesoporous silica thin film by HMDS vapor treatment greatly improves the hydrophobicity of the mesoporous dielectric, and a dielectric constant ~ 2.1 can be obtained for the thin film. Also, trimethylsilylation effectively increases the mechanical strength of the mesoporous silica films. Moreover, the nanoindentation measurements are discussed in terms of the pore microstructure of the mesoporous silica network and the spring-back effect due to the trimethylsilyl groups in the nanopores.

The film stress of the mesoporous silica thin film and the α -SiC:H/mesoporous silica

film stack was also studied. The as-calcined mesoporous silica exhibits a tensile film stress caused by its contraction during bake and calcination. Trimethylsilylation of the mesoporous film causes the spring-back effect, thereby improving its mechanical properties and relieving the tensile stress. Deposition of a plasma-assisted α -SiC:H layer on the mesoporous silica thin film can also relieve the tensile stress, and even cause the film stack to become compressively stressed. This finding follows from the stress compensation and alkoxylation during the deposition of α -SiC:H.

Finally, the thermal and chemical stability of the Cu/nitrided Ta/mesoporous silica film stack on the Si wafer are considered. The trimethylsilylated mesoporous silica dielectric is thermally stable up to 400°C, and its dielectric and chemical properties are reliably maintained over 50 days. Decomposition of trimethylsilyl groups on the pore surface becomes significant at temperatures of over 400°C. However, when the metallized film stack is annealed at temperatures of over 400°C, the film stack exhibits only slight delamination between layers and retains smooth interfaces. A bias-temperature stress test of the metallized film stack reveals little Cu diffusion into the mesoporous dielectric layer. This work reveals that the trimethylsilylated mesoporous silica thin film is thermally and electrically stable up to 400°C, and is a candidate ultralow- k dielectric for incorporation into a Cu damascene structure.

Acknowledgements

首先，謹將本文獻予曾經在論文研究這條路上關心我、協助我的恩人與機關團體。

學生由衷地感謝指導恩師 潘扶民教授與 張立教授這些年來的循循善誘與諄諄教誨，成功地引導學生進入半導體製程與奈米技術的世界，並以材料分析作為工具，藉以了解並解決 IC 製程整合上的問題。雖然在從事研究的過程中，經歷了許多挫折及困難，但相信也正因這一路漫長艱辛的歷練，造就我日後不畏艱難、勇往直前的人格特質。同時，我也在整個學習過程中，獲得更多的邏輯判斷、規劃組織以及團隊合作的經驗，謹此致以最誠摯的謝意。

感謝台大化工系 萬本儒教授、交大奈米所 許鈺宗教授、交大材料系 呂志鵬教授，以及國家奈米實驗室 吳文發副主任等學位口試委員的親臨指教，使學生無論於研究或啟發上獲益良多。尤其甚者，於颱風天的日子，卻仍願特此為學生無畏風雨、撥冗前來， 萬教授更是遠從台北而來，學生由衷的感謝之情，非文筆所能言喻。

要感謝的人真得很多，僅以「謝天」二字，實難表吾心。俊安、德富、厚光、懋榮、俊宏、種發學長，摯友志光，明雁、仕寅、岳翰、志坤、智偉等諸位學弟妹，在我身心備受試煉的艱熬，諸位的心泉支援，即時滋潤了我枯竭的心靈。儘管對實驗室無所貢獻，卻仍不遺不棄，衷心地大感激！

協宗、大憲、吉峯學弟們以及宜芳學妹，感謝你們這段時間的幫忙與支持。崎嶇難行的研究路途，因各位的存在與陪伴，不知不覺已儼然轉化為一康莊大道。協宗、宜芳學弟妹，學長表達謝意的同時，也祝福兩位能順利完成研究、取得學位。當獲得口試委員們的一致認同時，內心一股油然而生的踏實與喜悅之情，相信在不久的將來，你們一定也能感受到的。

亦同時感謝 國家奈米元件實驗室的諸位， 蔡增光博士、柏偉、瓊姿、君惠、美玲、穩俊、志遠、子綾以及恩宗，謝謝各位先進們在半導體製程與分析技術上所給予的援助與建言。另外，感謝 行政院國家科學委員會提供研究經費與獎助學金，以及國立清華大學化學系 趙桂蓉教授於原材料與技術的提供，使能順利完成此一研究，誠摯感謝。並感謝系辦余蕙馨與張麗娟小姐在行政方面所提供的協助與建議，使學生於學位考試的申請與進行，得以順利完成。

最後，感謝我最摯愛的家人，有你們在精神上的支持與鼓勵，我得以心無旁騖，順利完成學位。



Contents

Abstract (in Chinese).....	i
Abstract (in English).....	iii
Acknowledgements.....	v
Contents.....	vii
Table Caption.....	x
Figure Caption.....	xi
List of Symbols.....	xvii
Chapter 1 Introduction.....	1
1.1 Multilayer Interconnect Technology for Scaling.....	2
1.2 Urgent Development of Intermetal Dielectric Materials with Ultralow Dielectric Constant.....	4
1.3 Organization of Thesis.....	8
Chapter 2 Literature Review.....	10
2.1 Electrical Performance of Low- <i>k</i> Dielectrics.....	10
2.2 Potential Solutions for Creating Low- <i>k</i> Dielectrics.....	14
2.2.1 Fluorosilicate Glass (FSG).....	14
2.2.2 Silsesquioxane (SSQ)-based Materials.....	16
2.2.3 Low- <i>k</i> Polymers.....	19
2.2.4 Amorphous Carbon.....	25
2.2.5 Carbon-doped Silica.....	25
2.2.6 Porous Materials.....	27
2.2.6.1 Porous Silsesquioxanes.....	28
2.2.6.2 Xerogel and Aerogel.....	28

2.2.6.3 Surfactant-Templated Mesoporous Materials.....	29
2.3 Integration Studies of Porous Dielectric Films.....	32
2.3.1 Mechanical Properties of Porous Materials.....	32
2.3.2 Copper Metallization.....	33
2.3.3 Plasma Etching.....	35
Chapter 3 Experimental.....	36
3.1 Preparation of Surfactant-Templated Mesoporous Silica.....	36
3.1.1 Preparation of Silica Precursor.....	36
3.1.2 Deposition of Mesoporous Silica Thin Film.....	38
3.1.3 Self-assembly of Surfactant.....	39
3.1.4 Hydrophobisation.....	39
3.2 Metallization of Mesoporous Silica Thin Films.....	41
3.3 Characterization of Mesoporous Silica Thin Films.....	41
3.3.1 Electrical Characteristics.....	41
3.3.2 Mechanical Strength.....	43
3.3.3 Film Stress.....	45
3.3.4 Chemical and Thermal Stability.....	47
3.3.5 Microstructure, Surface Morphology and Optical Properties.....	47
Chapter 4 Dielectric Properties and Hydrophobicity of Surfactant-Templated Mesoporous Silica Films.....	49
4.1 Relationship between Surfactant and Dielectric Constant of Mesoporous Silica Thin Films.....	49
4.2 Methylsilylation of Mesoporous Silica Thin Films.....	53
4.3 Improvement of Dielectric Characteristics by Hydrogen Plasma Treatment.....	59
4.4 Summary.....	61

Chapter 5 Mechanical Strength of Surfactant-Templated Mesoporous Silica Thin Films.....	63
5.1 Microstructure of Mesoporous Silica Thin Films.....	64
5.2 Effect of Methylsilylation on the Mechanical Properties.....	71
5.3 Summary.....	74
Chapter 6 Effect of Trimethylsilylation on the Film Stress of Mesoporous Silica Ultralow- <i>k</i> Film Stacks.....	76
6.1 Volume Expansion by Spring-back Effect.....	77
6.2 Film Stress Relaxation.....	81
6.3 Thermomechanical Characteristics.....	86
6.4 Summary.....	89
Chapter 7 Thermal Stability of Trimethylsilylated Mesoporous Silica Thin Film as an Ultra-low <i>k</i> Dielectric in Copper Interconnects.....	90
7.1 Trimethylsilylation of the Mesoporous Silica Thin Film.....	90
7.2 Thermal and Chemical Stability of the Cu/Ta(N)-metallized Mesoporous Silica Film Stack.....	96
7.3 Summary.....	103
Chapter 8 Conclusions and Suggestions for Future Work.....	105
8.1 Conclusions.....	105
8.2 Suggestions for Future Work.....	106
References.....	108
Vita.....	121

Table Caption

Table 1.1	Requirements for low- <i>k</i> IMD materials.....	5
Table 1.2	Defining IMD characteristics.....	6
Table 2.1	Electronic polarizability of some typical chemical bonds.....	12
Table 2.2	Classification of low- <i>k</i> candidates.....	15
Table 2.3	Available SSQ-based low- <i>k</i> materials.....	17
Table 2.4	Material properties for SSQ-based matrix resins.....	18
Table 2.5	Some of the polymers for low- <i>k</i> application.....	23
Table 2.6	Intrinsic properties of SiLK™ low- <i>k</i> dielectric.....	24
Table 2.7	Film properties of carbon-doped oxide and PECVD oxide.....	26
Table 2.8	Various surfactant/inorganic (S/I) mesostructures and the reaction conditions.....	31
Table 3.1	Precursor composition for the molecularly templated silica films.....	37
Table 4.1	FTIR absorption bands in the mesoporous silica films.....	54
Table 4.2	FTIR absorption bands in the O-H stretching region.....	55
Table 5.1	Elastic modulus for low- <i>k</i> materials.....	74
Table 6.1	Coefficients of thermal expansion for various interconnect materials.....	88
Table 7.1	Dielectric properties of the as-calcined and HMDS treated mesoporous silica thin films after 400°C anneal.....	95

Figure Caption

Figure 1.1	Complexity of MOSFET-based chips versus time.....	1
Figure 1.2	Schematic diagram of a typical interconnect element.....	3
Figure 1.3	Calculated gate and interconnect delay versus technology generation.....	4
Figure 2.1	Bruggeman's effective medium approximation showing dielectric constant versus porosity for oxide and a low- <i>k</i> material.....	13
Figure 2.2	Chemical structures of FSG with (a) low fluorine concentration, (b) high fluorine concentration.....	16
Figure 2.3	Ladder (a) and cage (b-d) structures of Silsesquioxanes.....	17
Figure 2.4	Chemical structures of (a) polyarylethers; (b) FLARE™; (c) Teflon AF; (d) divinylsiloxane-benzocyclobutene (DVS-BCB); (e) SiLK.....	20
Figure 2.5	Chemical structure of PTFE and PVDF.....	21
Figure 2.6	SEM cross-sectional image of Cu-SiLK™ interconnect structure.....	24
Figure 2.7	Synthesis process of aerogel and xerogel (S: shrinkage).....	29
Figure 2.8	Ordered and disordered phases of mesostructured materials.....	30
Figure 2.9	Schematic representation of a dual damascene copper metallization structure with porous low- <i>k</i> dielectric.....	33
Figure 3.1	Process flow for the molecularly templated silica films.....	37
Figure 3.2	Acid-catalyzed hydrolysis proceeds by bimolecular nucleophilic displacement reactions.....	38
Figure 3.3	Stages of the spin-coating process.....	39
Figure 3.4	Self-assembly of surfactants and soluble silica.....	40
Figure 3.5	Preparation scheme for metal-insulator-semiconductor (MIS) capacitor structure (a), and Al shadow mask with dot array patterns (b).....	42

Figure 3.6	Schematic representation of (a) a cross section of a surface through an indentation, and (b) the load-displacement relationships.....	44
Figure 3.7	Principle of film stress measurement by optical reflection method.....	46
Figure 4.1	FTIR spectra of (a) the as-baked film, and the as-baked film followed by calcination at (b) 200°C for 90 min, (c) 300°C for 90 min, (d) 350°C for 30 min, and (e) 400°C for 30 min.....	50
Figure 4.2	Dielectric constant and refractive index of the mesoporous silica thin films as a function of surfactant/TEOS molar ratio.....	51
Figure 4.3	Surface morphologies of the mesoporous silica thin films prepared from a precursor P123/TEOS in molar ratios of (a) 0.01, (b) 0.02 and (c) 0.03.....	52
Figure 4.4	FTIR spectra of mesoporous silica thin film; (a) as-calcined film, (b) as-calcined film after HMDS treatment for 30 min, (c) as-calcined TMCS (10% molar ratio) derivatized film, (d) TMCS derivatized film after HMDS treatment for 30 min.....	54
Figure 4.5	Trimethylsilylation of mesoporous silica thin films by HMDS. A HMDS molecule reacts with surface silanol group, to give a silylated pore surface and $(\text{CH}_3)_3\text{SiNH}_2$, which then reacts with a Si-OH group yielding NH_3 as byproduct.....	55
Figure 4.6	Thermal desorption spectra of H_2O ($m/e = 18$) for the as-calcined (dash line) and the HMDS treated (solid line) mesoporous silica thin films.....	56
Figure 4.7	High frequency (1 MHz) $C-V$ characteristic and leakage current of mesoporous silica film after HMDS treatment.....	57
Figure 4.8	Capacitance-voltage curve and leakage current for TMCS derivatized mesoporous silica film.....	58
Figure 4.9	FTIR spectra of mesoporous silica thin film; (a) as-calcined film, (b) as-calcined	

	film after H ₂ plasma treatment for 3 min, (c) H ₂ plasma treated film after HMDS treatment for 20 min, (d) H ₂ plasma treated film after HMDS treatment for 30 min.....	60
Figure 4.10	Schematic representation of trimethylsilylated mesoporous silica thin films subjected to hydrogen plasma treatment.....	60
Figure 4.11	FTIR spectra of HMDS treated mesoporous silica thin film after H ₂ plasma treatment for (a) 0 min, (b) 2 min, (c) 3 min, and (d) 10 min.....	61
Figure 5.1	Cross-sectional SEM image of as-calcined mesoporous silica thin film. The thickness is estimated to be about 300 nm.....	64
Figure 5.2	AFM image of the as-calcined mesoporous silica thin film. The image size is 5 x 5 μm ²	65
Figure 5.3	XRD spectra of the as-calcined mesoporous silica thin films; (a) without TMCS derivatization, (b) with 10% molar ratio TMCS, (c) with 15% TMCS, and (d) 25% TMCS. For clarity, the XRD spectrum of the mesoporous film with 5% TMCS is not shown. The (100) diffraction peak of the silica film with 5% TMCS is situated at 2θ = 1.42, and has an intensity and a fwhm comparable to the mesoporous film with 10% TMCS.....	66
Figure 5.4	SEM images of the as-calcined mesoporous silica thin films with 15% molar ratio TMCS derivatization. The magnification is (a) 500x and (b) 3000x.....	67
Figure 5.5	Curve fitting for the absorption band of the Si-O-Si asymmetric stretching modes of as-calcined mesoporous silica film without TMCS modification, assuming a Gaussian shape for the resolved peaks. For comparison, the absorption band of the TMCS (5%) derivatized film is also shown in the figure (dashed line). A broader and symmetric absorption feature at the low wavenumber side can be clearly seen for the TMCS derivatized film. The	

	broader feature is ascribed to the presence of cyclosiloxane like rings as explained in the discussion.....	69
Figure 5.6	Asymmetric stretching motion of the (a) TO_3 and (b) TO_4 modes of the intertetrahedral oxygen in the SiO_2 network.....	69
Figure 5.7	FTIR spectra of mesoporous silica thin films in the range of the Si-O-Si asymmetric stretching modes; (a) the as-calcined film, (b) the as-calcined film after the HMDS treatment for 30 min, (c) the as-calcined film with 5% TMCS, (d) the as-calcined film with 10% TMCS. The small peak at 1258 cm^{-1} is due to the Si- CH_3 stretching mode.....	71
Figure 5.8	Young's modulus and hardness of the mesoporous silica thin films; (a) the as-calcined film, (b) the as-calcined film after the HMDS treatment for 30 min, (c) the as-calcined TMCS (5% molar ratio) derivatized film, (d) the TMCS (5% molar ratio) derivatized film after the HMDS treatment for 30 min, (e) the as-calcined TMCS (10% molar ratio) derivatized film, (f) the TMCS (10% molar ratio) derivatized film after the HMDS treatment for 30 min.....	72
Figure 6.1	Cross-sectional SEM image of the mesoporous $SiO_2/\alpha\text{-SiC:H/mesoporous } SiO_2$ sandwich film structure.....	78
Figure 6.2	Film thickness of the mesoporous SiO_2 thin film after various steps of the film preparation process. The film thickness was examined by cross-sectional SEM. Also shown in the figure is the film stress of the mesoporous film.....	79
Figure 6.3	FTIR spectrum of the mesoporous silica thin film after the HMDS treatment for 30 minutes. The inset shows the absorption band around 1258 cm^{-1} , which is due to the Si- $(CH_3)_3$ stretch vibration, for (a) the as-calcined film, and for the mesoporous silica after the HMDS treatment for (b) 30 min, (c) 60 min, (d) 90 min.....	80

Figure 6.4	Elastic modulus and hardness of the mesoporous silica thin films as a function of the HMDS exposure time.....	81
Figure 6.5	Film stress of the mesoporous SiO ₂ as a function of surfactant/TEOS molar ratio.....	82
Figure 6.6	Film stresses of three mesoporous SiO ₂ /α-SiC:H film stacks at different preparation stages. The α-SiC:H capping layer was deposited at (a) 150°C, (b) 250°C, and (c) 350°C.....	83
Figure 6.7	Film stress and refractive index of the α-SiC:H film deposited on the Si wafer as a function of deposition temperature.....	84
Figure 6.8	Auger intensity ratios of carbon to oxygen and to silicon for mesoporous silica/α-SiC:H film stacks as a function of α-SiC:H deposition temperature....	85
Figure 6.9	Stress as a function temperature during thermal cycling for mesoporous silica film on Si and Ge substrates; (a) the as-calcined film and (b) the methylsilylated film.....	87
Figure 7.1	Thermal desorption spectra of CH ₄ (m/e = 16) for the as-calcined (dash line) and the HMDS treated (solid line) mesoporous silica thin films.....	91
Figure 7.2	(a) FTIR spectra of (i) the as-calcined film, (ii) the HMDS treated film, and the HMDS treated film annealed at (iii) 300°C, (iv) 400°C, (v) 500°C, and (vi) 600°C. The enlarged absorption spectrum windows for the C-H stretching and the Si-O-Si asymmetric stretching modes are shown in (b) and (c), respectively.....	92
Figure 7.3	AES depth profiles of the SiN _x /Cu/Ta(N)/mesoporous SiO ₂ /Si film stack after (a) 450°C annealed and (b) 600°C annealed.....	97
Figure 7.4	Cross-sectional TEM images of the metallized film stack after (a) 450°C annealed and (b) 600°C annealed.....	99

Figure 7.5 High resolution TEM micrograph of the Ta₂C nanocrystal at the Ta(N)/mesoporous silica interface of the sample annealed at 600°C for 30 minutes.....100

Figure 7.6 C-V traces of Cu-MIS capacitors stressed under various gate biases at 150°C for 15 min: (a) unannealed capacitor, and (b) capacitor annealed at 400°C.....102



List of Symbols

A : the contact area of an indenter

C : the capacitance of material

D : the line spacing of interconnect

E : the elastic modulus of material

E_i : the elastic modulus of the indenter

E_r : the reduced elastic modulus

E_s : the Young's modulus of the bare substrate

H : the hardness of material

J : the leakage current density

L : the length of the metal line

M : the line thickness of interconnect

M_f : the biaxial modulus of the film

N : the number of molecules per m^3

P : the line pitch of interconnect

P_c : the power consumption

P_m : the maximum load

R : the resistance of material

S : the stiffness of material

T_g : the glass transition temperature

V : the supply voltage

V_f : the total volume of the film

V_p : the volume of the pores

W : the line width of interconnect



f : the operational frequency

f_d : the fraction of gates that switch during a clock period

g : the gradient of the stress as a function of temperature

h_c : the contact depth

h_m : the maximum depth of the elastic deformation under load

h_s : the displacement of the surface at the perimeter of the contact

k : the relative dielectric constant of the insulator

k_{bulk} : the bulk dielectric constant

k_{eff} : the effective dielectric constant

n : the refractive index of the film

r : the radius of the curvature of the wafer after the thin film was deposited

r_0 : the radius of the curvature of the wafer before the thin film was deposited

t_f : the thickness of the film

t_s : the thickness of the substrate

Π : the porosity of the film

α_e : the electronic polarization

α_f : the coefficients of thermal expansion of the film

α_i : the ionic polarization

α_o : the orientation polarization

α_s : the coefficients of thermal expansion of the substrate

β : a geometrical constant of the indenter

ε : a geometrical constant

ε_0 : the permittivity of a vacuum

ε_m : the permittivity of the solid matrix of the film

ε_p : the permittivity of the internal pores of the film



ϵ_r : the relative permittivity of material

θ : the X-ray diffraction angle

ν : the Poisson's ratio of material

ν_i : the Poisson's ratio of the indenter

ν_s : the Poisson ratio of the bare substrate

ρ : the metal resistivity

σ_f : the film stress



Chapter 1

Introduction

In recent decades, the field of solid-state electronics has a revolution and development continues at a remarkable rate. This development relies on the continuous miniaturization of devices in circuits [1], as forecasted by Intel's cofounder Gordon Moore, allowing more components and more functions to be installed per unit area (Fig. 1.1). Now, the field of solid-state electronics is approaching the era of nanodevices, whose dimensions are under 100 nm. However, the over-shrinkage of integrated circuits has forced chipmakers to face difficult challenges, such as RC delay, crosstalk and power dissipation. The preferred strategy now is to introduce a copper conductor accompanied by an insulator with a low dielectric constant (low- k). This chapter offers an overview of the development of integrated circuit technology. The characteristics and requirements of low- k materials are also briefly considered here.

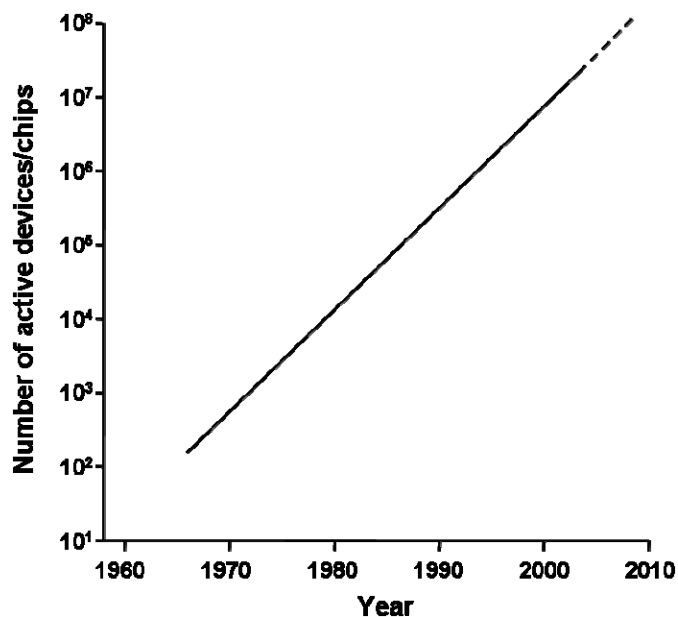


Figure 1.1 Complexity of MOSFET-based chips versus time [1].

1.1 Multilayer Interconnect Technology for Scaling

Developing ultralarge-scale integrated circuits (ULSI) depends on a scaling law, which states that the scaling of transistor dimensions increases chip performance. When the production dimensions of the transistor are reduced, the chip size can be reduced. Therefore, semiconductor makers can cut the unit manufacturing price by increasing the number of chips on each wafer. For instance, the 0.13 μm Pentium 4 processor, a product of Intel Corp., has 55 million transistors, and that becomes twice as many as a 90 nm microprocessor. Also, the scaling law establishes the possibility of increasing signal processing speed and power consumption as the transistor size is reduced. The industry remarkably doubles the device speed roughly every two years by reducing the gate size of the transistor by about 30% at every technology node. Faster, smaller, higher performance and lower cost ICs support the profitability of the industry today.

However, the effective speed of a device is controlled not only by the intrinsic gate delay but also by the rate of signal propagation through the metal interconnect. Modern integrated circuit devices contain millions of transistors electrically connected by millions of wires fabricated on the wafer. These connect wires, or “interconnects”, transfer the signal between the transistors, and make the devices perform logic operations. Previously, the interconnect signal delay, characterized by the resistance-capacitance (RC) time constant, was negligible. As the device dimensions are reduced below 250 nm, the performance of ICs, historically limited by the characteristics of the transistors, has become limited by the interconnect RC delay, crosstalk and power consumption. Figure 1.2 presents a simple model of the cross-sectional view of multilevel interconnects, where P represents the line pitch, W the line width, D the line spacing and M the line thickness [2]. The thickness of the insulators above and below the interconnect is assumed to be equal. In a simple first-order model, the

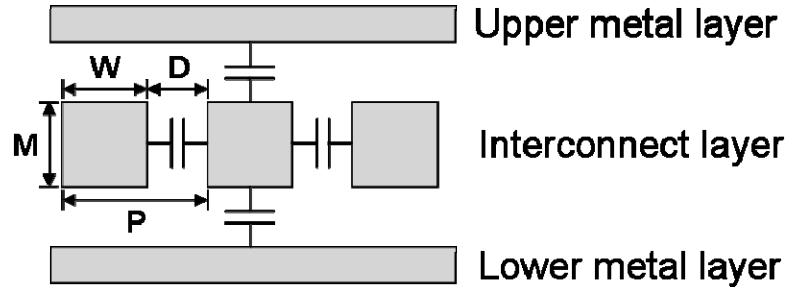


Figure 1.2 Schematic diagram of a typical interconnect element [2].

RC time delay is given by Eq. (1.1).

$$RC = 2\rho k\varepsilon_0 \left(4L^2 / P^2 + L^2 / M^2 \right), \quad (1.1)$$

where ρ is the metal resistivity, ε_0 the vacuum permittivity, k the relative dielectric constant of the insulator and L the length of the line. The power consumption (P_c) of a circuit is given by,

$$P_c = \left(\frac{1}{2} \right) f_d C V^2 f, \quad (1.2)$$

where C is the total on-capacitance, V the supply voltage, f the operational frequency and f_d the fraction of gates that switch during a clock period. The drop in the size of features greatly increases the RC delay time, but introducing metallic interconnects with low electrical resistivity and intermetal dielectrics (IMD) with low permittivity can overcome the scaling hurdles. Additionally, reducing k , and therefore C , reduces the power dissipation (P_c) and makes the device more efficient, as indicated by Eq. (1.2). Until recently, all interconnects were fabricated using aluminum ($\rho \doteq 2.66 \mu\Omega\text{-cm}$) as the conductor and silicon dioxide ($k=4.0$) as the dielectric. Figure 1.3 reveals that the introduction of Cu ($\rho \doteq 1.67 \mu\Omega\text{-cm}$) and low- k dielectric ($k=2.0$) improves the RC delay at each IC technology node [3]. At the 0.25 μm technology node and beyond, using Cu and a low- k dielectric greatly reduces the delay time to about 65% lower than that obtained using Al and SiO_2 at the sub-0.1 μm technology node.

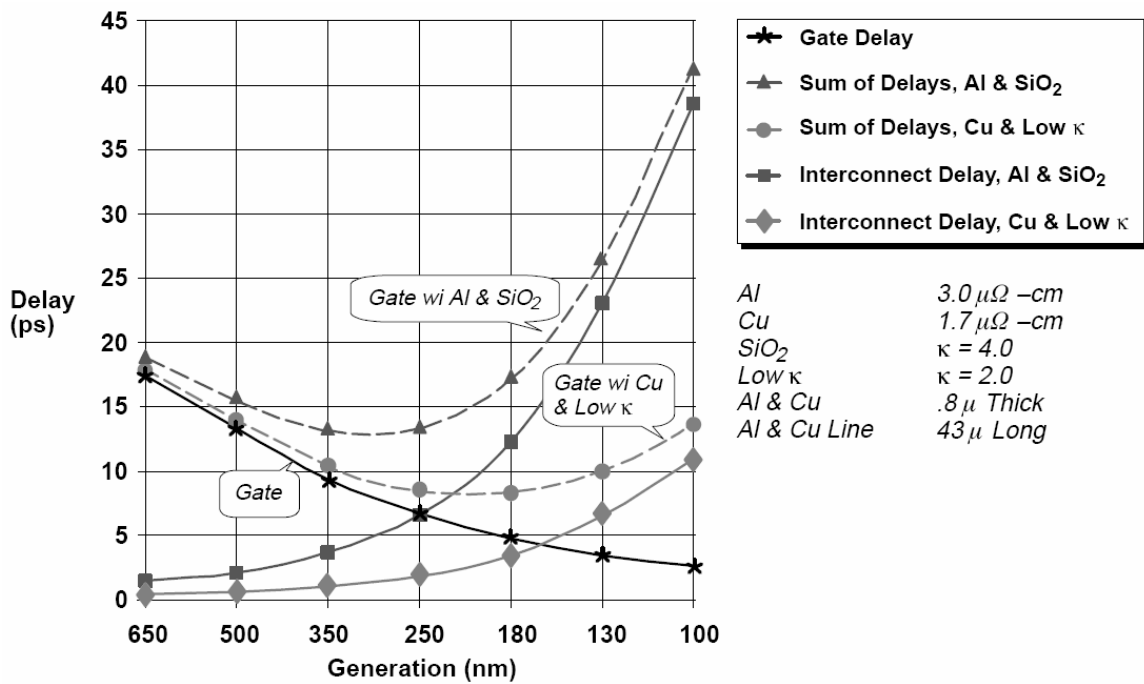


Figure 1.3 Calculated gate and interconnect delay versus technology generation [3].

Figure 1.3 also reveals that switching SiO₂ to low- k is more effective in improving the RC delay. The results are so important that they motivate not only researchers to invest their time in development but also the materials supplier to pay attention to the potential major economic benefits, which are as much as US \$400 million per year in 2006 [4].

1.2 Urgent Development of Intermetal Dielectric Materials with Ultralow Dielectric Constant

The copper dual damascene process has been extensively adopted in the production line, but no consensus exists about the preferred IMD material for sub-65 nm technology nodes. In fact, the implementation of low- k IMD with a required k value was continuously revised from 1999 [5, 6]. The delay in the implementation of low- k IMD is attributable to the fact that many obstacles are difficult to overcome when low- k materials need to be successfully

integrated in a dual damascene interconnect structure. According to the 2005 International Technology Roadmap for Semiconductors (ITRS), IMD materials with a bulk dielectric constant ($k_{bulk} \leq 2.4$) are expected to be used in 2007 [5]. In reaching such a low k value, many porous materials will be candidate ultralow- k dielectrics. Since air has a dielectric constant of about 1.0, introducing air into a dielectric can reduce the k value of the material as a whole. Therefore, the most logical strategy for reducing the k value of a dielectric is to reduce its mass density, or introduce pores into it [7-9]. However, high porosity raises many difficulties to the integration of porous ultralow- k dielectrics into the Cu damascene process. Tables 1.1 and 1.2 present the requirements and the best approximations to the defining characteristics of new IMD materials with $k < 3$, respectively. More effort has to be made to improve the mechanical and thermal properties of porous materials because the porosity is responsible for weak mechanical strength and poor heat conduction. Also, dielectric stability throughout the processing of the device and during its actual use is extremely important. The pore structure of the porous dielectric strongly affects many process steps, including dry etching, wet cleaning and chemical mechanical polishing.

Table 1.1 Requirements for low- k IMD materials.

Electrical	Mechanical	Chemical	Thermal
Isotropic dielectrics	Film uniformity	High selectivity	Thermal stability
Low dielectric loss	Adhesion	Low moisture absorption	Low thermal expansion
Low leakage current	Low stress	Low water solubility	High thermal conductivity
Low charge trap	High tensile modulus	High purity	
High breakdown field	Hardness	Corrosion free to metals	
Reliability	Low contraction	Long shelf time	
	Cracking threshold	ESH compatible	

Table 1.2 Defining IMD characteristics.

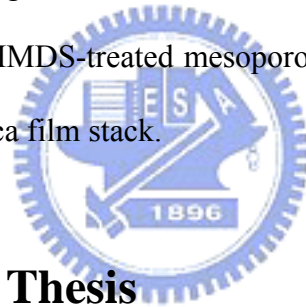
Characteristic	Desired value
Electrical	
Dielectric constant at 1 MHz	1.5-3
Dissipation factor	<0.005
Anisotropy	Undesirable
Breakdown strength	≥ 1 MV/cm
Bulk resistivity	$\geq 10^{15}$ Ω cm
Surface resistivity	$\geq 10^{15}$ Ω cm
Mechanical	
Final stress	$\leq \pm 100$ MPa
Tensile modulus	>1 GPa
Tensile strength	>0.2 GPa
Elongation-at-break	>5%
Crack resistance	Very high
Adhesion	Pass tape peel test after thermal cycling to $\sim 400^\circ\text{C}$
Chemical	
Interaction with acids, bases, and solvents used in processing	Preferably none
CMP	Compatible
Etch	Dry (RIE) high rate, selectivity over metal, oxygen plasma resistance
Moisture absorption	≤ 1 wt%
Out gassing	Low $\leq 500^\circ\text{C}$
Shelf-life	≥ 6 months, at R.T., 40% R.H.
Gap-fill capability	Excellent, no voids
Permeable to	Inert gases and hydrogen
Purity	Very high, free for mobile ions, particles \leq ppb level
Compatible/non-corrosive	With metal and diffusion barrier/adhesion promoter, environmentally safe
Thermal	
Glass transition temperature	$\geq 400^\circ\text{C}$
CTE	<50 ppm, isotropic
Thermal conductivity	High
Thermal stability	
TGA, 1% weight loss	>425 $^\circ\text{C}$
Out gassing temperature	>500 $^\circ\text{C}$
Shrinkage	<2.5%

Among various porous ultralow- k dielectrics, silica-based porous materials are most widely studied because they are chemically compatible with contemporary IC processes and $k < 2.5$ can be easily achieved owing to the high porosity. However, as indicated above, the mechanical strength of porous silica dielectrics is far inferior to that of a dense silicon oxide IMD. Porous silica thin films with nanoscaled pores, including xerogel [10-12] and surfactant templated mesoporous silica [12-16], are typically fabricated by the sol-gel method. In particular, self-assembled molecularly templated mesoporous silica is regarded as a very promising ultralow- k dielectric because it has better mechanical and dielectric characteristics than xerogel because of the ordered pore structure and uniform pore size distribution (2-10 nm) [16-18].

Porous silica dielectrics prepared by the sol-gel approach are typically hydrophilic. Therefore, the uptake of moisture can severely reduce the dielectric stability of the porous materials. Trimethylsilylation method is commonly used to increase the hydrophobicity of porous silica thin film [14-22]. Methylsilylated porous silica thin films not only exhibit improved hydrophobicity, but also better mechanical and dielectric properties. Since they have much poorer mechanical properties than their condensed counterparts, more attention should be paid to mechanical problems associated with the integration of mesoporous silica dielectrics into the Cu interconnect structure. One of the mechanical challenges is to maintain satisfactory adhesion with adjacent layers and resist against delamination or cracking during various processes, including thermal and chemical mechanical polishing (CMP) processes. Mesoporous silica thin films prepared by the sol-gel method exhibit a large tensile stress after drying, because of film shrinkage; plasma-assisted α -SiC:H films typically have compressive stress, whose magnitude depends on the deposition temperature. When these two dielectric materials are combined in a dual damascene structure, concerns about the compatibility of their mechanical properties warrant a close examination of the film stress that develops in the

film stack that is composed of ultralow- k mesoporous silica and barrier/etch stop layers. This thesis studies the film stress of ultralow- k mesoporous silica thin film and the α -SiC:H/mesoporous silica film stack. The effects of trimethylsilylation on the mechanical characteristics and the dielectric character of the mesoporous silica thin film were also studied.

The insertion of trimethylsilyl groups into the pore surface introduces uncertainty in the thermal stability of the mesoporous thin film. A high thermal and chemical stability is certainly critical to the integration of the mesoporous silica dielectric into a copper interconnect. However, the organic trimethylsilyl group can withstand up to a certain temperature in thermal treatment, and may decompose during various high-temperature IC processes, causing severe damage to the interconnect structure. This work studies the thermal and dielectric stability of the HMDS-treated mesoporous silica thin film and its effect on the Cu-metallized mesoporous silica film stack.



1.3 Organization of Thesis

This work discusses the primary issues around porous low- k material integration. Self-assembled molecularly templated mesoporous silica thin films were prepared as low- k dielectrics. Some thin-film characterization approaches are adopted to analyze the electrical, mechanical and thermal properties of the mesoporous silica thin films and metal/dielectric film stacks.

This dissertation is divided into seven chapters. The contents of each chapter are as follows.

Chapter 1 introduces the motivation and organization of this dissertation.

Chapter 2 reviews the literature. The factors that affect the dielectric constant of the materials are initially considered. Then, the general background of low- k materials, especially

mesoporous silica thin films, and their application in backend Cu dual damascene process is presented.

Chapter 3 introduces the experimental method and the analytic technology.

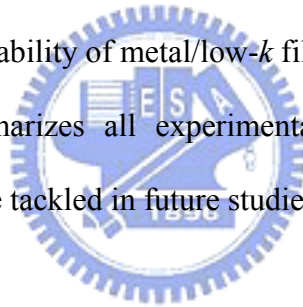
Chapter 4 discusses the dielectric properties and hydrophobicity of self-assembled templated mesoporous silica thin films.

Chapter 5 focuses on the microstructure and mechanical strength of mesoporous silica thin films.

Chapter 6 discusses film stresses in the mesoporous silica dielectric and its stacks. The results of the thermal stress experiment are also discussed. The coefficient of thermal expansion of the mesoporous silica thin film is derived.

Chapter 7 is concerned mainly with the thermal and electrical stability of mesoporous silica thin films. The thermal stability of metal/low- k film stacks was evaluated.

Finally, Chapter 8 summarizes all experimental results. Some unfinished work is mentioned and new issues to be tackled in future studies suggested.



Chapter 2

Literature Review

Many materials, including ceramics and polymers, are electrical insulators and candidates for IMD applications. However, the most promising dielectric is one with material characteristics that can withstand the manufacturing process. This chapter reviews the dielectric properties, material characteristics of low- k dielectrics materials. Both organic and inorganic low- k dielectrics are considered.

2.1 Electrical Performance of Low- k Dielectrics

The basic electrical phenomenon of a dielectric material is polarization: an electric dipole moment can be induced by an electric field or can be permanent. A dielectric material can exhibit three forms of polarization in an applied electric field - electronic, ionic and orientation [23, 24]. Electronic polarization arises when the cloud of bound electrons is displaced from the nucleus of an atom, resulting in an electric dipole moment. Ionic polarization refers to the distortion of the position of the nuclei by the applied field, and, therefore, a change in the bond length. Some also refer to this as atomic polarization. If a molecule has a permanent electric dipole moment, which arises from the different electronegativity or other features of bonding, then polar molecules can exhibit orientation polarization in an applied field. These three polarization phenomena reveal at the specific frequency of an ac field and determine the polarizability of materials. For instance, orientation polarization involves the motion of complete molecules, so it does not resonate at a critical frequency, as do electronic and ionic polarization. Electronic polarization dominates at high

frequency ($\sim 10^{15}$ Hz), while the other two polarization are nuclear responses and are important at lower frequencies ($< 10^{13}$ Hz). Currently, typical device operating frequencies are 10^9 to 10^{10} Hz, and all three polarization contribute to the dielectric constant, as discussed below. (The maximum response frequency of orientation polarization is of the order of 10^9 Hz). Therefore, the polarization of IMD materials should be minimized to optimize performance.

The relationship between the dielectric constant and the total polarization can be quantitatively described by the Clausius-Mossotti equation [24],

$$\frac{\epsilon_r - 1}{\epsilon_r + 2} = \frac{N}{3\epsilon_0} (\alpha_e + \alpha_i + \alpha_o), \quad (2.1)$$

where ϵ_r the relative permittivity or dielectric constant of material, ϵ_0 the permittivity of a vacuum and N the number of molecules per m^3 . The terms α_e , α_i and α_o are the electronic, ionic and orientation polarizations in the molecule, respectively. According to the equation, the relative permittivity is smaller if materials contain fewer polar molecules. This fact offers an important clue to the fact that reducing the density N and the polarizabilities α can reduce the dielectric constant. Table 2.1 presents the polarizabilities of some typical chemical bonds [25]. C-F and C-C bonds have the lowest polarizability, indicating that the incorporation of fluorine atoms and reducing the number of double or triple bonds can effectively reduce the polarization of materials. The former is associated with high electronegativity, which causes tight binding of the electrons and increases free volume. The latter is associated with a drop in the mobility of the π electrons. Some fluorinated aliphatic hydrocarbon materials are designed using these rules for low- k applications. For example, polyimides, which are extensively adopted in microelectronics, have dielectric constant values in the range 2.9-3.4. Fluorine substitution can reduce the dielectric constant to a lower value of 2.6 [26].

Table 2.1 Electronic polarizability of some typical chemical bonds [25].

Bond	Polarizability (\AA^3)
C-C	0.531
C-F	0.555
C-O	0.584
C-H	0.652
O-H	0.706
C=O	1.020
C=C	1.643
C≡C	2.036
C≡N	2.239

Although the contribution of polarization to the dielectric constant of materials is very important, the ways to reduce molecular polarizability are limited. Equation (2.1) also reveals that film density, like the chemical bonds, is important in reducing relative permittivity. Reducing the density is considered to be more effective because it can reduce k to close to unity. It can be performed using lighter atoms and/or by incorporating more free space around the atoms. Technologically, the best way to reduce film density is to introduce pores. Treating the porous film as two component materials, enables Eq. (2.1) to be rewritten as [27],

$$\frac{\varepsilon_r - 1}{\varepsilon_r + 2} = \Pi \cdot \frac{(\varepsilon_p - 1)}{(\varepsilon_p + 2)} + (1 - \Pi) \cdot \frac{(\varepsilon_m - 1)}{(\varepsilon_m + 2)}, \quad (2.2)$$

$$\Pi = \frac{V_p}{V_f}, \quad (2.3)$$

where ε_p and ε_m are the permittivity of the internal pores and the solid matrix of the film, respectively. The porosity of the film, Π , defined by Eq. (2.3), is the ratio that of the volume of the pores (V_p) to the total volume of the film (V_f). Equation (2.2) is also called the Bruggeman effective medium approximation and predicts the effect of porosity on the

dielectric constant. Figure 2.1 presents the theoretical predication of the model for SiO_2 ($k=4$) and a material with an original k value of 2.5. The curves reveal that the dielectric constant decreases as a function of porosity slightly faster than linearly. This fact is very useful to the material designer who wishes to estimate the minimum porosity required for a desired k value. For instance, to yield $k=2.0$, oxide materials require a porosity of about 50%. However, as presented in Fig. 2.1, a porosity of only $\sim 30\%$ is required for a $k=2.5$ low- k material, indicating that the lower k start value corresponds to a lower required porosity, potentially increasing the integration compatibility of the low- k materials. Additionally, the k values in Fig. 2.1 are ideal (for a dry film) and quite different from typical experimental values. In a real case, the reserve environment and the test methods affect the results. Most oxides contain many terminal OH groups and thus adsorb water. This trapped water ($k \approx 78$) or chemicals are likely to increase the dielectric constant and promote crack formation; a k value of below 2.0 is difficult to obtain even though the porosity is increased.

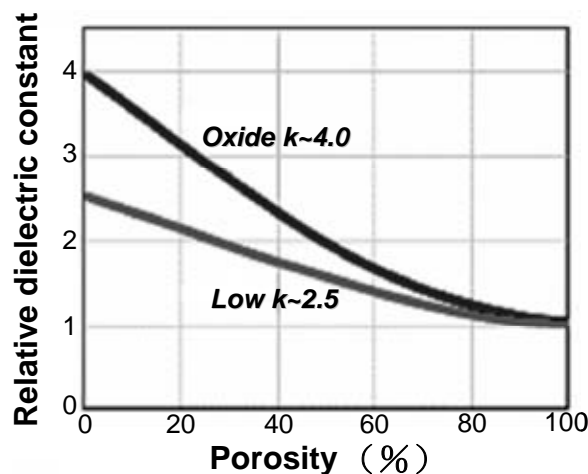
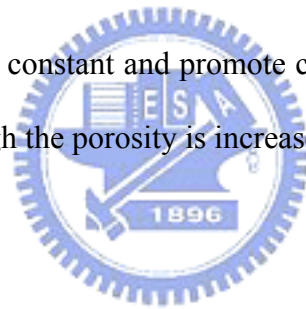


Figure 2.1 Bruggeman's effective medium approximation showing dielectric constant versus porosity for oxide and a low- k material.

2.2 Potential Solutions for Creating Low- k Dielectrics

Many low- k materials, including organic and inorganic dielectrics, have been proposed as replacements for the traditional CVD SiO₂. The dielectric constant of CVD SiO₂ films is 4.0±0.2, and dielectrics with a k value of below 4.0 are defined as low- k dielectric materials. SEMATECH has basically characterized several classes of candidate low- k materials. Table 2.2 presents the results. These candidate low- k materials are generally categorized as follows.

1. Oxides or organic polymers
2. Organic, inorganic or hybrid materials
3. CVD or spin-on methods
4. Fluorinated or nonfluorinated materials
5. Porous or nonporous materials

This section introduces the potential low- k materials. The material characterization and integration issues of them are presented for comparison.



2.2.1 Fluorosilicate Glass (FSG)

Fluorine atoms were initially incorporated into SiO₂ to reduce the k value relative to that of the traditional silicate glass, SiO₂, in the development of low- k materials and fluorosilicate glass, FSG. The fabrication of FSG involves chemical vapor deposition, which process extends traditional SiO₂ manufacture. Therefore, this material has attracted the attention of chipmakers. Figure 2.2 presents the chemical structure of FSG. Since fluorine is very electronegative, the incorporation of fluorine atoms reduces the polarization of SiO₂, decreasing the dielectric constant, as described in section 2.1. Additionally, more terminal Si-F bonds result in a looser SiO₂ structure and a drop in the density of the film. Therefore, the dielectric constant of SiO₂ can be reduced; the drop depends on the concentration of

Table 2.2 Classification of low-*k* candidates.

<i>k</i> value	CVD inorganic	CVD organic	Spin-on inorganic	Spin-on organic
$k \sim 4.0$	SiO ₂ (3.9-4.2)			
$3.1 \leq k \leq 4.0$	SiO _x F _y (3.4-4.1)			
$2.4 \leq k < 3.1$	Coral™ (2.4-3.0) Black Diamond™ (2.2-2.7)		HSQ/MSQ (2.5-3.3)	Polyimides (3.1) Silicon-based polymer (2.8-3.0) Polyarylene ethers (2.6-2.8) BCB (2.6) SiLK™ (2.6)
$2.0 \leq k < 2.4$		Parylene AF4 (2.25) Amorphous fluorocarbon (2.1-2.5)		Porous SiLK™ (<2.6)
$k < 2.0$		PTFE (1.9)	Nanoglass™ (1.8-2.5) Xerogel (1.2-3.9) Mesoporous silica (1.3-2.5)	Porous organosilicate (<2.2) Porous PTFE (<1.9)

fluorine. Experimentally, adding 10-15 at% F to SiO₂ can reduce the *k* value by 20% to about 3.3.

Although fluorosilicate glass can be fabricated by many thin film deposition approaches, including TEOS-CVD, ECR-CVD, AP-CVD and LP-CVD, the most general approach is high-density plasma CVD (HDP-CVD). SiH₄ and fluorides (such as SiF₄, C₂F₆, CF₄ or TEFS) as the gas source support simultaneous deposition and etch back, resulting in good gapfilling capacity without any void even for a width of 0.25 μm [28]. FSG has now been introduced into 0.25 and 0.18 μm IC production lines because of its chemical compatibility with IC processes. However, the thermal stability of fluorine is lower, potentially making the

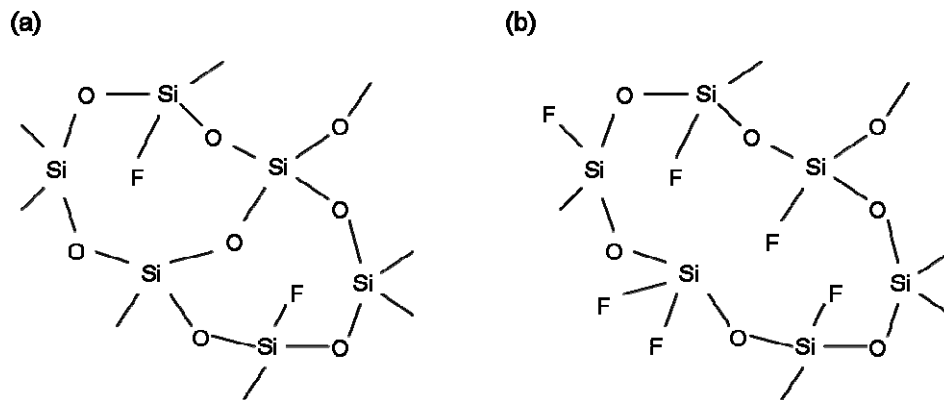


Figure 2.2 Chemical structures of FSG with (a) low fluorine concentration, (b) high fluorine concentration.

dielectric unstable. The thermal treatment temperature should be under 450°C, when FSG films are used for IMD. Additionally, although the incorporation of fluorine makes the geometry of the Si-O network less polarizable, the concentration should be less than 10 at% to ensure the stability of the film, because the drop in film density provides more free space for the adsorption of moisture. This limitation in the fluorine concentration or in dielectric constant, causes the FSG films to fail at the 0.13 μm IC technology node and below.

2.2.2 Silsesquioxane (SSQ)-based Materials

Silsesquioxane-based materials comprise the inorganic Si-O bonding unit and organic substituents of low molecular weight, or hydrogen. Empirically, they have the chemical formula $(\text{R-SiO}_{1.5})_n$ where the substituent R may be hydrogen, alkyl, alkenyl, alkoxy or aryl. Their name is derived from the sesqui-stoichiometry of oxygen atoms bound to a silicon atom, and they are therefore also called “T-resin” (tri-substituted). The most common structures are oligomers with a cage (T_8 cube, eight silicon atoms on the vertices of the cube) or a ladder structure [29], as presented in Fig. 2.3.

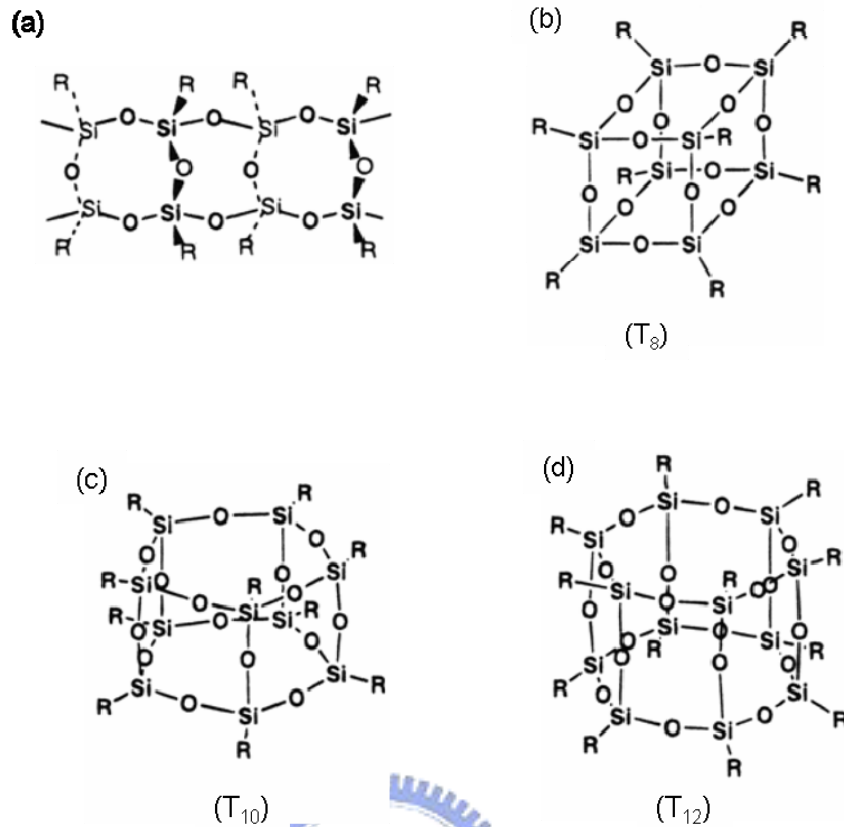


Figure 2.3 Ladder (a) and cage (b-d) structures of Silsesquioxanes [29].

Organic substitution on Si causes the SSQ oligomer commonly to dissolve in an organic solvent as a precursor, before it is spin-coated on a substrate. These precursor solutions, developed by many famous suppliers of chemical materials, can yield SSQ low- k films with $k < 3.0$, as indicated in Table 2.3. Following spin-on, the film has the characteristics of a liquid gel. It necessarily suffers baking and curing steps, which promote the formation of a

Table 2.3 Available SSQ-based low- k materials.

Material	Trade name	k value	Company
HSQ	Fox (flowable oxide)	2.9-3.0	Dow Corning
MSQ	RZ25-15	2.6	Hitachi
MSQ	HOSP	2.6	Honeywell
Porous HSQ	XLK	2.2	Dow Corning
Porous MSQ	LKD 5109	2.2-2.3	JSR
Porous MSQ	Zirkon	2.3	Shipley

three-dimensional network siloxane (Si-O-Si) skeleton. During baking, the residual solvent is removed. Further curing results in polycondensation, which forms the mutually bonded silsesquioxane units [30]. Liu *et al.* [31], and Liou and Pretzer [32, 33] backed at 180-250°C for MSQ and 150-350°C for HSQ, following curing above 400°C; the as-cured films had dielectric constants of 2.9-3.2. Although the siloxane matrix is chemically similar to SiO₂, more than 25% non-bridging Si-R bonds yield a lower density than that of SiO₂. The Si-R bond has a relative lower polarizability than the Si-O bond in SiO₂. The lower density and polarizability bonds of SSQ are attributed to the lower *k* values in the range 2.5-3.3.

The three common silsesquioxane compounds are recognized by the substituents R:

Hydrogen-silsesquioxane (HSQ, HSSQ),

Methyl-silsesquioxane (MSQ, MSSQ),

Phenyl-silsesquioxane (PSQ, PSSQ).

The material properties of these three silicate based materials vary greatly as indicated in Table 2.4. HSQ (H-SiO_{1.5}) and MSQ (CH₃-SiO_{1.5}) are two low-*k* SSQ materials used commonly in microelectronic applications. HSQ has a *k* value in the range 3.0-3.2 but it involves many problems of integration. For instance, Liou and Pretzer [33] found that a network structure formed upon thermal processing at over 400°C due to the disassociation of Si-H bonds, which increases the difficulty of integration. MSQ has a dielectric constant of

Table 2.4 Material properties for SSQ-based matrix resins.

Property	SiO ₂	HSSQ	MSSQ	PSSQ
Dielectric constant	4.0	3.0	2.8	--
Modulus	70-80 GPa	6 GPa	3-5 GPa	--
Density	2.2 g/cm ³	1.4-1.5 g/cm ³	1.2-1.3 g/cm ³	--
Contact angle	<20°	–	108°	94°
Refractive index (at 632.8 nm)	1.458	–	1.37	1.554
Tensile Strength	--	80 MPa	50 MPa	28 MPa

2.8, lower than that of HSQ, because the the Si-CH₃ bonds are larger but less polarizable than the Si-H bonds. It is also more stable during the thermal process. The challenge raised by HSQ is degradation during O₂ plasma resist stripping, such that an alternative stripping technique, such as H₂ plasma treatment, is required [31].

Additional pores are introduced into the matrix resins of both HSQ and MSQ by adding surfactant or porogen, to greatly reduce the dielectric constants. Table 2.3 presents some of the results, and the section on porous materials will present details of the pore-forming methods.

2.2.3 Low-*k* Polymers

Since the 1980s, a large group of researchers have studied many newly synthesized or pre-existing polymers for their use as IMDs. For example, polyimide, a traditional material used in IC packaging, has a low *k* value from 2.3 to 2.9. Such polymers are varied but most are inappropriate for use in actual Cu metallization. Seven main considerations limit their applicability:

1. poor thermal stability (weight loss >1.0% at under 450°C)
2. anisotropic thermal, electrical and mechanical properties
3. softness
4. poor thermal conductivity
5. moisture uptake and outgassing
6. poor adherence to other contact layers, including the metal line and the diffusion barrier
7. incompatibility with traditional technological processes developed for SiO₂-based dielectrics.

Figure 2.4 presents the chemical structures of some common polymer low-*k* materials.

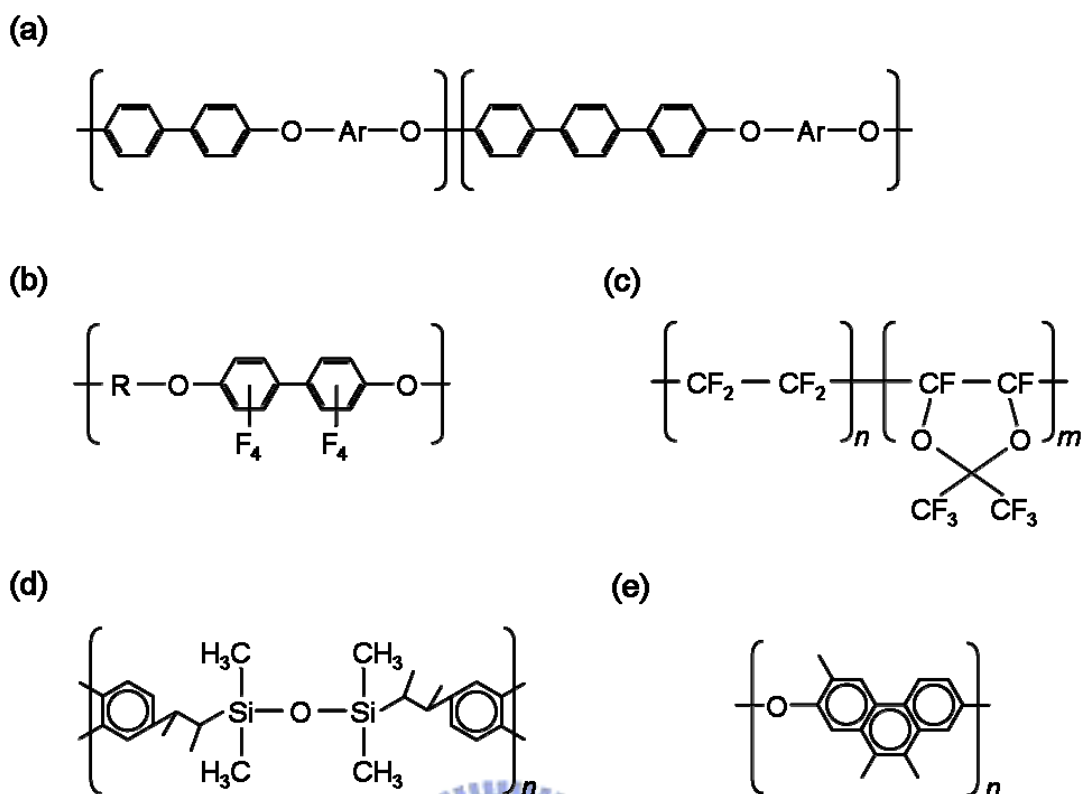


Figure 2.4 Chemical structures of (a) polyarylethers; (b) FLARE™; (c) Teflon AF; (d) divinylsiloxane-benzocyclobutene (DVS-BCB); (e) SiLK.

Notably, these materials often have symmetric monomer structures, balancing the polarizability of the polymers. Additionally, organic low- k polymers are typically synthesized as non-polar or polar polymers. Non-polar polymers comprise primarily non-polar C-C bonds. Therefore, they have dielectric constants that are independent of frequency, such that their dielectric losses are low. Unlike non-polar polymers, polar polymers have an asymmetric charge distribution, which arises from differences among the electronegativities of atoms. They therefore have higher dielectric loss and a dielectric constant that depends on frequency and temperature. Saturated hydrocarbons have a lower polarizability and dielectric constant than unsaturated, conjugated and aromatic hydrocarbons (Table 2.1). However, they typically suffer from thermal degradation at temperatures of 300-400°C, or even much lower temperature. Only materials with aromatic, ladder, cross-linked structures can tolerate

temperatures of 450-500°C, which are required for IC interconnects. This situation represents a dilemma but the designer must find a compromise between the dielectric constant and the thermal stability when producing reliable polymer dielectric films. Empirically, most low-*k* polymer films with sufficient thermal stability have dielectric constants of 2.6-2.8.

In the last five years, low-*k* polymers have remained attractive to some researchers because of their properties are variable [34, 35]. These variations in the properties of polymers involve the partial rearrangement of monomers [36, 37]. Two polymers, PVDF [poly(vinylidene fluoride)] and PTFE [poly(tetrafluoroethene) or Teflon], have very similar chemical structures, but widely different properties. As presented in Fig. 2.5, the difference between these polymers that the two hydrogen atoms in PVDF are replaced by two fluorine atoms in PTFE. This slight difference between bonding atoms makes PVDF soluble in a polar solvent and PTFE is insoluble in organic solvents. Additionally, replacing the hydrogen with larger side groups can generate asymmetry in the polymer chain, reducing the tendency of the chains to slide past each other and increasing the tendency to form bonds between the chains, improving rigidity and increasing the melting point. Another case of interest involves copolymer, which replaces the side of the polymer chain with two or more polymer branches. Such branched structures may reduce the packing density of linear polymer, affecting the mechanical properties and the thermally induced glass transition temperature, T_g . (More branching corresponds to lower crystallinity).

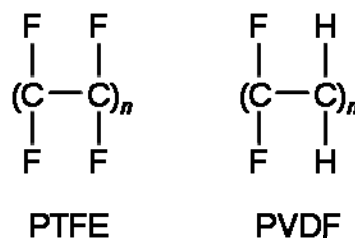


Figure 2.5 Chemical structure of PTFE and PVDF.

The glass transition temperature is some temperature, or narrow range of temperatures below which an amorphous polymer is in a glassy state, and above which it is rubbery. Polymer is glass or rubbery, depending on whether its application temperature is above or below its T_g ($>450-500^\circ\text{C}$ for low- k films). The degree of cross-linking, which affects the thermal [38] and mechanical [39] properties of low- k polymer materials, also affects their glass transition temperature. Polymer chains may chemically link to each other via the reactive groups, to form a 3D network, in a process called cross-linking, which typically occurs during curing, improving stiffness, and ensuring that the behavior prior to plastic deformation under a load is sustainable. Heavily cross-linked polymers, or thermosetting polymers, typically have a high T_g and better mechanical yield strength. They are generally brittle [40]. Epoxies, polyurethane, parylenes, polyimide siloxanes, polyimides and FPI (fluorinated polyimides), benzocyclobutene (BCB) [41], SiLKTM [42, 43], FLARETM [fluorinated poly(arylethers)] [44], PAE [poly(arylethers)], HOSPTM (hybrid organosiloxane) [44] and perfluorocyclobutane are such polymers and are preferred for use in IMD applications.

Figure 2.4 presents the chemical structures of PAE, FLARETM, BCB and SiLKTM low- k materials. These organic polymers with a dielectric constant in the range 2.5-3.0 contain large amounts of benzene or fluorine, and, therefore, have low dielectric constants and good thermal stability. They share the problems of poor mechanical strength and poor adhesion. Therefore, a capping oxide layer and an adhesion promoter must be added to each for integration. Table 2.5 also presents some of the polymers adopted in IMD applications.

Another focus of low- k polymer candidates is SiLKTM resin. SiLKTM is a spin-on hydrocarbon dielectric [5, 6, 42, 43, 45], which was developed by the Dow Chemical company. In 2000, IBM Microelectronics first used this dielectric material was first used in 0.13 μm BEOL. Figure 2.6 presents a four-level metal SRAM structure with a three-level

Table 2.5 Some of the polymers for low- k application.

Polymer	k value	T_g (°C)	Moisture absorption (wt%)
HOSP	~2.5	--	1-2
Polyarylethers	2.6-2.8	260-450	<0.4
FLARE	2.4-2.6	280-300	<0.2
Teflon AF	1.9	≤ 360	--
DVS-BCB	2.6-2.7	≥ 350	<0.2
Polynorborene	2.2	365	<0.1
SiLK	2.6-2.7	>450	<0.25
Parylene-n	2.6-2.8	420	<0.05
Parylene-c	2.7-3.0	--	--
Parylene-d	2.7-3.0	--	--
Parylene-f	2.2-2.4	>530	--
FPI-45M	2.8	~500	0.95
FPI-136M	2.64	~500	1.5
F-TAE	2.2-2.8	≥ 300	--
Polyimide	2.7-3.1	350	1.5-3.0

SiLKTM dielectric [5]. Water is typically generated during curing because of dehydration in the condensation reaction in the synthesis of polymer from monomers. The SiLKTM resin is an extremely dense aromatic hydrocarbon (Fig. 2.4e) and releases no moisture as a byproduct during curing. Table 2.6 summarizes the main properties of SiLKTM dielectric. As indicated in the table, SiLKTM has a k value of 2.6 and $T_g > 490^\circ\text{C}$, resulting in thermal stability over 425°C . Its intrinsic properties are so intriguing that UMC actively developed it as IMD [46]. However, UMC announced that it was ending its development of SiLKTM and in Feb. 2002, when it began to use FSG and CoralTM (carbon-doped oxide). After two years, IBM also considered abandoning SiLKTM because its CTE (which is a function of temperature) is too high at temperatures of over 150°C [47]. Although other refinements were subsequently announced, they did not satisfy the chipmakers. Nowadays, some Japanese companies like SONY and Fujitsu use a hybrid scheme as an IMD structure.

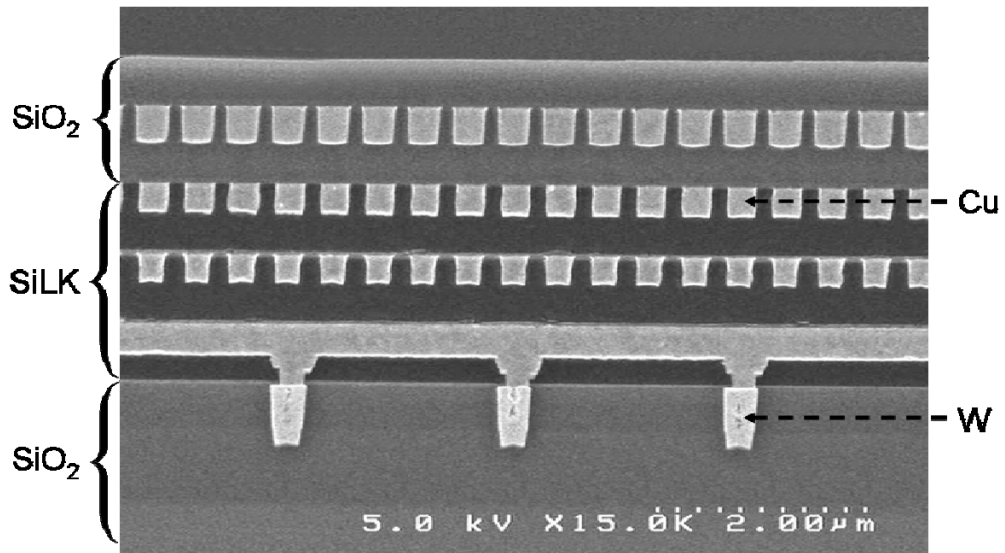


Figure 2.6 SEM cross-sectional image of Cu-SiLK™ interconnect structure [5].

Table 2.6 Intrinsic properties of SiLK™ low-*k* dielectric.

Property	Value
Dielectric constant	2.65
Breakdown voltage	4 MV/cm
Leakage current (at 1 MV/cm)	0.33 nA/cm ²
Refractive index (at 632.8 nm)	1.63
Moisture uptake (at 20°C, 80% R.H.)	0.24%
Thermal stability	>425°C
Weight loss (at 450°C)	0.7 wt%/h
Thermal conductivity	0.19 W/mK (at 25°C) 0.23 W/mK (at 125°C)
Glass transition temperature	>490°C
Young's modulus	2.45 GPa
Hardness	0.38 GPa
Toughness	0.62 MPa m ^{1/2}
Strength	90 MPa
Ultimate strain	11.5%
Residual stress (at R.T.)	56 MPa
CTE	66 ppm/°C

2.2.4 Amorphous Carbon

The use of fluorinated amorphous carbon (a-C:F) thin films as IMDs with low dielectric constants was recently reported [39, 48-59]. Sometimes, such materials are given such names as diamond-like carbon (DLC), hydrogenated DLC, fluorine-containing DLC (FDLC) [51, 52], plasma-polymerized fluorocarbon (PPFC) [53], fluorinated amorphous-carbon (a-C:F:H) [39] and amorphous carbon fluoride (a-CF) [54]. All these films have a wide range of k values from 2.0 to 3.6 and are typically formed by plasma-enhanced CVD (PECVD) using a discharge with fluoro-carbon gases (such as CF_4 , C_2F_6 , $\text{C}_4\text{F}_8 + \text{CH}_4$ or hydrogen mixtures). The film comprises amorphous C-C cross-linked bonds (mixing of sp^3 and sp^2 bonding) and C-F bonds with a PTFE-like structure. Controlling the F/C ratio of an a-C:F film is important because it is the factor that most strongly affects the dielectric constant and the thermal stability. C-F bonds with a weak tendency to polarize in external electrical fields can reduce the dielectric constant of the a-C:F thin film, but excess C-F bonds suppress the formation of C-C cross-links, which would otherwise maintain the film's thermal stability. Therefore, the properties of the a-C:F thin films can be adjusted easily by changing the plasma process conditions.

2.2.5 Carbon-doped Silica

Alkyl groups, like fluorine, can be incorporated into silicon dioxide to reduce its k value. It is called carbon-doped oxide (CDO) [also known as organosilicate glass (OSG), or silicon oxycarbide (SiOCH)]. Carbon-doped oxide films can be deposited at $\geq 400^\circ\text{C}$ by PECVD, typically using O_2 and such precursors as methylsilane (1MS, H_3SiCH_3), dimethylsilane [2MS, $\text{H}_2\text{Si}(\text{CH}_3)_2$], trimethylsilane [3MS, $\text{HSi}(\text{CH}_3)_3$], tetramethylsilane [4MS, $\text{Si}(\text{CH}_3)_4$] [60-62], and other methyl-based sources, including tetramethylcyclotetrasiloxane (TMCTS) [63, 64], octamethylcyclotetrasiloxane (OMCTS) [65] and dimethyldimethoxysilane (DMDMOS) [66].

Of these, 3MS is the most widely accepted precursor for depositing CDO films because it is safe and the industry is familiar with it. CDO film has a dielectric constant of between 2.2 and 3.0, determined by the amount of methyl dopants. These dopants terminate some Si-O bond links in the oxide matrix, and reduce the electronic polarizability of the film. However, adding more carbon may create more problems such as cracking, softness and lack of adhesion. Precursors with more methyl groups can generally incorporate more carbon into the film, replacing 10-25% of the Si atoms [66-67].

The incorporated methyl groups also influence the physical, chemical and thermal properties of the CDO films. Table 2.7 presents some characteristics of the CDO films. CDO films have good thermal conductivity (~ 0.9 W/mC for PE-SiO₂) and a coefficient of thermal expansion (CTE) that is close to those of Cu (~ 17.7 ppm/ $^{\circ}$ C) and TaN (~ 6 ppm/ $^{\circ}$ C). Therefore, the CDO thin films resist cracking and peeling when integrated into a Cu interconnect. Well-known commercial CDO materials are CoralTM from Novellus Systems Inc. [68] and Black DiamondTM from Applied Materials Inc. [69]. The k value of Black DiamondTM II is less than 2.7 and is acceptable for 90 nm chips. Recently, TSMC decided to use a low- k Black Diamond system as its 90 nm process IMD [70, 71]. CDO dielectrics now seem to dominate the market of 90 nm IC products.

Table 2.7 Film properties of carbon-doped oxide and PECVD oxide.

Property	Carbon-doped oxide	PECVD SiO ₂
Dielectric constant	<3.0	4.2
Refractive index	<1.42	1.46
Stress	Tensile	Compressive
Young's modulus	<10 GPa	70-80 GPa
Hardness	<2.0 GPa	7-9 GPa
Density	<1.4 g/cm ³	2.2 g/cm ³
Thermal conductivity	<0.4 W/mC	~ 1 W/mC
CTE	<10 ppm/ $^{\circ}$ C	<1 ppm/ $^{\circ}$ C

2.2.6 Porous Materials

Introducing porosity into the materials is the only way to achieve dielectric constants of far below 2.3. Therefore, much research has been performed in this area. Most porous materials have a porosity of between 0.2 and 0.95. Pores can be straight or curved with various shapes and morphology, including cylindrical, spherical and slit. Pore size, according to the International Union of Pure and Applied Chemistry (IUPAC), is defined as follows; micropores have diameters of under 2nm, mesopores of 2 to 50 nm and macropores of over 50 nm. This definition somewhat contradicts that used in other nanoscale fields. Nanoporous materials actually include some microporous materials and all mesoporous materials.

Porous materials are of two main types. The first type has open pores, which connect to the surface of the materials, and the second has closed pores, which are isolated from the outside. Typical open pore-structured materials include silica xerogel [10-12, 21, 72, 82], aregel [73, 83] and templated silica films [13-16, 74-76, 84-106]. These materials are prepared by the sol-gel process, and they are made porous by removing the solvent and the templated molecules. The hydrolysis-polymerization of alkoxy silanes requires that the internal pore surface of porous silica be full of silanol groups and chemically modified to make the material hydrophobic. Additionally, templated and zeolite [77] porous low- k materials have more ordered pore arrays, resulting in a higher modulus and hardness than other porous materials. Closed pore films are synthesized by burning or dissolving organic components, forming foams in the silica matrix. These films have limited porosity. Once the porosity exceeds ~20-25%, the pores connect to each other, and become an open pore structure. However, $k \leq 2.0$ only with over 50% porosity in an ideal oxide ($k=4.0$), as predicted by the Bruggeman approximation [78]. Therefore, the closed pore structure is more suitable for a low- k material whose original k value is lower.

2.2.6.1 Porous Silsesquioxanes

Common porous materials are silica-based materials such as porous silsesquioxanes (porous SSQ) and xerogel silica. Porous SSQ are prepared by adding porogens into the SSQ resins to reduce k . Porogens are commonly organic components that are easy to remove. Aoi [8] used triphenylsilanol (TPS) moieties as porogens to synthesize porous films with pores with a diameter of 80 nm and $k \sim 2.3$. Other commercial examples with $k \sim 2.2$ include LKDTM porous MSQ by JSR [79] and XLKTM porous HSQ by Dow Corning [80].

2.2.6.2 Xerogel and Aerogel

Xerogel silica films are synthesized by the sol-gel process [81]. A sol solution is typically in the form of uniformly dispersed colloids that comprise silicon alkoxide, water and alcohol solvent. Alkoxides are popular precursors because they react readily with water. Catalyzed by an acid or base, the hydrolysis and condensation reactions in the sol-gel process cause the aggregation of colloids to form silica gel. After the solvent has been removed, a silica film with a random pore structure is obtained. The porosity and the microstructure of the xerogel film vary with the sol-gel conditions, including concentration, temperature, pH value and aging time [81]. Under some critical conditions, the porosity of the xerogel film can be as large as $\sim 80\%$, yielding $k < 1.5$. Buckley and Greenblatt [82] used TEOS, ethanol and water to prepare xerogel and found that the particle size decreased as the ethanol ratio of the solution increased. They also showed that mesoporosity was preferentially formed at low water content, while macroporosity preferentially formed at high water content. The preparation of aerogel is similar to that of xerogel but the drying differs considerably (Fig. 2.7). Aerogel is dried using supercritical fluids, including humidified carbon dioxide. The alcohol solvent is extracted rapidly from the aerogel film into the CO₂ phase, promoting rapid and extensive network condensation. The shrinkage of the film, therefore, is less and ultrahigh

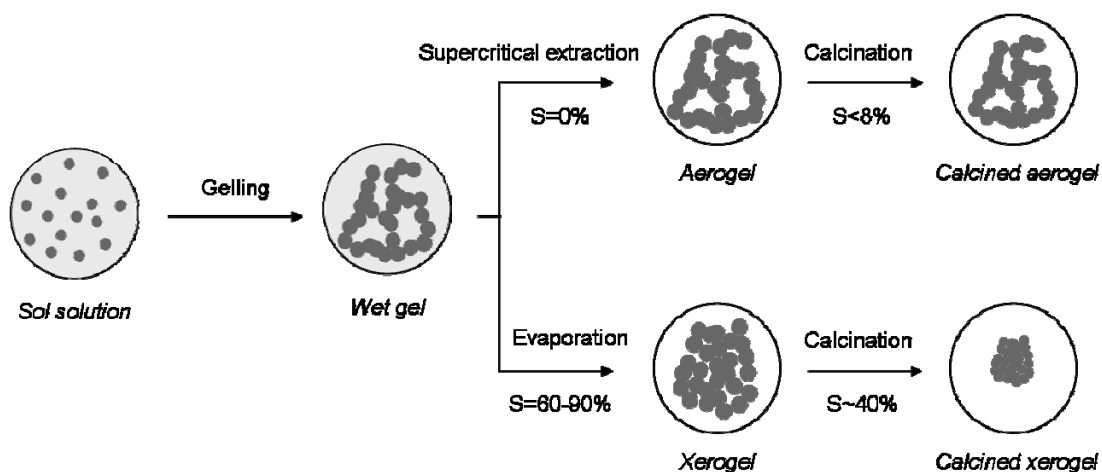


Figure 2.7 Synthesis process of aerogel and xerogel (S: shrinkage).

porosity ($\sim 90\%$, $k \approx 1.3$) can be achieved. However, the high temperature and high pressure used in the process make it dangerous and require a large amount to be spent on the instruments [83]. In contrast, the solvent in xerogel is dried thermally in air, which is much less dangerous and lower cost. Therefore, xerogel films are more suitable for practical use.



2.2.6.3 Surfactant-Templated Mesoporous Materials

Self-assembly surfactant template methods have been used to prepare mesoporous low- k dielectrics that are stable, and have ordered pore geometry and high porosity. The surfactant template approach to porous materials uses the propensity of surfactants to yield ordered supramolecular assemblies in solution. In 1992, Mobil researchers for the first time synthesized a family of ordered mesoporous aluminosilicates (MCM-41 groups) [84, 85]. Since then, the surfactant template approach has extended porous materials from traditional microporous zeolite to meso-scale materials with larger, uniform and ordered pore structures. Such materials typically have the following properties;

- high surface areas ($>1000 \text{ m}^2/\text{g}$),
- adjustable uniform pore sizes (2-10 nm),

liquid crystal-like structure, with long range ordering of pores,
 structural stability,
 ease of surface functionalization, and
 compositional tailoring of the inorganic framework.

Therefore, they are extensively investigated for various applications, including catalysis [86], adsorption [87], separation [88], optics [89], sensors [90] and electronics [91].

The microstructures of surfactant-templated materials can be disordered or ordered with a lamellar, cubic or hexagonal phase. Figure 2.8 presents examples of ordered and disordered phases of mesostructured materials reported in the literature [92-98]. The formation of these mesostructures involves surfactant (S)/inorganic (I) chemical interactions. Based on the nature of the surfactant molecules and synthetic conditions, various S/I interactions have been proposed. They are listed in Table 2.8 and include electrostatic (S^+T^- , ST^+ , $S^+X^-T^+$, $S^-M^+T^-$) [84, 85, 99, 100], hydrogen-bonding ($S^{0+}T^{0-}$, $N^{0+}T^{0-}$) [101, 102], hydrogen-bonding/electrostatic [$(S^0H^+)(X^-T^+)$] [103, 104] and covalent (S-I) [105]. MCM-41 and M41S materials are

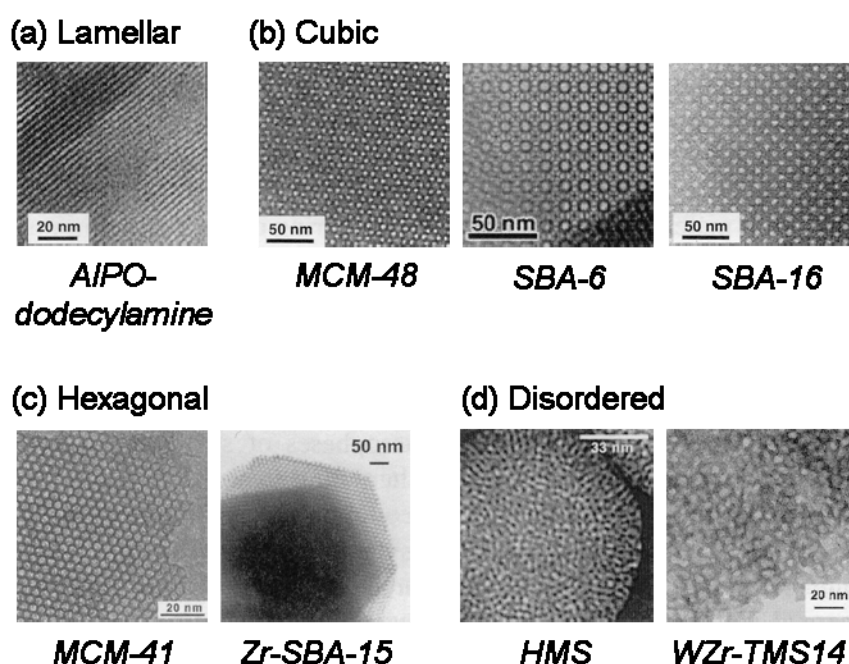


Figure 2.8 Ordered and disordered phases of mesostructured materials [92-98].

Table 2.8 Various surfactant/inorganic (S/I) mesostructures and the reaction conditions.

Interaction	Example
S^+I^-	MCM-41 mesoporous SiO_2 (at basic pH)
S^-I^+	Al-dodecylphosphate mesostructure (at acidic pH)
$S^+X^-I^+$	SBA-3 mesoporous SiO_2 (at acidic pH)
SM^+I^-	Al-dodecylphosphate mesostructure (at basic pH)
S^0I^0	HMS mesoporous SiO_2 (at neutral pH)
N^0I^0	MSU-1 mesoporous SiO_2 (at neutral pH)
$(S^0H^+)(X^-I^+)$	SBA-15 mesoporous SiO_2 (at acidic pH)
S-I	Nb-TMS1 mesoporous Nb_2O_5

synthesized by S^+I^- interactions [84, 85]. Under basic conditions, the attraction between the cationic ammonium (CTAB) surfactant (S^+) and the hydrated silica with an anionic charge (I^-) leads to the formation of a hexagonal micelle rod array. Pannavania *et al.* [101] used neutral amine surfactant (S^0) and neutral inorganic precursors (I^0) to prepare mesoporous metal oxide via S^0I^0 interaction. However, these ionic or neutral amine surfactants are typically toxic and expensive, and inappropriate for use in IC industries. The nonionic amphiphilic PEO (polyethylene oxide) surfactants, including diblock and triblock copolymers, are relatively low-cost, nontoxic and biodegradable [106], and are better suited to use in the IC industry. Amphiphilic block copolymers have hydrophilic and hydrophobic blocks, and the number of repeating blocks can be controlled. Therefore, a wide range of PEO block copolymers with various compositions and properties can be formed. For instance, two pluronic triblock $EO_mPO_{70}EO_m$ amphiphilic copolymers, P123 (SBA-15, $m=20$) [103] and F127 (SBA-16, $m=106$) [104], with the same block composition but different EO/PO ratios, have very different pore structures. SBA-15 (EO/PO=0.07~1.5) has a pore size of 4.7-8.9 nm and a hexagonal (space group $p6mm$) mesostructure. Its pore size and wall thickness can be controlled by hydrothermal treatment because increasing the temperature increases the

hydrophobicity of the PE segments and increases the number of micell that aggregate in the silica framework. SBA-16 (EO/PO>1.5) is a cubic mesophase with a space group $Im\bar{3}m$ and a pore size of ~ 5.4 nm after calcination. The formation of nonionic SBA-15 involves an interaction like $[(EO)H_3O^+]XI^+$, which is weaker than the electrostatic (S^+I^-) interaction of MCM-41 (which also has hexagonal pore symmetry). The temperature at which SBA-15 surfactant can thus be removed is lower than that at which MCM-41 ionic surfactant can be removed. This is an important feature characteristic, given the low-temperature requirement of the backend-of-the-line (BEOL) process.

2.3 Integration Studies of Porous Dielectric Films

Porous dielectrics have a very low k value because they are highly porous. They are regarded as candidate IMD materials for sub-65 nm technology nodes. However, their high porosity raises many problems in the integration of porous ultralow- k dielectrics in the Cu damascene process. Many process steps, such as dry etching, wet cleaning and CMP, are severely affected by the pore structure of the porous dielectric. Studying integration-related issues thus becomes more urgent for porous dielectrics, especially silica-based porous ultralow- k films.

2.3.1 Mechanical Properties of Porous Materials

CMP processes can seriously damage films that do not have enough chemical strength. The mechanical properties of porous materials depend on their porosity and microstructure. The elastic modulus of a film is an important mechanical characteristic in understanding its deformation behavior. Three techniques are available for measuring the elastic modulus of thin films - the acoustic method [107, 108], the bending method [109-111] and indentation [112-123]. All results reveal a power-law dependence of the elastic modulus on the density,

and typical models of generic porous materials have been reported [124-128]. The most commonly used technique for measuring the hardness and elastic modulus of a thin film is nanoindentation [114-123]. However, accurate data can only be obtained by preventing the substrate from having any effect on the measured hardness and elastic modulus of the film, so the indentation depth can be only one tenth of the thickness of the film. Chiang *et al.* [115] measured the hardness and the elastic modulus of various films with low dielectric constants by nanoindentation. Jain *et al.* [116] fitted power laws to demonstrate that porous silica films have higher elastic moduli than other amorphous low- k materials. Miyoshi *et al.* [117] theoretically analyzed the effect of the arrangement of pores on the elastic modulus and the dielectric constant of porous silica films. They found that a periodic hexagonal arrangement of cylindrical pores has a higher elastic modulus than a random arrangement. Their group also reported the relationship between the mechanical strength and the Si-O asymmetric stretching vibration mode (LO_4) as determined by nanoindentation and FTIR [118]. Even though a dense oxide can have a native elastic modulus value as high as ~ 72 GPa, amorphous silica with over 50% porosity ($k < 2.5$) has a elastic modulus of lower than 10 GPa. Therefore, porous low- k materials must be chemically modified to increase their mechanical strength and face the CMP challenges [18, 119].

2.3.2 Copper Metallization

In a damascene scheme, as presented in Fig. 2.9, porous low- k dielectric is in contact with other materials, including metal (Cu), diffusion barrier (Ta or TaN) or hard mask/etch stop (SiN or SiC). The interaction between these materials and porous dielectrics is important in successful integration. Copper is an attractive material for IC metallization because of its low bulk resistivity and high resistance to electromigration. However, it is also known to be a fast diffuser through both dense SiO_2 and Si. Additionally, most dielectric materials poorly

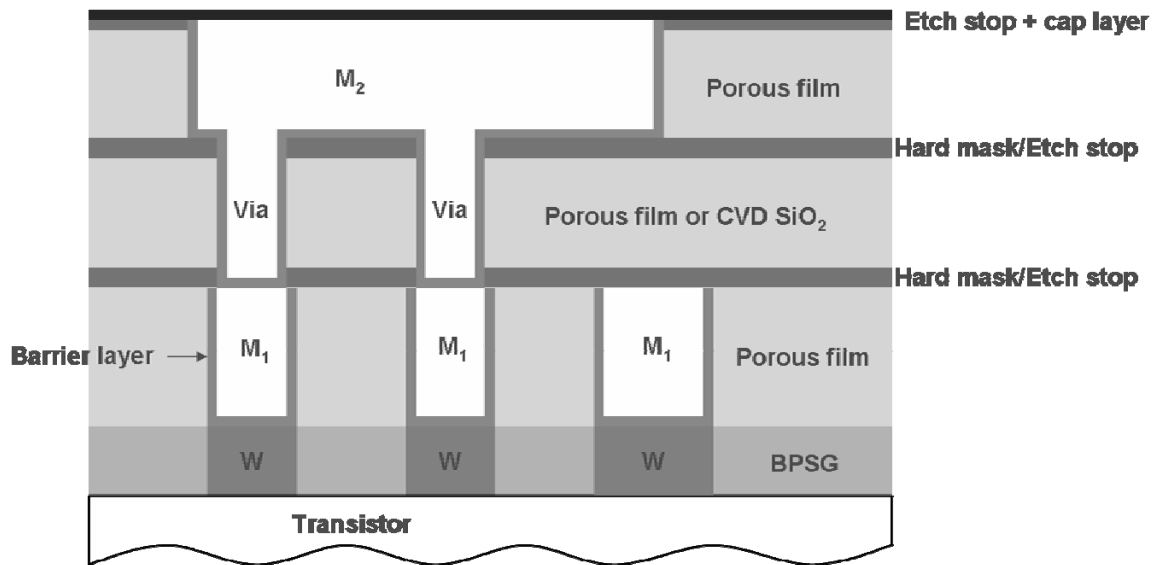


Figure 2.9 Schematic representation of a dual damascene copper metallization structure with porous low- k dielectric.

adhere to Cu and require a buffer layer to promote adhesion. The diffusion barriers for Cu tend to be refractory metals (such as Ti, Ta, W) and their compounds (e.g. TiN_x, TaN_x, WN_x). Most reports focus on Cu/barrier interactions and barrier failure mechanisms. Many potential barrier materials are currently under investigation, but Ta-based barriers are the most likely to be used because they provide a stable, adhesive interface between Cu and oxide [129]. Industrial products now have a Ta/TaN_x dual layer structure. Kumar *et al.* [130] has reported Ta, TaN and Ti as possible diffusion barriers for porous SiO₂. Rogojevic *et al.* [131] reported that a Ta/xerogel stack can be stable when annealed at a temperature of up to 450°C in an environment of N₂. Ta films buckle at high temperature or annealing time, because of the presence of amounts of oxygen that promote the oxidation of Ta. Tantalum and tantalum nitride films seem very suitable for use in Cu diffusion barriers with porous silica dielectrics.

Silicon nitride was used to form barrier/etch stop layers when the copper dual damascene structure was first introduced to the industry because of its excellent ability to prevent copper diffusion and satisfactory etching selectivity toward the oxide. However, the k value of the production silicon nitride typically exceeds 6.5, making the overall k value of the damascene

stack unacceptably high. Amorphous hydrogenated silicon carbide (α -SiC:H) has many dielectric characteristics that are similar to those silicon nitride: it can be used as a barrier/etch stop layer in the dual damascene structure, but it has a much lower dielectric constant ($k < 5$) than the PECVD silicon nitride, and, therefore, is preferred in a dual damascene structure [60]. α -SiC:H thin films are typically deposited by PECVD, and their properties, including microstructure, chemical and thermal stability, depend strongly on the process variables [132-142]. Properly choosing deposition parameters such as, in particular, the deposition temperature is, therefore, very important to the use of α -SiC:H in Cu interconnect technology.

2.3.3 Plasma Etching

Low- k films are very sensitive to plasma, and can be easily damaged in the etch/ash process. Porous silica films can be etched in fluorocarbon discharges, such as CF_4 , CHF_3 , C_3F_6 and C_4F_8 . Porosity and residual fluorocarbon impurities are important in the patterning of these films. Standaert *et al.* [143-146] have extensively studied the etching of porous silica and some conventional dielectric films using inductively coupled fluorocarbon plasma. They studied the etching rates of the xerogel films with various porosities and corrected the etch rates by applying the porosity factor $(1 - \Pi)$ [145]. Following this correction, the etch rates of xerogel are actually lower than those of conventional SiO_2 and depend strongly on the porosity of the film. They also found that more fluorocarbon polymerization occurred inside the pores at the xerogel surfaces than occurred in SiO_2 . Xerogel etching, therefore, was suppressed, especially in the xerogel films with high porosity and large pores. The fluorocarbon passivation layer typically forms on the sidewall when an oxide trench and via are patterned in a high-density plasma system. This process promotes anisotropic etching, and the obtaining of a pattern with a high aspect ratio, which nevertheless needs to be removed after etching.

Chapter 3

Experimental

This chapter describes the preparation of surfactant-templated mesoporous silica thin films. The parameters that govern the steps, - spin-coat, thermal treatment, surface modification and metallization - required to produce mesoporous silica low- k films are presented in detail. Finally, approaches used to characterize the mesoporous dielectric films are introduced.

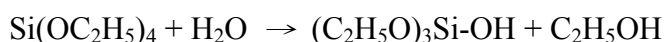
3.1 Preparation of Surfactant-Templated Mesoporous Silica



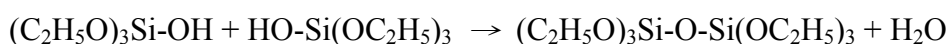
3.1.1 Preparation of Silica Precursor

Figure 3.1 presents the preparation of molecularly templated silica films. Mesoporous silica is derived from the conventional sol-gel process by self-assembly, and was supplied by Prof. K. J. Chao's lab (Dept. of Chemistry, NTHU, Taiwan). A silica precursor sol was prepared by mixing a solution of tetraethyl orthosilicate (TEOS), H₂O, HCl, ethanol and a nonionic surfactant, Pluronic P-123 (P123), in the molar ratio given in Table 3.1. The solution mixture was refluxed at 70°C for 90 min and then aged for 4 hours at room temperature.

As hydrolysis and condensation proceeds in the sol-gel process, TEOS is hydrolyzed:



The following water condensation reaction then takes place.



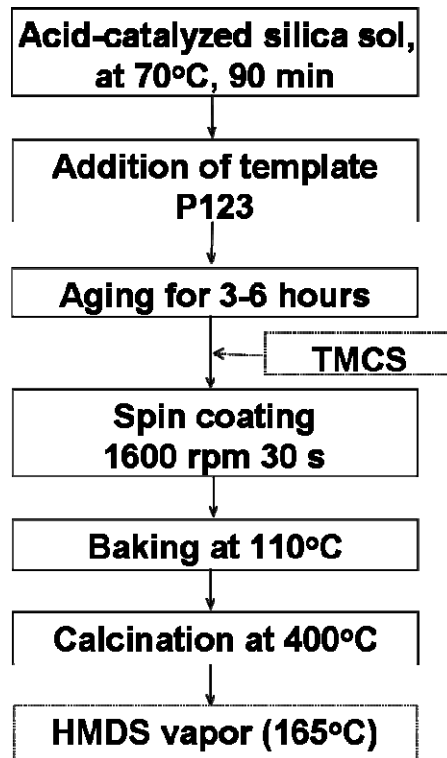


Figure 3.1 Process flow for the molecularly templated silica films.

and the alcohol condenses :



As gelation proceeds, water and ethanol are produced by the formation of siloxane (Si-O-Si) bonds.

Table 3.1 Precursor composition for the molecularly templated silica films.

Constituents	Molar ratio
TEOS	1
Ethanol	10-34
H ₂ O	3.5-5
HCl	0.003-0.03
Surfactant P123	0.008-0.03

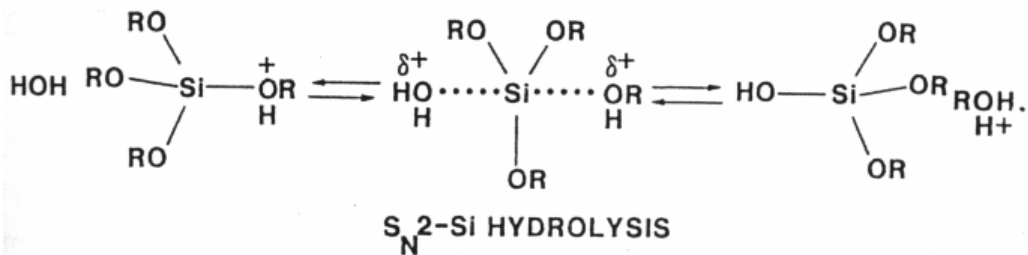
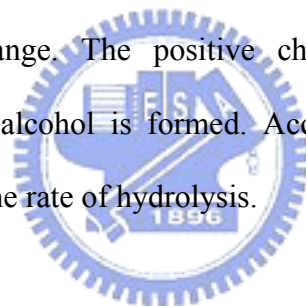


Figure 3.2 Acid-catalyzed hydrolysis proceeds by bimolecular nucleophilic displacement reactions [81].

Adding hydrogen chloride can also promote the hydrolysis of TEOS due to bimolecular nucleophilic displacement reactions (S_N2-Si reactions) [81]. Under acidic conditions, the alkoxide group of TEOS is protonated rapidly (Fig. 3.2), reducing the electron density of the silicon, resulting in an electrophilic state. The surrounding water thus more easily reacts with the silicon by charge exchange. The positive charge of the protonated alkoxide is correspondingly reduced and alcohol is formed. Accordingly, the steric crowding around silicon is reduced, increasing the rate of hydrolysis.



3.1.2 Deposition of Mesoporous Silica Thin Film

The precursor was spin-coated (Fig. 3.3) on precleaned 4 or 6 in. (100) *p*-type silicon wafers, which were precleaned by the standard RCA process. The spin speed and the spin time were controlled at 1600 rpm and 30 sec, respectively. The as-deposited samples were dried at 40°C for 2 h in an oven, and then baked at 110°C for 1 h to remove the aqueous solvent. The organic template molecules were removed from the mesoporous silica film by calcination at 400°C for 30 min in a furnace in flowing air. The as-calcined mesoporous silica thin film prepared as described, had a porosity of about 50% and pores whose sizes ranged from 3.5 nm to 5 nm.

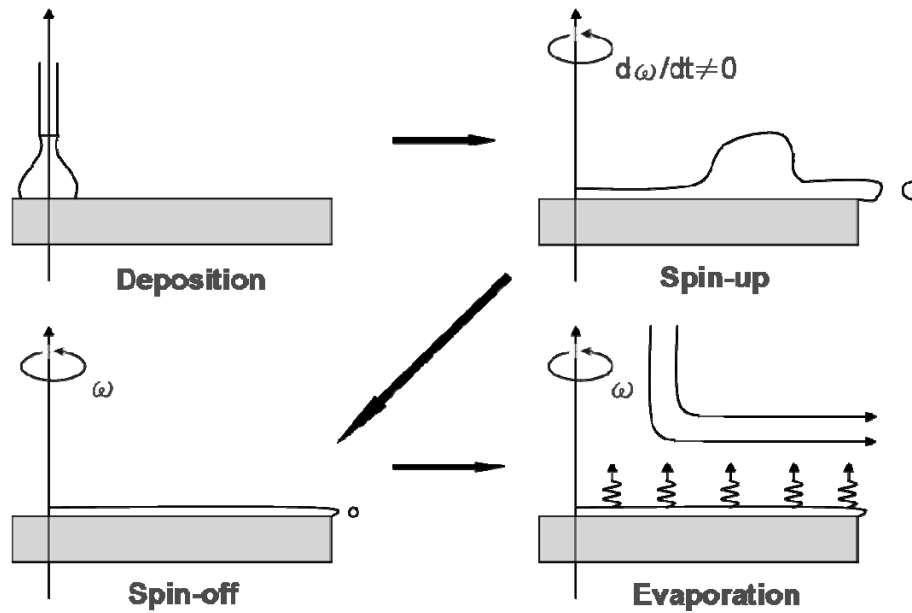


Figure 3.3 Stages of the spin-coating process [81].

3.1.3 Self-assembly of Surfactant

Figure 3.4 presents the self-assembly of the surfactant. The surfactant P123 has a hydrophobic and a hydrophilic part. Preferential evaporation during spin-coating induces the self-assembly of surfactants into micelles and micellar rods, followed by hexagonal mesophases [147]. During the spin-on process, the centrifugation disturbs the shape of the surfactant array, yielding a short-range ordered structure.

3.1.4 Hydrophobisation

The as-calcined mesoporous silica thin films have hydrophilic surfaces. The abundant surface silanol groups adsorb water, resulting in unsatisfactory electrical properties (such as k value and leakage current). Mesoporous silica films must be dehydrated and dehydroxylated to stabilize their electrical properties and achieve convincing reliability for further integration. In this work, the hydrophobicity of the mesoporous silica films is achieved primarily by

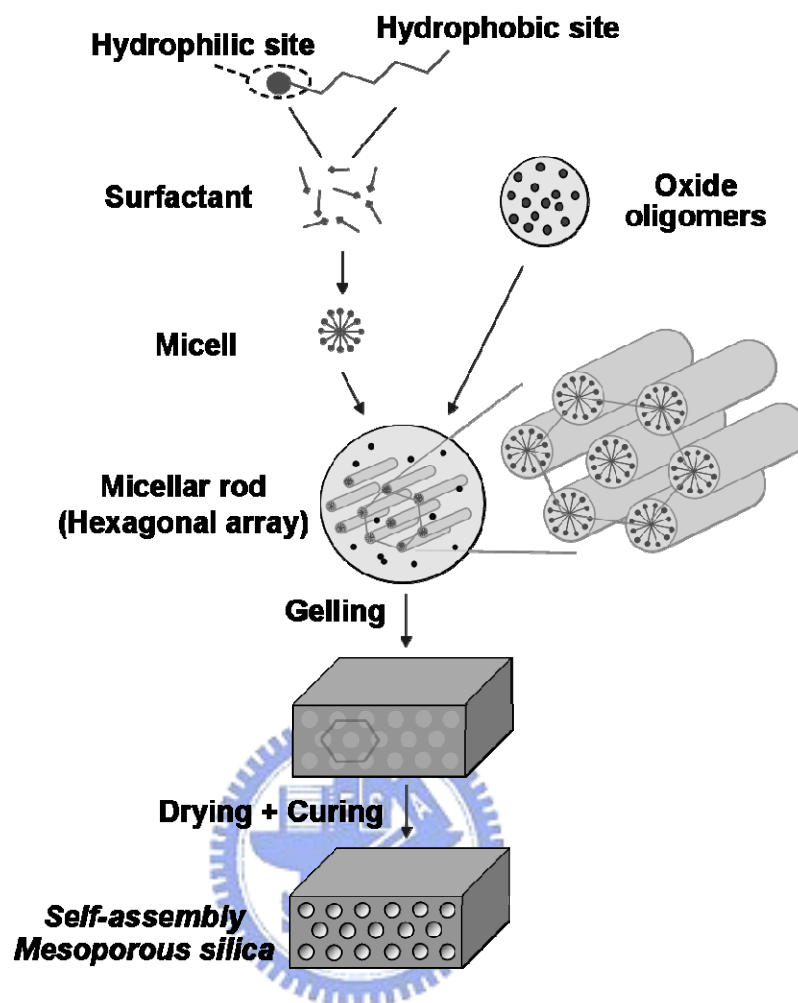


Figure 3.4 Self-assembly of surfactants and soluble silica.

silylation. Hexamethyldisilazane (HMDS) and trimethylchlorosilane (TMCS) were thus adopted, and many silanol groups could be replaced with trimethylsilyl groups in a short time. The treatment procedure differs little between HMDS and TMCS. In the preparation of TMCS-derivatized nanoporous silica films, the aged sol solution was mixed with TMCS (in a molar ratio to TEOS of 0.02-0.2) by vigorous stirring. The HMDS silylation, however, was performed following the calcinations, exposing the porous dielectric film to HMDS vapor at 165°C. Additionally, in some cases, H₂ plasma was adopted to passivate the unstable dangling bounds in the mesoporous silica thin films.

3.2 Metallization of Mesoporous Silica Thin Films

A film stack with the layer structure, SiN_x/Cu/Ta(N) (30 nm)/mesoporous-SiO₂ (200 nm)/SiO₂ (20 nm), was deposited on the *p*-Si wafer and annealed in N₂ ambient at various temperatures in order to study the thermal stability of the Cu-metallized mesoporous silica film. Partially nitrated Ta was sputter-deposited on the mesoporous silica layer as a Cu diffusion barrier in a sputtering system (SBH-3308RDE, ULVAC Taiwan Inc.) at a power of 500 W. The base pressure of the sputter chamber was $<6 \times 10^{-7}$ Torr. During the deposition of Ta(N), a gaseous mixture of Ar and N₂ was used in Ta nitridation with a gas flow ratio Ar:N₂=1:0.05. A Cu film was then deposited to a thickness of 300 nm on the Ta(N) layer at a power of 1500 W in the same sputtering chamber without breaking the vacuum. A thin layer of silicon nitride was deposited on the Cu layer by plasma-enhanced chemical vapor deposition (PECVD) at 250°C to protect the underlying Cu layer from oxidation during thermal treatments [148].

In the stress study, the film stack of α -SiC:H etch stop layer and the ultralow-*k* dielectric were prepared by depositing an α -SiC:H thin film to a thickness of ~50 nm on mesoporous silica thin film at various substrate temperatures (100–375°C) in an inductively coupled plasma (ICP) HDP-CVD system, using trimethylsilane (3MS, Si(CH₃)₃H) as the gas source. The ICP power and the flow rate of 3MS were kept at 500 W and 30 sccm, respectively.

3.3 Characterization of Mesoporous Silica Thin Films

3.3.1 Electrical Characteristics

A metal-insulator-semiconductor (MIS) capacitor structure was used to measure electrical characteristics. An Al film with a thickness of 500 nm was evaporated on the backside of the Si wafer as an electrode. In the deposition of a metal electrode, the

mesoporous silica film was covered with a shadow mask, which has a dot array pattern, as presented in Fig. 3.5. The Cu/Ta(N) electrode on the mesoporous silica layer thus has a mesa structure with a diameter of 0.2-0.8 mm. The dielectric constant and the leakage current

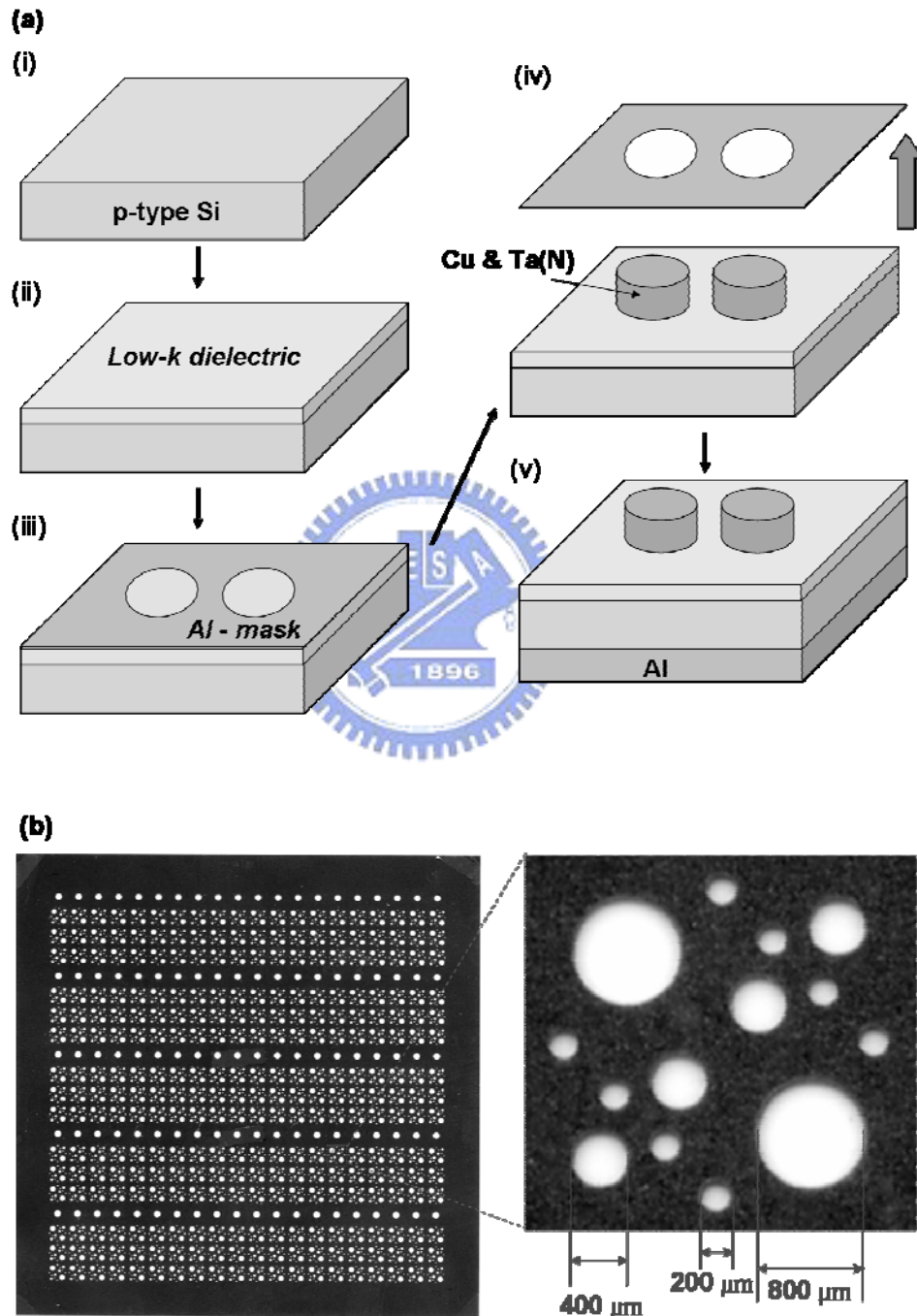


Figure 3.5 Preparation scheme for metal-insulator-semiconductor (MIS) capacitor structure (a), and Al shadow mask with dot array patterns (b).

density were measured using a Keithley model 590 CV meter and an HP 4156A semiconductor parameter analyzer, respectively. The bias-temperature stress (BTS) test was adopted to study mobile ion drift in mesoporous films. During the BTS test, the capacitors were biased up to ± 20 V at 150°C .

3.3.2 Mechanical Strength

The hardness and elastic modulus of the mesoporous silica thin films were measured using a Nano Indenter XP (MTS Corp.) with a diamond tip with a Berkovich geometry. This approach can determine the hardness and elastic modulus depth profiles at depths down to a few tens of nanometers by progressively increasing the applied load from 0.5 to 20 mN. A holding segment was inserted in the end of each loaded segment to allow time for the system to equilibrate before it was unloaded. Then, unloading was performed at a constant rate. The early unloaded portion was used to calculate the stiffness, and the holding segment was used to correct the thermal drift. The indentation depth was 150 nm, but both the elastic modulus and the hardness were determined from the first 10% of the film thickness to avoid the substrate effect. About ten identical indents were made in each test to ensure reproducibility and accuracy.

According to the elastic contact theory [149], the elastic modulus and the hardness of the film can be determined from the initial unloading stiffness S , which is the tangent of the curve plotted from the initial unloading data (Fig. 3.6):

$$h_c = h_m - h_s = h_m - \varepsilon \frac{P_m}{S},$$

where h_c is the contact depth, h_m the maximum depth of the elastic deformation under load, h_s the displacement of the surface at the perimeter of the contact, P_m the maximum load and ε a geometrical constant. For a Berkovich indenter, the project area A of the actual contact can be

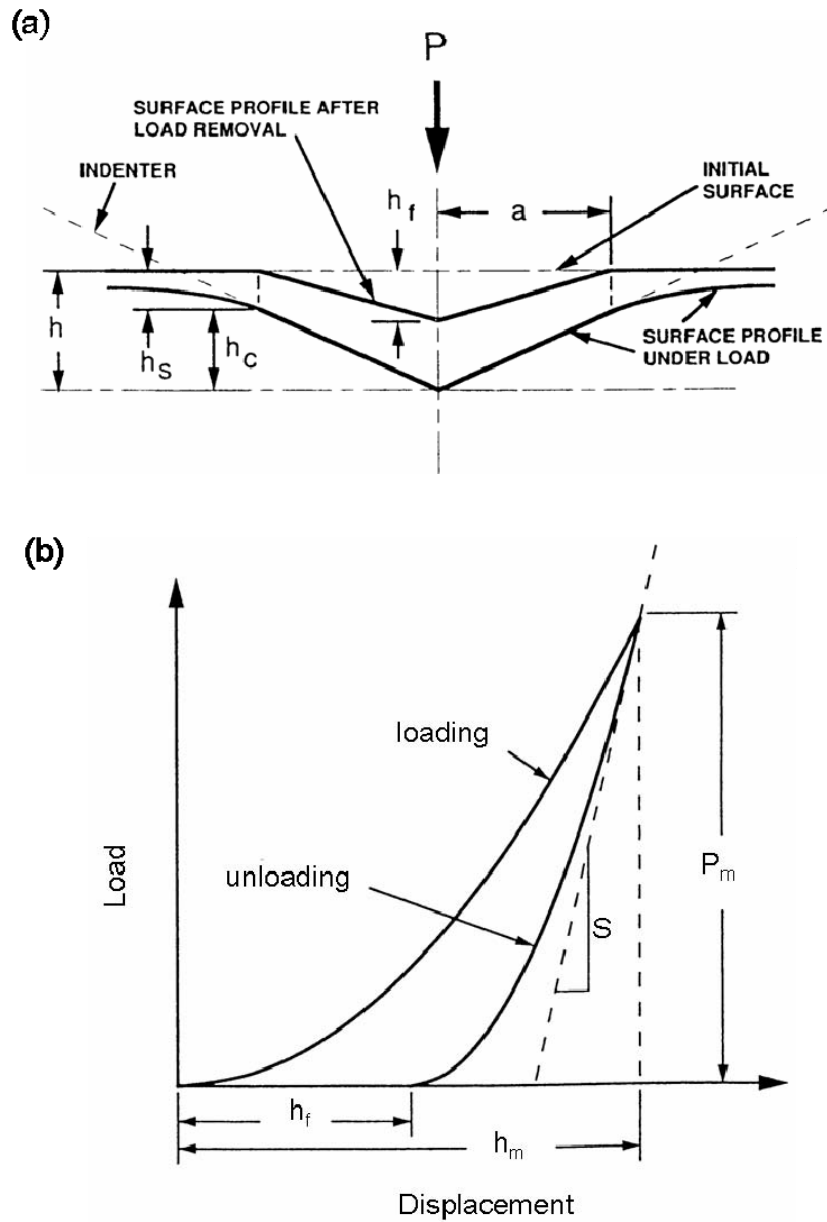


Figure 3.6 Schematic representation of (a) a cross section of a surface through an indentation, and (b) the load-displacement relationships [149].

expressed as a function of the contact depth h_c [150]:

$$A(h_c) = 24.5h_c^2 .$$

Once the contact area A is known, the hardness of the material H is given by,

$$H = \frac{P_m}{A} . \tag{3.1}$$

The reduced elastic modulus E_r can be derived from the contact stiffness S :

$$S = \frac{dP}{dh} = \frac{2\beta}{\sqrt{\pi}} E_r \sqrt{A}.$$

The factor β is a geometrical constant of the indenter and equals 1.034 for Berkovich. The elastic modulus of the material E is given by,

$$\frac{1}{E_r} = \frac{(1-\nu^2)}{E} + \frac{(1-\nu_i^2)}{E_i}, \quad (3.2)$$

where ν is the Poisson's ratio of the material, and E_i and ν_i are the elastic modulus and the Poisson's ratio of the indenter, respectively. $E_i=1141$ GPa and $\nu_i=0.07$ were used to calculate the elastic modulus of the test samples.

3.3.3 Film Stress

A Tencor FLX-2320 stress measurement system was employed to measure the film stress. The stress measurement system optically detects changes in the wafer curvature and calculates the film stress using the standard Stoney equation [151]. Figure 3.7 presents a diagram of the principle of film stress measurement by optical reflection. The Tencor FLX-2320 has two 4 mW solid-state lasers - a Class IIIA laser with a wavelength of 670 nm, and a Class IIIB laser with a wavelength of 750 nm. A 670 nm Class IIIA laser was used in the stress studies. The laser was directed at a sample surface with a known spatial angle and then reflected to a photodiode. When the laser beam scans across the sample surface, the displacement of the reflected beam is determined by the position-sensitive photodiode. The change in the displacement of the reflected beam is proportional to the change in the angle between the incident laser beam and the surface of the wafer. It is thus proportional to the inverse radius of curvature. The changes in the radius of curvature yield the relative stress in the film according to Stoney's equation,

$$\sigma_f = \frac{E_s t_s^2}{6(1-\nu_s) t_f} \left(\frac{1}{r} - \frac{1}{r_0} \right), \quad (3.3)$$

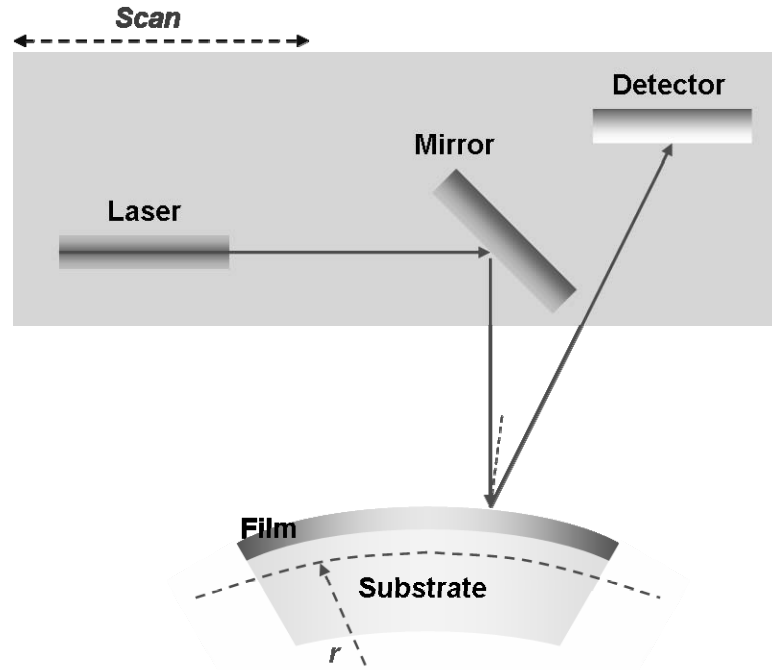


Figure 3.7 Principle of film stress measurement by optical reflection method.

where r_0 and r are the radius of the curvature of the wafer before and after the thin film was deposited, respectively. E_s and ν_s are the Young's modulus and Poisson ratio of the bare substrate, and are related to the orientation of single crystal substrates. For the Si substrate E_s was 131 GPa and ν_s was 0.278 [152]. The factor $E_s / (1 - \nu_s)$ is the substrate biaxial modulus. The thickness t , with subscripts "s" and "f" is the thickness of the substrate and the film, respectively. For the film stack, t_f is substituted for the total thickness of the film stack to yield the final stress of the films. The film thickness was confirmed by SEM and the value of the thickness term in the equation was corrected.

The thermal stress of the film in elastic deformation is given by [153],

$$g = \frac{d\sigma}{dT} = (\alpha_s - \alpha_f) \cdot M_f,$$

where g is the gradient of the stress σ as a function of temperature T , and α_s and α_f are the coefficients of thermal expansion (CTE) of the substrate and the film, respectively. M_f is the

biaxial modulus of the film. When the mesoporous silica thin films are deposited on two substrates with different CTEs, two gradients g_1 and g_2 of the stress-temperature curve are obtained. The CTE of the mesoporous silica thin film then can be calculated from,

$$\alpha_f = \frac{g_2 \cdot \alpha_1 - g_1 \cdot \alpha_2}{g_2 - g_1}, \quad (3.4)$$

and the biaxial modulus of the film, related to the film elastic modulus E_f and Poisson's ratio ν_f , is given by the following equation;

$$M_f = \frac{g_2 - g_1}{\alpha_2 - \alpha_1}. \quad (3.5)$$

In making measurements of CTE, Ge (CTE 5.84 ppm/°C) was used as a substrate in conjunction with Si (CTE 2.61 ppm/°C) [154]. Both substrates were 150 μm thick and had a (100) orientation. The thermal cycling experiment involved three cycles to stabilize the films, and only the third cycle was used to calculate CTE. In each cycle, the temperature was ramped from room temperature to 400°C at a rate of 2 °C/min before being cooled down to room temperature at the natural cooling rate of the chamber.

3.3.4 Chemical and Thermal Stability

The chemical structure and thermal stability of the mesoporous silica films were studied by Fourier transformation infrared spectroscopy (FTIR) (ASTeX PDS-17), thermal deposition mass spectroscopy (TDS) (TDS-APIMS, Hitachi Tokyo Electronics) and Auger electron spectroscopy (AES) (VG Scientific MICROLAB 350).

3.3.5 Microstructure, Surface Morphology and Optical Properties

Transmission electron microscopy (TEM) (JEM-2010F) was used to study the microstructure of the film stack. The surface morphology of the mesoporous films was

elucidated by atomic force microscopy (AFM) and scanning electron microscopy (SEM). XRD is adopted to study the pore microstructure of the mesoporous films. The optical refractive index of the film was measured using an n&k analyzer 1280. The film density was also applied to determine the porosity of the silica using the empirical equation derived from the Dale-Gladstone relationship [155]:

$$\Pi = \frac{(1.458 - n)}{0.458} \times 100 . \quad (3.6)$$



Chapter 4

Dielectric Properties and Hydrophobicity of Surfactant-Templated Mesoporous Silica Films

This chapter briefly discusses the dielectric characteristics and the hydrophobicity of the mesoporous silica thin films. Pores are introduced into the spin-on silica-based dielectric by the templation method to yield an ultralow k . However, as-calcined mesoporous silica films are typically rich in residual silanol groups, which do not participate in the condensation reaction, and thus adsorb water molecules easily. The hydrophilic mesoporous silica films must be functionalized to achieve an acceptable hydrophobicity and thus maintain the stability of the dielectric properties, typically using trimethylsilylation treatments. The hydrophobicity of a calcined silica film was demonstrated to be effectively improved by *in-situ* trimethylchlorosilane (TMCS) silylation in sol precursor solution, and/or by a hexamethyldisilazane (HMDS) vapor post-treatment; with further plasma treatments, a dielectric constant of less than 2.0 was obtained.

4.1 Relationship between Surfactant and Dielectric Constant of Mesoporous Silica Thin Films

Surfactant-templating strategies can be used to make controlling the porosity and the pore periodicity of the porous silica films easier than by the traditional sol-gel process. The temperature required to remove the templated molecules should not exceed 450°C, to ensure the usefulness of this method in IC production. Figure 4.1 presents the FTIR spectra obtained

at various calcination temperatures and times for removing the surfactant P123. The surfactant P123 was used as an organic template herein because its interaction with silica matrix is weak, and thus associated with a low process temperature. As presented in Fig. 4.1, the peaks range from 2830 to 3020 and from 1270 to 1520 cm^{-1} , which results are attributable to the surfactant P123 [156]. The samples calcined at 200 (Fig. 4.1a) and 300 $^{\circ}\text{C}$ (Fig. 4.1b) for 90 min retained some surfactants in the silica films. Further increasing the calcination temperature accelerated the rate of surfactant degradation and shortened the process time. The FTIR spectrum obtained after calcinations at 400 $^{\circ}\text{C}$ (Fig. 4.1d) reveals that the organic templates and residual water were efficiently removed from the film. The best condition for thermal calcination is thus concluded to be 400 $^{\circ}\text{C}$ for 30 min, as determined from the IR spectra. This temperature is exactly that used by IC manufacturers. A much lower calcination temperature may be

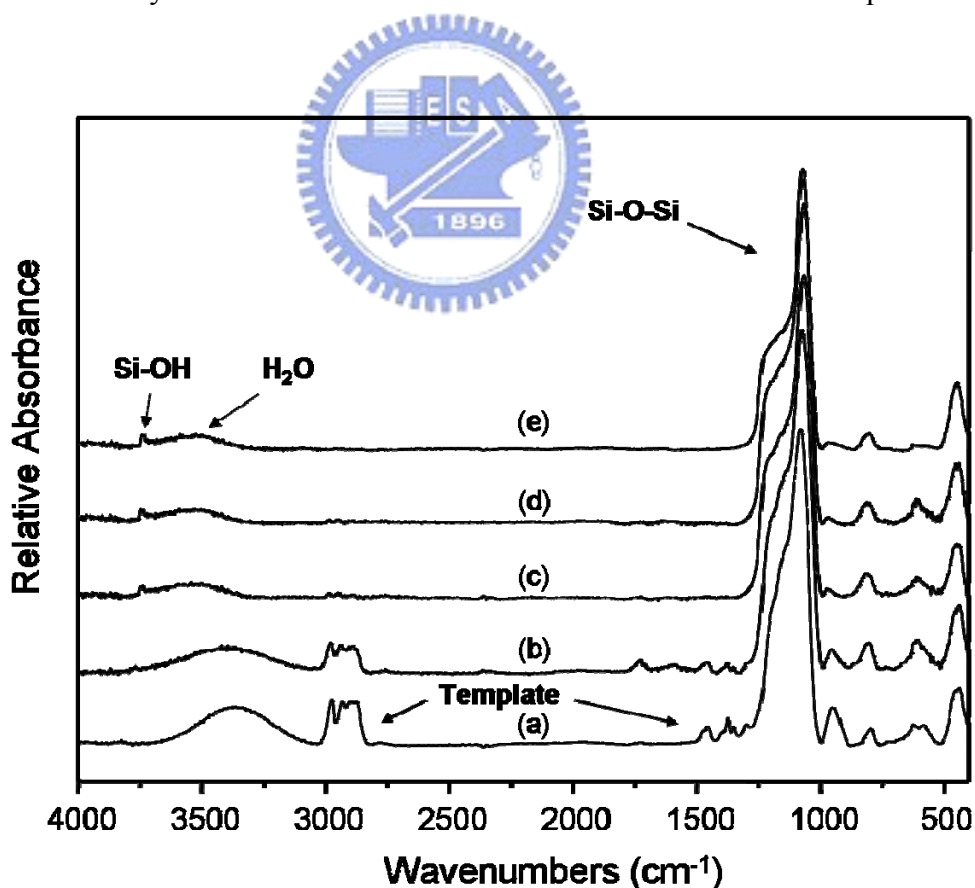


Figure 4.1 FTIR spectra of (a) the as-baked film, and the as-baked film followed by calcination at (b) 200 $^{\circ}\text{C}$ for 90 min, (c) 300 $^{\circ}\text{C}$ for 90 min, (d) 350 $^{\circ}\text{C}$ for 30 min, and (e) 400 $^{\circ}\text{C}$ for 30 min.

achieved combining this process with other chemical reactions, like oxygen plasma treatment, but doing so may cause plasma damage to the film, following dielectric degradation [157].

Since the surfactant is the main cause of pore formation in mesoporous films, the quantity added to the precursor solution may influence the dielectric constant. As presented in Fig. 4.2, the refractive index of the mesoporous silica thin film declines with the surfactant/TEOS molar ratio, indicating that increasing the surfactant content dose increases the porosity of the film. The dielectric constant of the mesoporous silica film therefore declines as the surfactant molar ratio increases and tends toward unity. However, merely increasing the surfactant ratio may cause other problems, such as film cracking. Figure 4.3 presents optical images of the mesoporous silica thin films prepared from a precursor P123/TEOS in molar ratios of 0.01, 0.02 and 0.03. Crack traces are observed in silica films with molar ratios of 0.02 and 0.03. They are more serious when the molar ratio is 0.03. Film cracking is caused by the excessive addition of surfactant P123, which generates high strain in

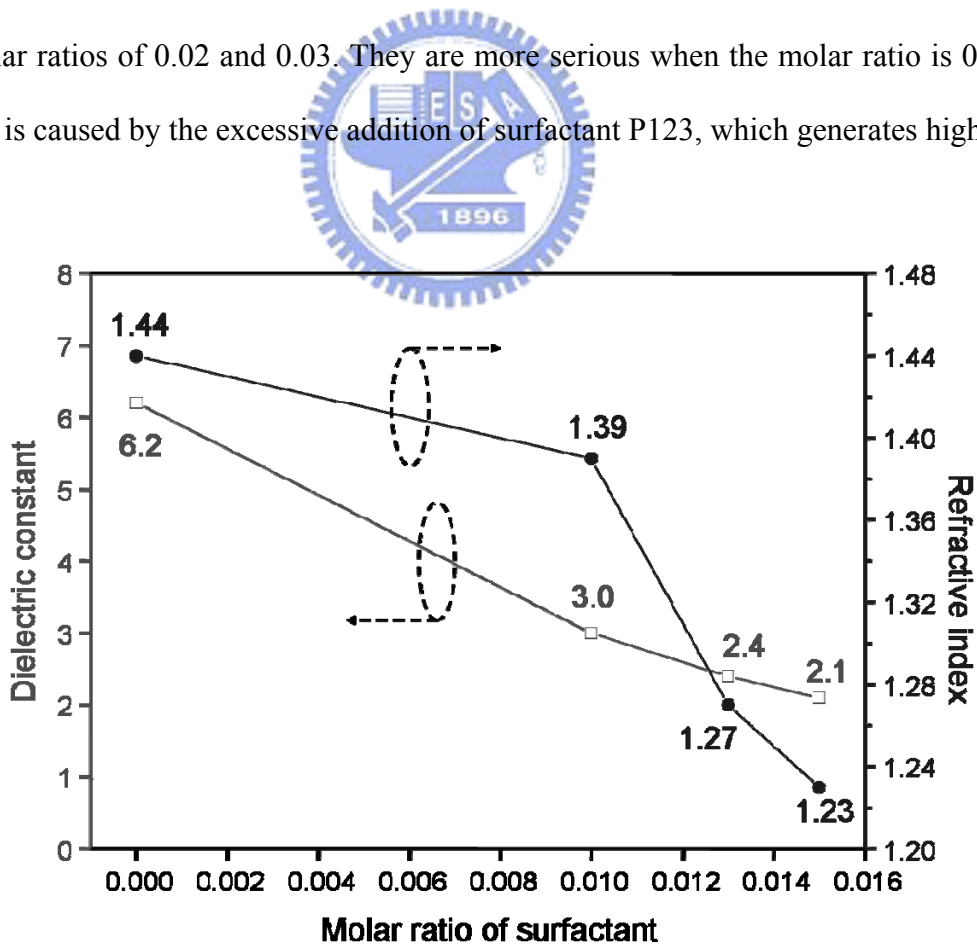


Figure 4.2 Dielectric constant and refractive index of the mesoporous silica thin films as a function of surfactant/TEOS molar ratio.

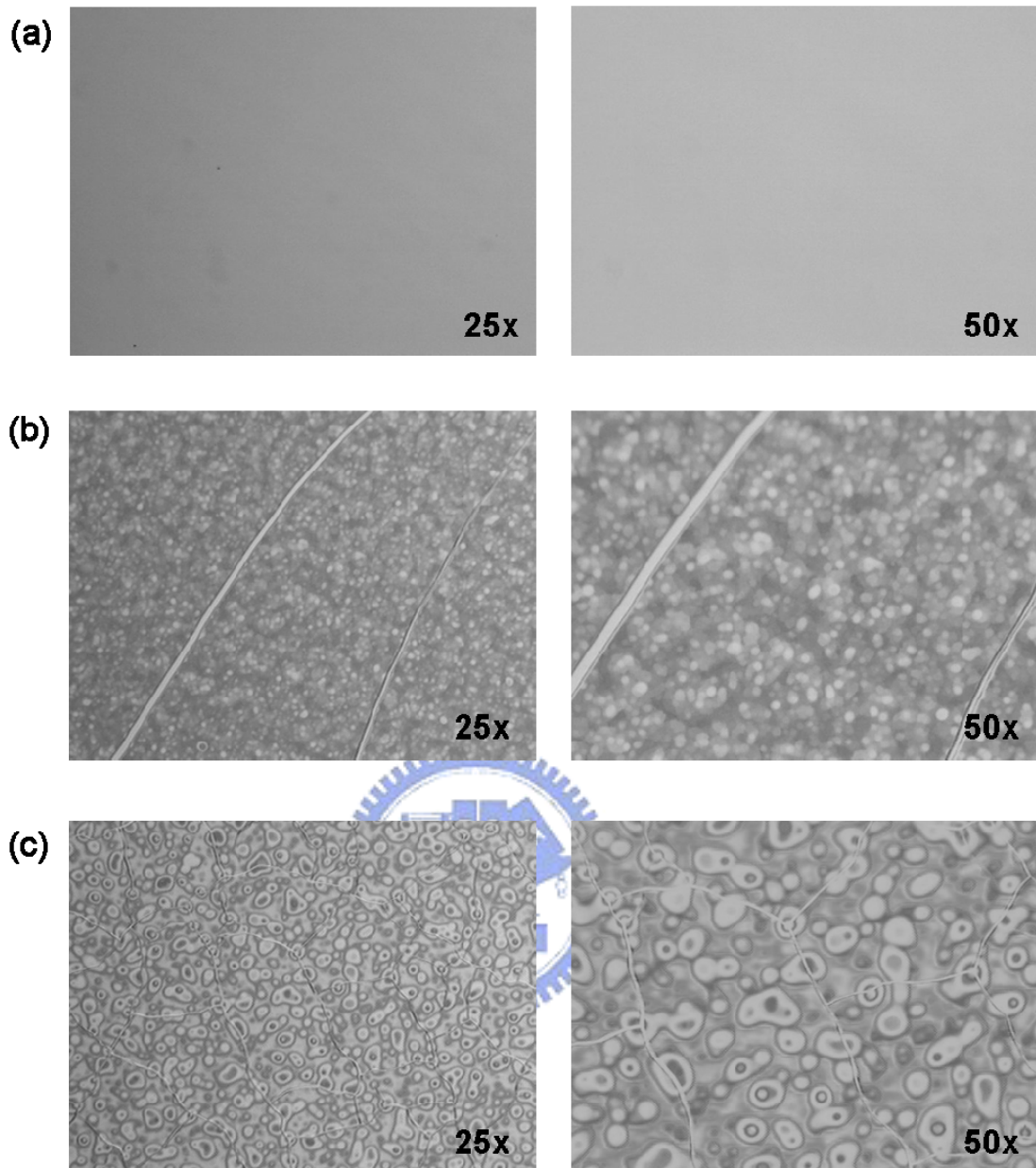


Figure 4.3 Surface morphologies of the mesoporous silica thin films prepared from a precursor P123/TEOS in molar ratios of (a) 0.01, (b) 0.02 and (c) 0.03.

the silica matrix. Changing the water/solvent ratio may ease the strain and relax the limitation on the surfactant capacity. This issue is beyond the scope of this work because the vain pursuit of dielectric limitations is unrealistic in IC integration. In fact, the main problem associated with porous silica dielectrics is the adsorption of water. Notably, all of the dielectric constants of the mesoporous silica thin films in Fig. 4.2 were measured following HMDS hydrophobisation. Mesoporous silica thin films without any hydrophobisation typically

adsorb water in a short time, yielding a k value of over 4.0, which is the dielectric constant of a dense oxide.

4.2 Methylsilylation of Mesoporous Silica Thin Films

Chapter 3 stated that TEOS is hydrolyzed and forms silanol (Si-OH) terminal bonds in a sol-gel process. Some of these silanol bonds are eliminated in the condensation reaction but many remain at the inner surfaces of the pores, even though the film underwent calcination at 400°C. Figure 4.4 presents the FTIR absorption spectra of the mesoporous silica thin films and Tables 4.1 and 4.2 summarize their associated IR vibrations [158, 159]. The IR spectrum in Fig. 4.4a reveals that -OH absorption ($\sim 3600\text{ cm}^{-1}$) occurs in the as-calcined mesoporous silica thin film. The as-calcined mesoporous silica films are rich in residual OH groups, and thus are liable to adsorb many water molecules ($\sim 3300\text{ cm}^{-1}$). Many silica-based porous materials are also reported to exhibit this hydrophilic characteristic, and their Si-OH bonds must be passivated by hydrophobic surface groups [160, 161]. Two hydrophobising agents, HMDS and TMCS, can react with the terminal silanol groups to yield trimethylsilyl groups by silylation. The FTIR spectra of Figs. 4.4b and c present the chemical microstructural evolution of post-treated HMDS and TMCS-derivatized mesoporous silica thin films, respectively. Both spectra have two further peaks, at 1258 and 2965 cm^{-1} , attributed to Si-CH₃ stretching and the methyl segment of the trimethylsilyl group, which is bound to the pore surface. Fewer silanol and water signals in the FTIR spectra were observed following trimethylsilylation, indicating that HMDS and TMCS treatment can successfully increase the hydrophobicity of the mesoporous silica films. Plausible mechanisms of the methylsilylation by HMDS and TMCS have been reported. Gunko *et al.* [162] found that the HMDS molecule has a high reactivity with silica surface silanol group because of its basic nitrogen. The electrophilic Si on HMDS attacks the nucleophilic oxygen of a free surface silanol to generate

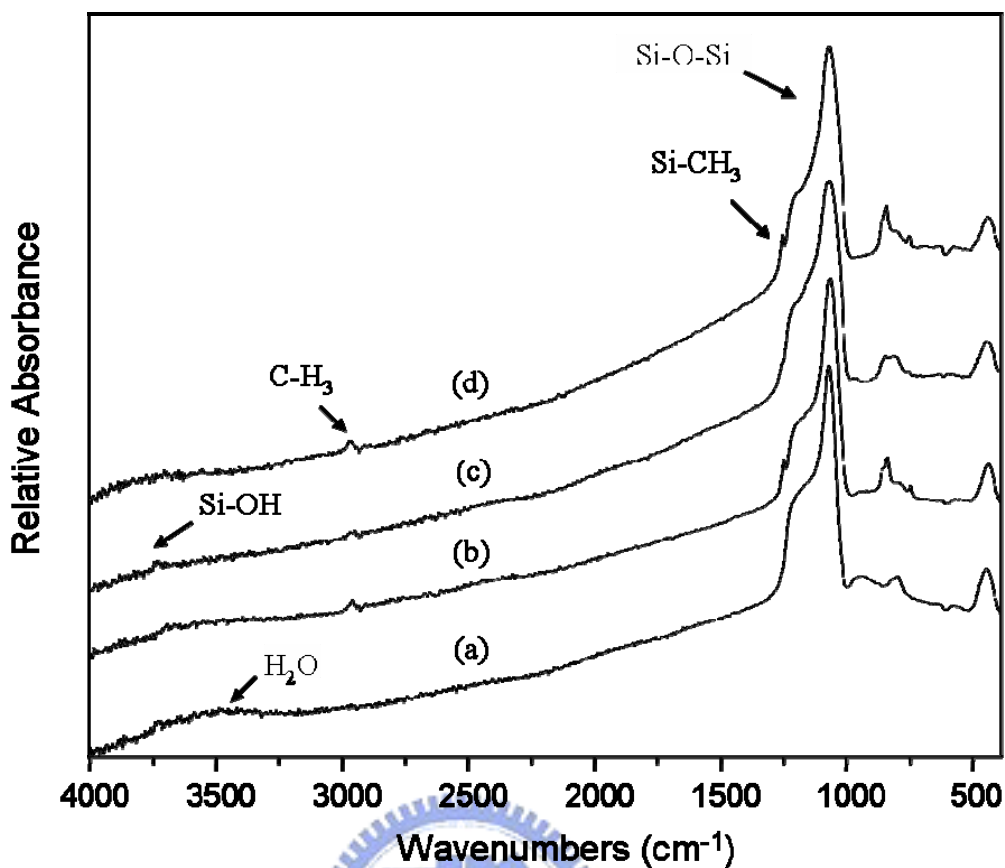


Figure 4.4 FTIR spectra of mesoporous silica thin film; (a) as-calcined film, (b) as-calcined film after HMDS treatment for 30 min, (c) as-calcined TMCS (10% molar ratio) derivatized film, (d) TMCS derivatized film after HMDS treatment for 30 min.

Table 4.1 FTIR absorption bands in the mesoporous silica films.

Wavenumbers (cm ⁻¹)	Assignments
3200-3700	Silanol SiO-H stretching
1000-1200	Si-O-Si Asymmetric stretching
~940	Silanol Si-O stretching
~805	Si-O-Si Symmetric stretching
~450	Si-O-Si bending
~1258	Si-(CH ₃) ₃ stretching
~840, ~760	Si-(CH ₃) ₃ rocking
~2965	C-H stretching

Table 4.2 FTIR absorption bands in the O-H stretching region.

Wavenumbers (cm ⁻¹)	Assignments
3300-3500	H-bonded H ₂ O (O-H stretching)
3650-3800	O-H stretching not involved in hydrogen bonding (isolated OH and terminal OH)
3690	Hydroxyl terminals
3750	Isolated surface silanols Si-OH (sharp peak)
3200-3650	H-bonded Si-OH in chain (Si-OH stretching)

the trimethylsilyl group, as presented in Fig. 4.5. The surface silanol groups on the interior of the pore can thus be passivated as long as the pore structure is open and the pores are large. (The length of a HMDS molecule is reported to be ~1.022 nm [163].) Tsai *et al.* [15] reported that TMCS added to the sol precursor reacts rapidly with silanol groups of linear silica in an acidic medium. Many terminal trimethylsilyl groups formed on the edge of silica branches and isolated them, affecting the degree of linkage of silica, as will be discussed in Chap. 5.

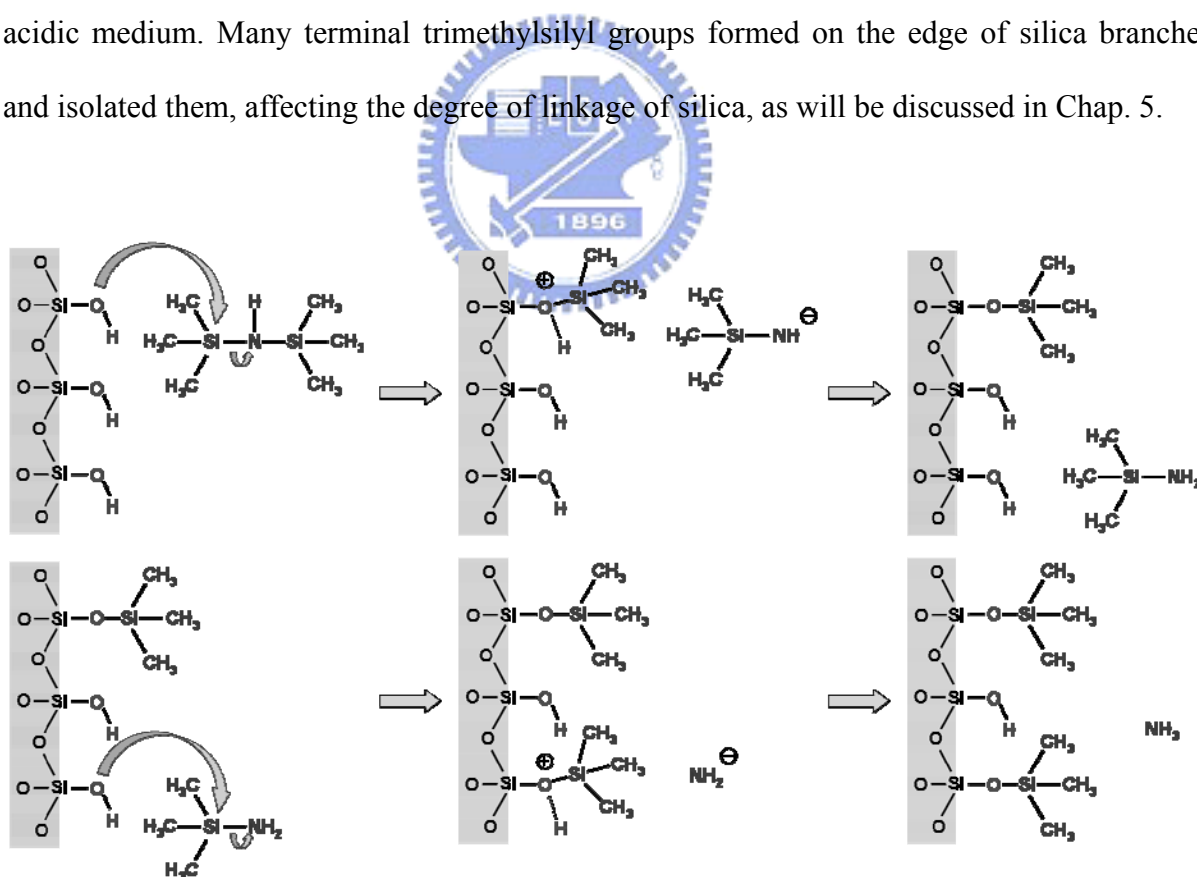


Figure 4.5 Trimethylsilylation of mesoporous silica thin films by HMDS. A HMDS molecule reacts with surface silanol group, to give a silylated pore surface and (CH₃)₃SiNH₂, which then reacts with a Si-OH group yielding NH₃ as byproduct.

Figure 4.6 presents the thermal desorption spectra of H₂O ($m/e = 18$) for the as-calcined and the HMDS-treated mesoporous silica thin films. The spectrum of the as-calcined film (dashed line) reveals a large amount of water that evolved from the as-calcined mesoporous silica as the sample was heated. Three desorption peaks are clearly seen. The peak at the lowest desorption temperature ($<80^{\circ}\text{C}$) is associated with physisorbed water, and that at about 230°C is probably associated with weakly hydrogen-bonded water molecules [164, 165]. The peak at the highest desorption temperature is associated with the decomposition of silanol groups on the pore surface [164, 165]. HMDS vapor treatment greatly mitigates the adsorption of water in the mesoporous silica thin film, as presented in the TDS result (solid line). The distinct drop in intensity of the OH-related desorption peak reveals that the HMDS treatment can effectively remove most silanol surface groups, which finding is supported by the FTIR study referred to above.

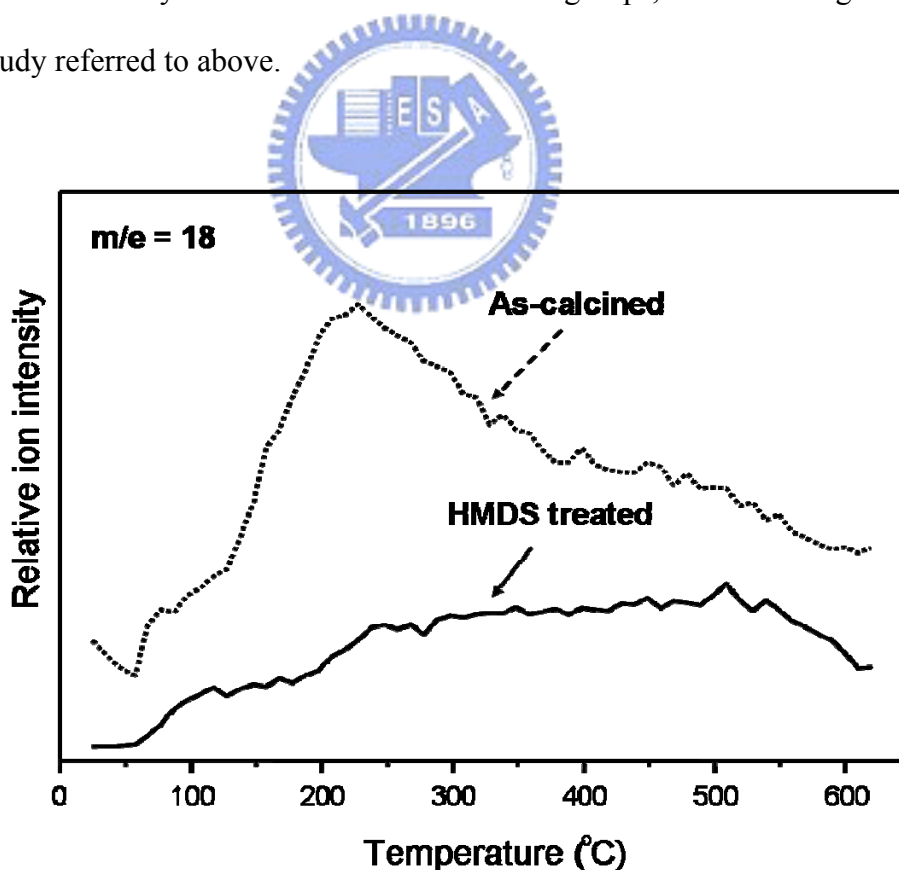


Figure 4.6 Thermal desorption spectra of H₂O ($m/e = 18$) for the as-calcined (dash line) and the HMDS treated (solid line) mesoporous silica thin films.

Trimethylsilylation also improves the dielectric characteristics of the mesoporous silica thin film. The dielectric constant of the as-calcined mesoporous silica film was measured to exceed 20, because of the surface Si-OH on the pore walls and the absorbed water inside the mesoporous film. Figures 4.7 and 4.8 plot the capacitance-voltage ($C-V$) curve of the silica

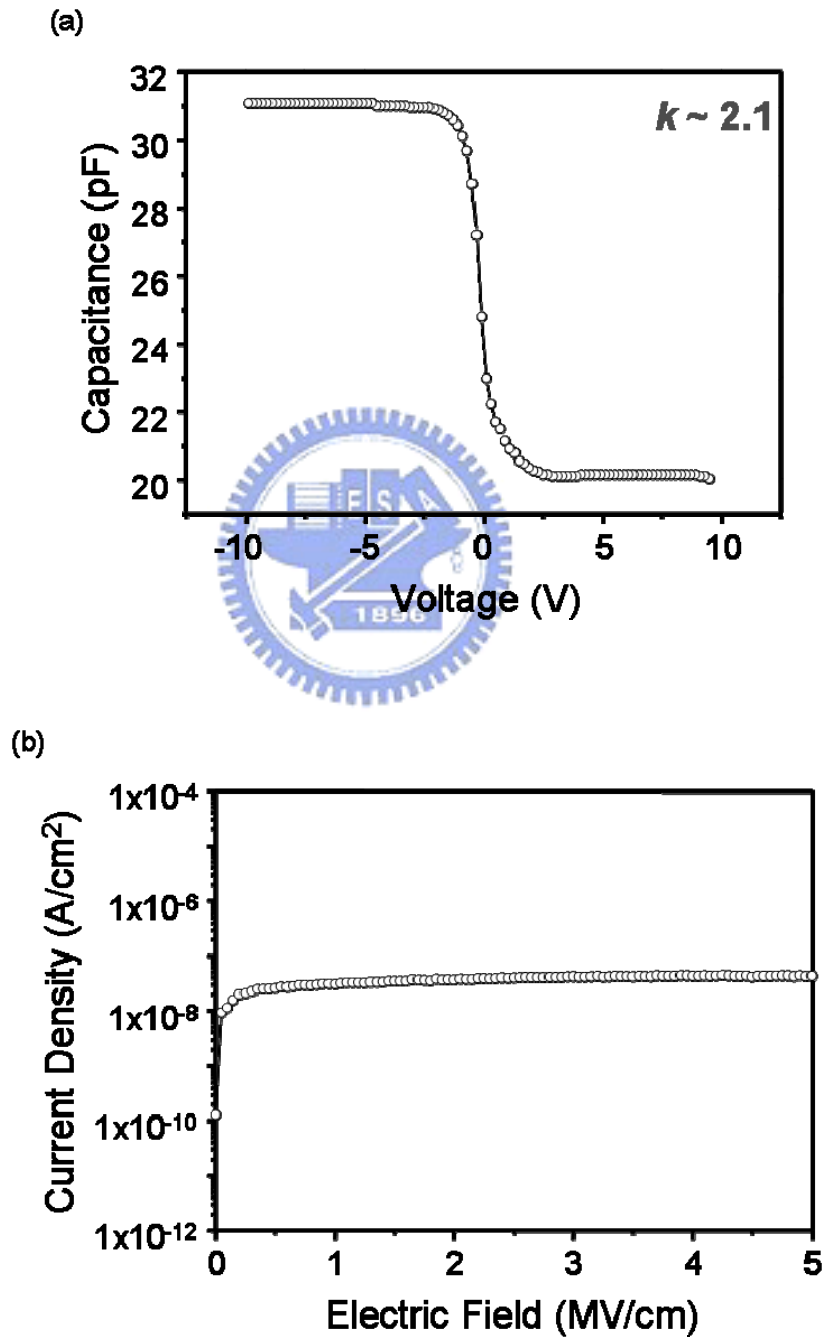


Figure 4.7 High frequency (1 MHz) $C-V$ characteristic and leakage current of mesoporous silica film after HMDS treatment.

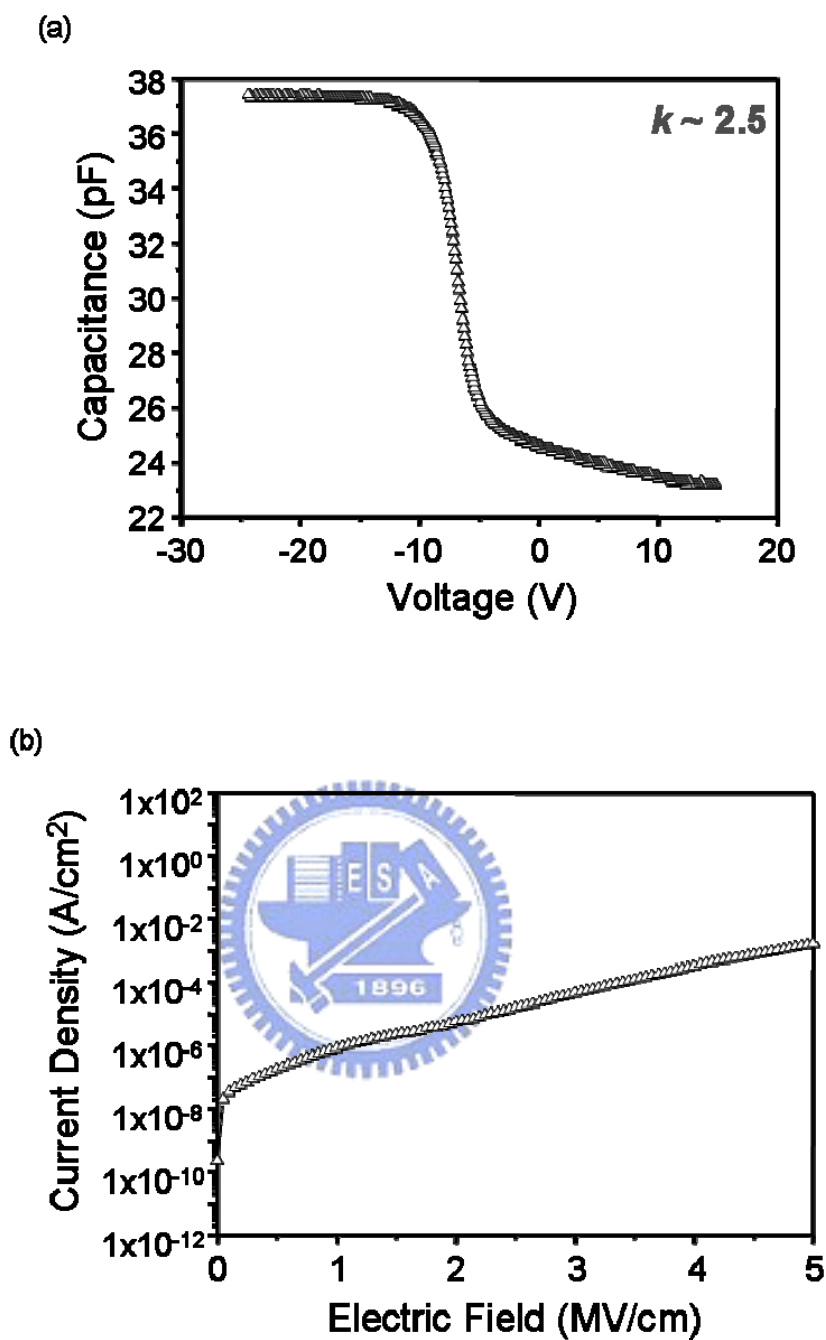


Figure 4.8 Capacitance-voltage curve and leakage current for TMCS derivatized mesoporous silica film.

films and the leakage current following HMDS and TMCS treatments, respectively. The dielectric constant obtained from the C - V curve reveals a k value that is much lower than that of the as-calcined film. The TMCS derivatized mesoporous silica film has a k value of ~ 2.5 and a leakage current density of 6.0×10^{-6} A/cm² at an electric field of 2 MV/cm. An HMDS

vapor-treated film can have a much lower k value, 2.1, and a leakage current of the order of 10^{-8} A/cm². These improvements in the dielectric properties of the mesoporous silica thin film quantitatively reveal the effects of hydrophobisation. Therefore, HMDS vapor treatment of the mesoporous silica thin film seems more effective than TMCS derivatization in eliminating silanol groups and increasing the hydrophobicity of the film.

4.3 Improvement of Dielectric Characteristics by Hydrogen Plasma Treatment

Further treatment with reductive hydrogen plasma can improve the dielectric characteristics of the mesoporous silica thin film. According to earlier works [20], low-power H₂ plasma-assisted treatment can reduce the dielectric constant from 2.6 to 2.2. Figure 4.9 presents the FTIR spectra of mesoporous silica films following H₂ plasma treatment for 3 min and further exposure to HMDS vapor. Hydrogen radicals formed from the H₂ plasma can react with ether nonbridged silicon atoms or Si-OH centers in the mesoporous film (Fig. 4.10). Therefore, the intensity of Si-OH at 3750 cm⁻¹ decreased when the mesoporous silica film was treated with H₂ plasma. This result reveals that the number of surface silanols decreases considerably, and methylsilylation on the pore surface thus become more difficult to execute. As indicated by the IR spectra of Figs. 4.9(c) and (d), the long duration of the H₂ plasma treatment limits HMDS silylation, resulting in ambiguous Si-CH₃ absorption. Once the HMDS silylation had been completed before H₂ plasma treatment, the Si-CH₃ absorption peak at 1258 cm⁻¹ exhibited a very little change in Fig. 4.11, indicating less plasma damage associated with hydrophobicity. Since Si-H bonds (bonding strength ≤ 299.2 kJ/mol) are weaker than Si-C bonds (bonding strength ~ 451.5 kJ/mol) [166], they are more easily destroyed during some IC process leaving defects or charges trapped in the center of the silica

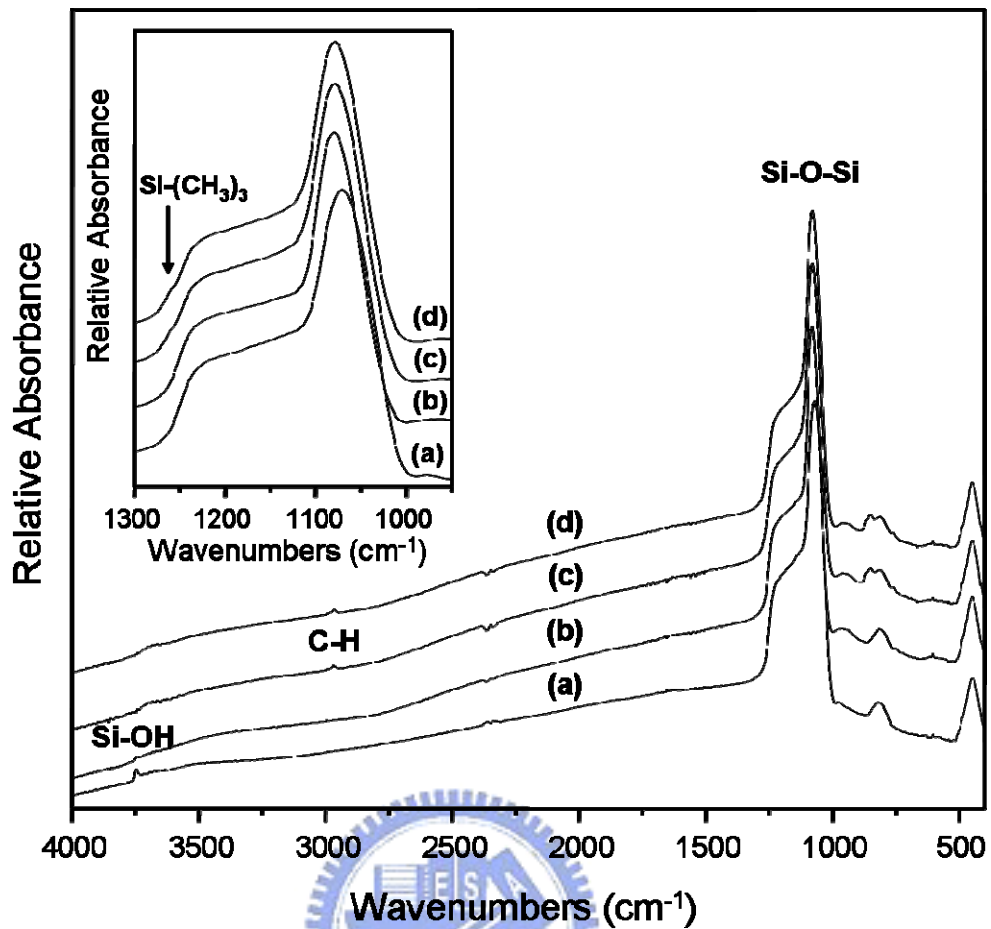


Figure 4.9 FTIR spectra of mesoporous silica thin film; (a) as-calcined film, (b) as-calcined film after H₂ plasma treatment for 3 min, (c) H₂ plasma treated film after HMDS treatment for 20 min, (d) H₂ plasma treated film after HMDS treatment for 30 min.

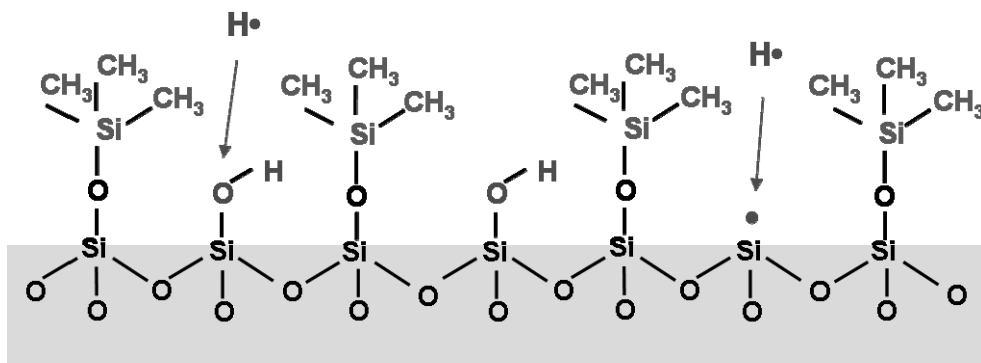


Figure 4.10 Schematic representation of trimethylsilylated mesoporous silica thin films subjected to hydrogen plasma treatment.

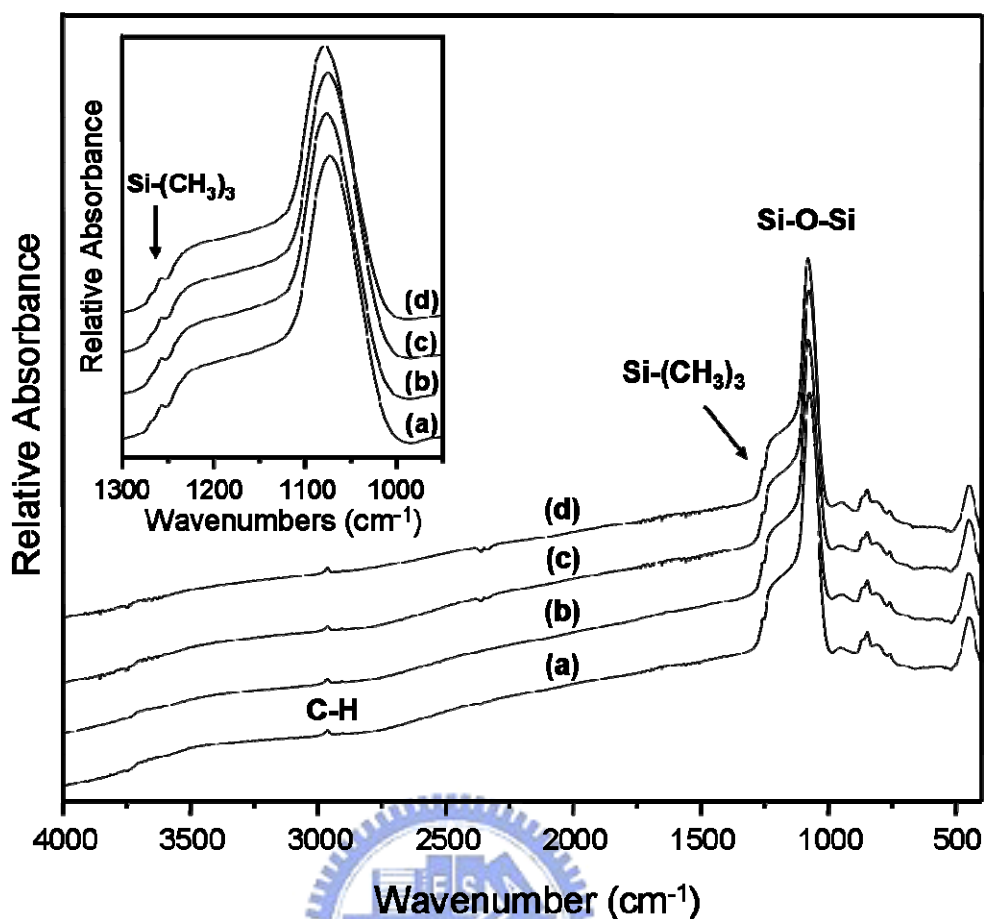


Figure 4.11 FTIR spectra of HMDS treated mesoporous silica thin film after H₂ plasma treatment for (a) 0 min, (b) 2 min, (c) 3 min, and (d) 10 min.

film. Accordingly, reductive hydrogen plasma modification promotes dielectric improvement and should be performed following HMDS hydrophobisation.

4.4 Summary

Spin-on mesoporous silica thin films were prepared by self-assembled templation. The density and the dielectric properties of the film were controlled by changing the surfactant/TEOS molar ratio of a silica precursor. The as-calcined mesoporous silica thin films have pore surfaces that are rich in surface silanol groups and easily adsorb water in the ambient atmosphere. Adding TMCS to the sol-gel precursor during gelation or exposing the

mesoporous thin film to HMDS vapor after calcination stabilizes the electrical properties and the hydrophobicity of the mesoporous silica film. HMDS-treated mesoporous silica thin films had an ultralow k value of 2.1. Combining HMDS vapor and low-power reductive H₂ plasma treatment further improved the dielectric properties of the mesoporous silica film. However, H₂ plasma treatment is suggested to be performed after HMDS vapor treatment to ensure the completeness of trimethylsilylation.



Chapter 5

Mechanical Strength of Surfactant-Templated Mesoporous Silica Thin Films

Silica dielectrics are typically prepared with high porosity to yield $k < 2.0$. Given a lack of complete chemical bonding support, more porous films have less mechanical strength, allowing breakage within the porous layer during chemical mechanical polishing. The controllable porosity and uniform pore size distribution are such that molecularly templated mesoporous silica films can provide better mechanical and dielectric properties than many other porous low- k dielectrics. However, the mechanical strength and dielectric stability of molecularly templated mesoporous films are still far inferior to those of conventional silicon oxide ILD and the former are liable to take up water. Before being implemented at sub-65 nm IC technology, mesoporous silica dielectrics must overcome the integration challenges. As stated in the preceding chapter, the hydrophobicity of a calcined silica film can be effectively improved by *in-situ* TMCS silylation in the sol precursor solution, and/or by HMDS vapor post-treatment. However, adding TMCS to the sol solution may disturb the self-assembly of template molecules and suppress the condensation reaction, resulting in the formation of mesoporous silica films with a less ordered pore structure and random micropores in the silica solid matrix. These changes mechanically weaken the TMCS-derivatized mesoporous films.

In this work, the relationship between the microstructure and the mechanical properties of the mesoporous silica films was studied by Fourier transform infrared spectroscopy, X-ray diffraction spectroscopy and nanoindentation test. Hardness and elastic modulus depend strongly on the methods of preparation and modification. They are effectively enhanced by

trimethylsilylation of HMDS.

5.1 Microstructure of Mesoporous Silica Thin Films

The thickness of the thin mesoporous silica films prepared as described above can be well controlled within the range of 250-450 nm, as measured by cross-sectional SEM. Figure 5.1 shows the cross-sectional SEM image of an as-calcined mesoporous silica thin film with no film modification. The SEM image clearly shows that the mesoporous silica thin film has a smooth surface and a uniform thickness. The average surface roughness was estimated to be less than 10 \AA ($5 \times 5 \mu\text{m}^2$) by AFM (Fig. 5.2). A smooth surface and a uniform thickness are essential to an accurate nanoindentation measurement for thin-film samples. According to the krypton adsorption/desorption isotherm, the total porosity of the as-calcined silica thin films ranges from 53% to 72% with an adjustable pore size from 43 to 80 \AA , depending on the

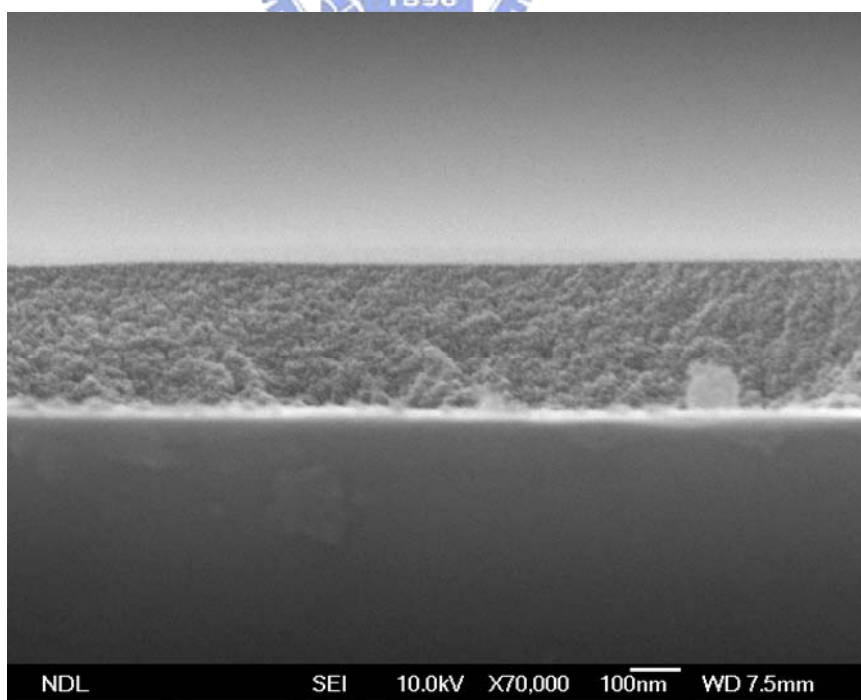


Figure 5.1 Cross-sectional SEM image of as-calcined mesoporous silica thin film. The thickness is estimated to be about 300 nm.

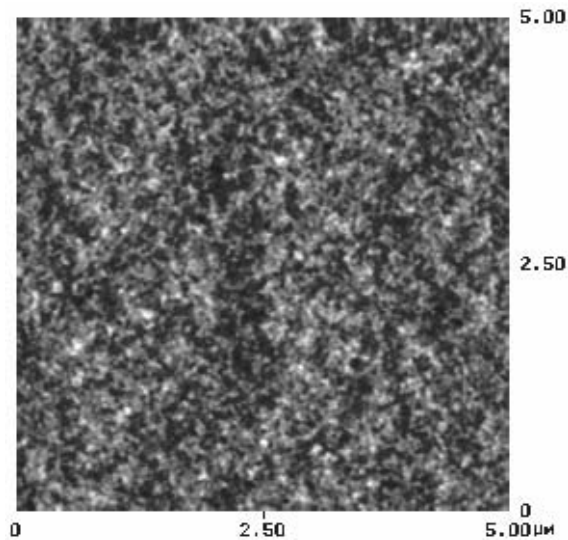


Figure 5.2 AFM image of the as-calcined mesoporous silica thin film. The image size is 5 x 5 μm^2 .

preparation of the precursor solution [16]. Self-assembled mesoporous silica thin films templated with P123 are known to have a hexagonal pore structure [104]. According to the XRD spectra shown in Fig. 5.3, the strong $\langle 100 \rangle$ diffraction signal reflects that the spin-coated mesoporous silica film without TMCS derivatization has an ordered pore-to-pore spacing of 61 Å after calcination. The single $\langle 100 \rangle$ peak without any other discernible diffraction signal reveals that the pore channel array is lying parallel to the silicon substrate surface. Compared with the sample set without TMCS modification, the TMCS derivatized mesoporous silica films have a weaker and broader $\langle 100 \rangle$ diffraction peak indicating a less ordered packing of the mesopores in the TMCS derivatized silica film. This suggests that the addition of TMCS in the sol solution significantly degrades the hexagonal pore structure of the mesoporous films. The $\langle 100 \rangle$ diffraction peak shifts to lower diffraction angles as the TMCS concentration in the sol precursor solution increases. When the TMCS molar ratio increases from 5 to 10%, the diffraction angle 2θ shifts from 1.42 to 1.29, corresponding to an increase in the pore-to-pore spacing from 64 to 70 Å. While the pore space increases with the TMCS concentration, there is no significant difference in the intensity and the full width at

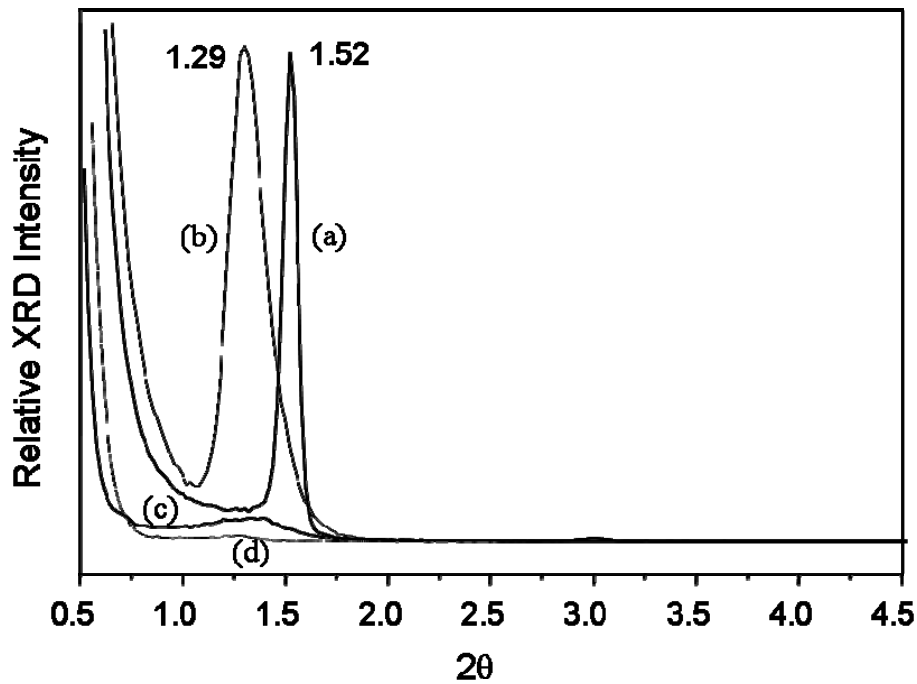


Figure 5.3 XRD spectra of the as-calcined mesoporous silica thin films; (a) without TMCS derivatization, (b) with 10% molar ratio TMCS, (c) with 15% TMCS, and (d) 25% TMCS. For clarity, the XRD spectrum of the mesoporous film with 5% TMCS is not shown. The (100) diffraction peak of the silica film with 5% TMCS is situated at $2\theta = 1.42$, and has an intensity and a fwhm comparable to the mesoporous film with 10% TMCS.

half-maximum (fwhm) of the $\langle 100 \rangle$ diffraction peaks between the 5 and 10% TMCS derivatized mesoporous films. The diffraction peak of mesoporous silica films with a TMCS molar ratio over 15%, has a 2θ angle close to that of the film with 10% TMCS, but becomes very broad and almost vanishes. The presence of TMCS in the sol precursor not only hampers condensation reactions but also perturbs self-assembly of the surfactant micelles, and thus leads to the formation of mesoporous silica thin films with a less ordered microstructure for the pore network and the silica matrix. It seems that, under the film preparation condition used in the study, there is a critical TMCS concentration in the sol precursor solution, above which the formation of an ordered self-assembled pore channel array is seriously retarded. Moreover, the surface roughness increases abruptly when the TMCS/TEOS molar ratio is higher than 0.15. Some islands of 1 μm round base and 5-9 nm thickness were found on the silica film

surface as shown in Fig. 5.4. These islands are composed of SiO₂ and the formation is closely related to the viscosity of precursor solutions [15].

FTIR was used to study the chemical structure of the mesoporous films. Figure 4.4 shows the FTIR spectra of the as-deposited, HMDS treated, and TMCS derivatized mesoporous silica thin films. As mentioned in Chap. 4, the as-calcined TMCS derivatized sample has a less extent of OH absorption ($\sim 3600\text{ cm}^{-1}$) as compared with the as-calcined

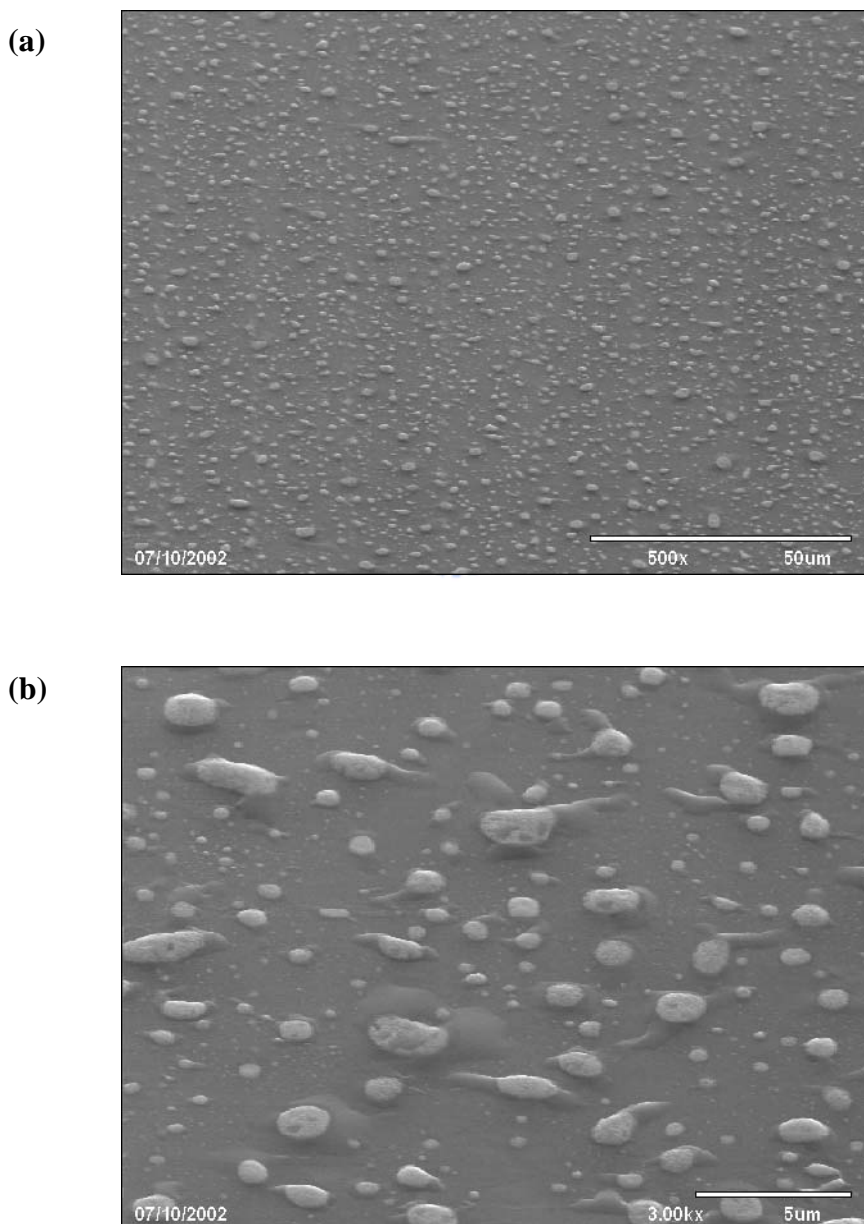


Figure 5.4 SEM images of the as-calcined mesoporous silica thin films with 15% molar ratio TMCS derivatization. The magnification is (a) 500x and (b) 3000x.

mesoporous film. After treatment with HMDS vapor, both mesoporous silica thin films with and without TMCS modification are effectively trimethylsilylated as indicated by the two strong absorption peaks at 1258 and 2965 cm^{-1} , which are due to Si-CH₃ and C-H₃ stretching vibration modes, respectively. The broad absorption band in the range of 1080-1280 cm^{-1} is due to asymmetric stretching of the intertetrahedral oxygen in the SiO₂ network, and is usually assigned to an overlap of two asymmetric stretching (AS) modes. The absorption band has been widely studied for various silica materials, and, generally, is assigned to be the overlap of two pairs of transverse optical (TO) and longitudinal optical (LO) modes [167-169]. Figure 5.5 shows that the absorption band of the as-calcined mesoporous silica film without TMCS modification can be well resolved into four peaks by curve fitting, assuming a Gaussian shape for the absorption peaks. The low wavenumber peak at $\sim 1069 \text{ cm}^{-1}$ is assigned to be a transverse optical mode (TO₃), and is due to the stretching motion of oxygen atoms moving back and forth with respect to the adjacent silicon atoms and in phase with neighboring oxygen atoms. Paired with the TO₃ absorption is the longitudinal optical mode (LO₃) centered at $\sim 1223 \text{ cm}^{-1}$. According to previous studies [167], another pair of TO-LO vibration modes (denoted by TO₄-LO₄ in the following text) is responsible for the overlapping absorption signal between the TO₃ and LO₃ peaks. The TO₄-LO₄ pair mode is due to the vibration in which oxygen atoms execute AS motion 180° out of phase with neighboring oxygen atoms. Figure 5.6 illustrates these two AS motion of the TO₃ and TO₄ modes. The TO₄ peak is estimated to center around 1177 cm^{-1} and the LO₄ is around 1125 cm^{-1} from Fig. 5.5. Compared with the as-calcined samples without TMCS modification, the TMCS derivatized mesoporous films have a higher absorbance for LO₄ and TO₄ vibration peaks as shown in Fig. 5.5.

Increasing TMCS concentration in the sol precursor results in a signal increase of the LO₄-TO₄ pair. Kirk has shown that disorder-induced mode coupling may result in

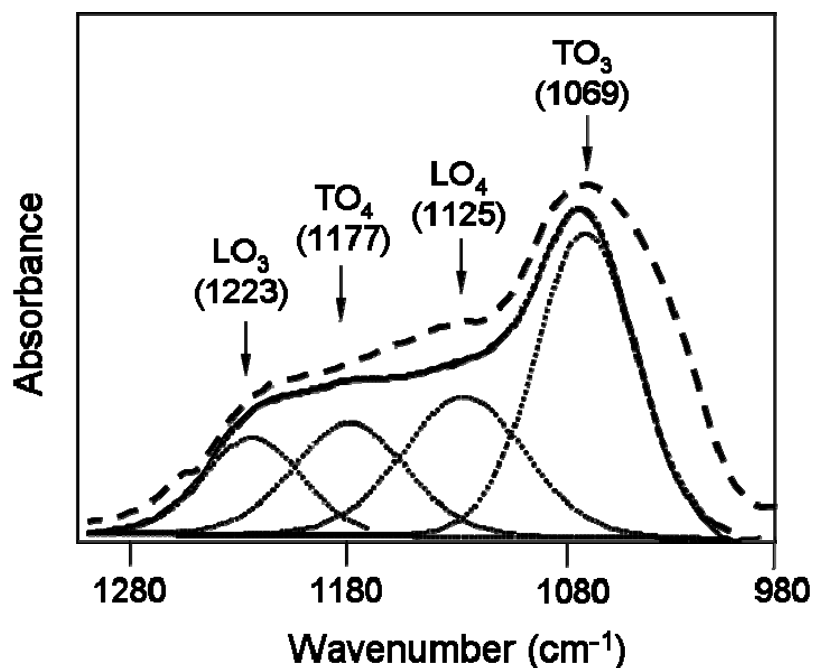


Figure 5.5 Curve fitting for the absorption band of the Si-O-Si asymmetric stretching modes of as-calcined mesoporous silica film without TMCS modification, assuming a Gaussian shape for the resolved peaks. For comparison, the absorption band of the TMCS (5%) derivatized film is also shown in the figure (dashed line). A broader and symmetric absorption feature at the low wavenumber side can be clearly seen for the TMCS derivatized film. The broader feature is ascribed to the presence of cyclosiloxane like rings as explained in the discussion.

enhancement of absorption of the TO₄ and LO₄ modes [168]. The absorption strength of the TO₄ mode of bulk silica was estimated to be three to five times that of the same mode in quartz, indicating that microstructure disorder may effectively enhance the absorption strength

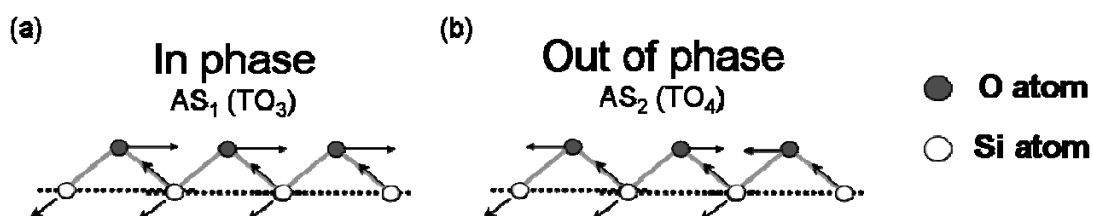


Figure 5.6 Asymmetric stretching motion of the (a) TO₃ and (b) TO₄ modes of the intertetrahedral oxygen in the SiO₂ network.

of the out-of-phase AS mode [169]. Therefore, the observation of a larger absorbance of the TO_4 - LO_4 pair for TMCS derivatized mesoporous silica films suggests that the addition of TMCS in the sol solution results in a less ordered microstructure in the silica matrix of the mesoporous network. In addition, the TO_3 peak becomes broader and shows less symmetric at the low wavenumber side for the TMCS derivatized samples. This may be ascribed to a poorly ordered microstructure and stress effects due to the presence of terminal methyl groups inside the silica matrix [170]. Besides the two pairs of TO-LO modes, one more peak at the low wavenumber side ($\sim 1030\text{ cm}^{-1}$) is needed to obtain a rational curve fit for the TMCS derivatized films. It is possible that random and small cyclic structures in the silica backbone, which are created due to incomplete condensation reactions and may be associated with cyclosiloxane like rings [171], are responsible for the broader and asymmetric absorption band. By analyzing the intensity variation of the absorption band of the Si-O-Si stretching modes, one can determine the relative orderliness of microstructure of the silica matrix in different mesoporous silica films. The FTIR spectra in the range of 975 - 1300 cm^{-1} for the mesoporous silica thin films with and without TMCS derivatization are shown in Fig. 5.7. Comparison of curves c and d in Fig. 5.7 shows that mesoporous film with 10% TMCS has a slightly higher TO_4 - LO_4 absorption signal than the film with 5% TMCS indicating a less ordered microstructure for the former. Also shown in Fig. 5.7 is the absorption band of the HMDS treated mesoporous silica film (curve b). Compared with the as-calcined film (curve a), curve b shows little difference in peak shape and position except an additional peak at 1258 cm^{-1} due to the Si- CH_3 stretching. This suggests that trimethylsilylation by the HMDS vapor treatment makes little change in the chemical structure of the silica matrix of the mesoporous films except the increase in the surface density of terminal methyl groups.

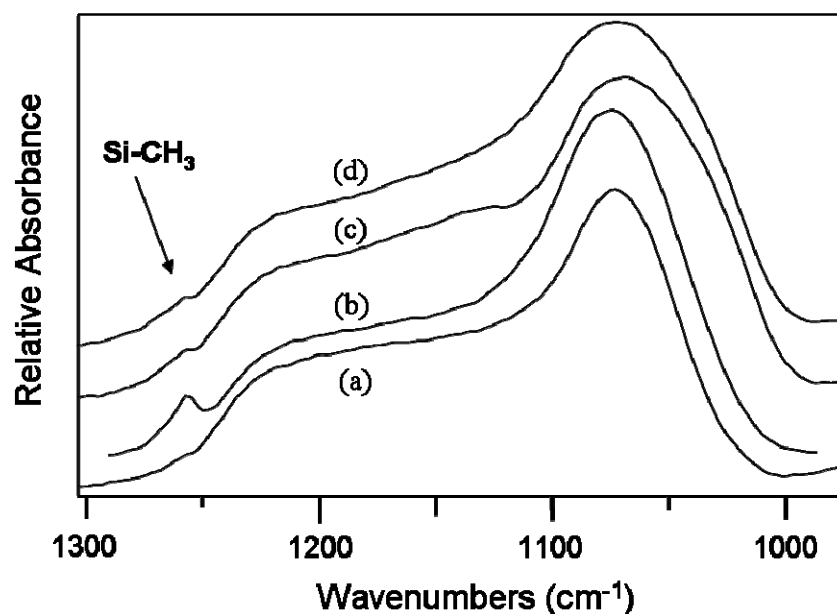


Figure 5.7 FTIR spectra of mesoporous silica thin films in the range of the Si-O-Si asymmetric stretching modes; (a) the as-calcined film, (b) the as-calcined film after the HMDS treatment for 30 min, (c) the as-calcined film with 5% TMCS, (d) the as-calcined film with 10% TMCS. The small peak at 1258 cm^{-1} is due to the Si-CH₃ stretching mode.

5.2 Effect of Methylsilylation on the Mechanical Properties

Elastic modulus is an important property characterizing the ability of porous materials to withstand stress-induced deformations. The elastic modulus and hardness of the mesoporous silica thin films are shown in Fig. 5.8. The TMCS derivatized mesoporous thin films have a much smaller elastic modulus and a slightly lower hardness than mesoporous films without TMCS modification. This is expected from a microstructural view point for the mesoporous thin films with an ordered pore structure. The introduction of TMCS in the precursor solution decreases the degree of the cross-linkage of the silica network and suppresses the amount of silanol groups on the silica species [15]. The less ordered hexagonal pore structure and a broad pore size distribution, as revealed by the XRD results, deteriorate the mechanical strength of the mesoporous films. In addition, micropores were also present in the silica matrix of the TMCS derivatized mesoporous films according to our previous study [16]. For

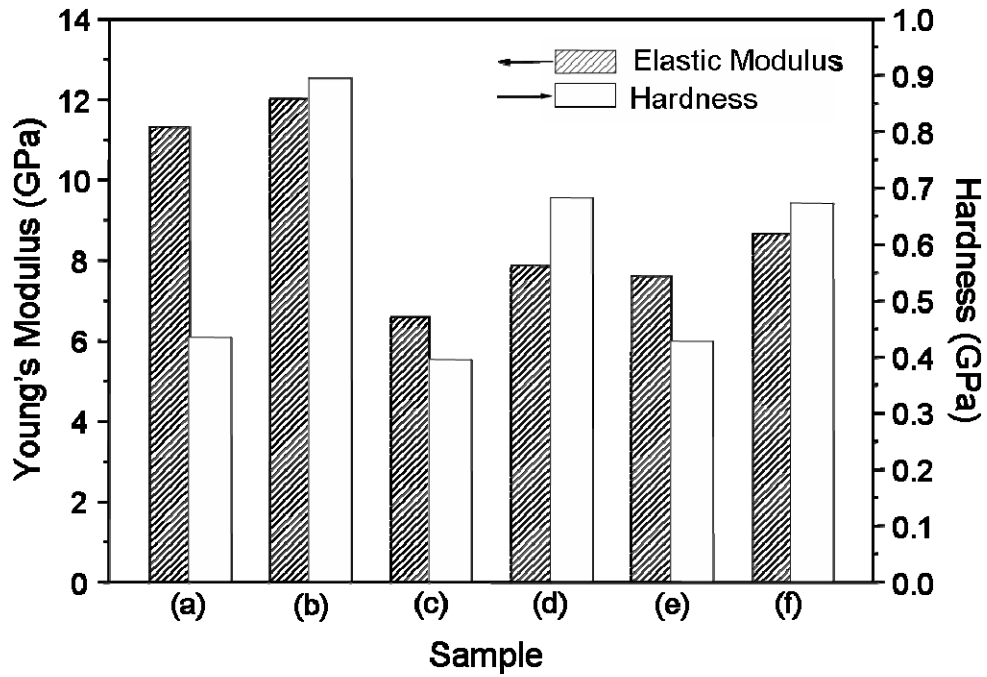


Figure 5.8 Young's modulus and hardness of the mesoporous silica thin films; (a) the as-calcined film, (b) the as-calcined film after the HMDS treatment for 30 min, (c) the as-calcined TMCS (5% molar ratio) derivatized film, (d) the TMCS (5% molar ratio) derivatized film after the HMDS treatment for 30 min, (e) the as-calcined TMCS (10% molar ratio) derivatized film, (f) the TMCS (10% molar ratio) derivatized film after the HMDS treatment for 30 min.

porous materials, while the k value decreases linearly with increasing porosity, the mechanical properties change as a power law with density or porosity [172]. The presence of micropores in the silica matrix not only supplies an additional porosity to the mesoporous film leading to a lower k value, but also decreases the density of the silica matrix. The molecularly templated mesoporous silica thin films prepared in this work can be considered as cellular material with a thick cell wall. For cellular materials, a reduction in the density of the cell wall certainly decreases the elastic modulus and other mechanical properties [173].

Nanoindentation measurements show that the mechanical strength of the mesoporous films can be greatly improved by trimethylsilylation. As shown in Fig. 5.8, the mesoporous silica films, both with and without the TMCS derivatization, gain an increase in hardness by a

factor of more than 75% after HMDS vapor treatment for 30 min. An increase of <20% in Young's modulus was observed. The improvement of mechanical strength can be attributed to the presence of trimethylsilyl groups on the pore surfaces. The mechanical strength of the 5% TMCS derivatized mesoporous film is somewhat weaker than that of the 10% TMCS derivatized film. As discussed previously, a higher TMCS content in the sol-gel precursor solution leads to the formation of a less ordered mesoporous silica network, resulting in weaker mechanical strength. The observation of the opposite trend is ascribed to that more terminal trimethylsilyl groups in the 10% TMCS derivatized film may enhance the mechanical strength due to a spring-back effect, and thereby compensate for the loss of the mechanical strength caused by the less ordered structure. Prakash *et al.* [174] and Smith *et al.* [172] have reported a "spring-back" feature for aerogel and xerogel films during the drying stage. The thickness of the xerogel film or the volume of the silica gel which receives methylation treatments can recover to a certain extent after the gel reaches its greatest compaction. On the contrary, shrinkage of the gel is completely irreversible for those nonmodified mesoporous silica thin films. The spring-back feature is attributed to the presence of terminal organosilane groups that cannot participate in condensation reactions. The electrostatic repulsion interaction between the crowded and bulky trimethylsilane groups on pore surfaces may effectively increase the resistance of the silica network to deformation under an applied load.

Table 5.1 lists some reported Young's modulus of low-*k* materials. Most silica based low-*k* materials have better modulus than polymer dielectrics. However, it shows a corresponding variety on the modulus and *k* values, and silica low-*k* material with high porosity often contains a modulus value below 10. The mesoporous silica thin film with methylsilylation in this work shows outstanding characters on both mechanical strength and dielectric constant by comparison, and, therefore, it has more integration advantages on the

Table 5.1 Elastic modulus for low-*k* materials.

Low- <i>k</i> material	Dielectric constant	Modulus (GPa)
Thermal oxide	3.9	72
PE-oxide	~4.1	59
Dense hybrid xerogel	3.7	44.8
Nanoglass	~1.9	2.5
HSQ	~3.2	4.74
59% porous HSQ	~2.2	2.5
56% mesoporous hybrid silsesquioxane	1.98	4.3
55% porous templated silica	2.4	~14
MSQ	2.9	1.65
PAE	~2.71	~3.9
40% porous PAE	~1.83	~2.04
SILK	2.65	~2.45
BCB	2.7	~2.9
Polynorbornene	2.67	~1.3
Polyimide (PI)	2.7	2.0
BPDA-PDA PI	3.1	~2.45
Teflon	~1.9	2.45

development of sub-65 nm IC technology nodes.

5.3 Summary

Microstructural and mechanical properties of organic surfactant templated mesoporous thin silica films have been studied by XRD, FTIR and nanoindentation. Compared with many other porous low-*k* dielectrics, the self-assembled molecularly templated mesoporous silica films demonstrate better mechanical properties. This is ascribed to the presence of a well-ordered pore channel structure in the mesoporous silica films. When the sol precursor solution is mixed with TMCS, the resulting mesoporous films have a weaker mechanical

strength. The pore channel structure of the mesoporous silica film becomes less ordered for the TMCS derivatized mesoporous films. In addition, FTIR analysis reveals that the chemical structure in the solid matrix of the porous network of the TMCS derivatized films is more disordered than those without TMCS modification. Trimethylsilylation by the HMDS vapor treatment can significantly improve the mechanical strength of the mesoporous silica thin films. The nanoindentation measurement results can be explained in terms of the pore microstructure of the mesoporous silica network and the spring-back effect due to the presence of trimethylsilyl groups in the nanopores.



Chapter 6

Effect of Trimethylsilylation on the Film Stress of Mesoporous Silica Ultralow- k Film Stacks

Mesoporous silica dielectrics have much poorer mechanical properties than their condensed counterparts and attention must be paid to their mechanical problems that arise upon integration into the Cu interconnect structure. One of the mechanical difficulties is the maintenance of satisfactory adhesion with adjacent layers and resistance against delamination or cracking during such processes as thermal and CMP. Amorphous hydrogenated silicon carbide (α -SiC:H) has many of the dielectric properties that are similar to those of silicon nitride used in the barrier/etch stop layer in the dual damascene structure, but it has a much lower dielectric constant ($k < 5$) than that of PECVD silicon nitride [60]. α -SiC:H thin films are typically deposited by PECVD, and the properties of the film, including the microstructure, the chemical stability and the thermal stability, strongly depend on various process variables [175-185]. Properly choosing deposition parameters such as, in particular, the deposition temperature is, therefore, critical to the application of α -SiC:H in Cu interconnect technology.

Mesoporous silica thin films prepared by the sol-gel method have a large tensile stress after drying because of film shrinkage, and plasma-assisted α -SiC:H films typically have a compressive stress, depending on the deposition temperature. When these two dielectric materials are placed together in the dual damascene structure, the concern regarding the compatibility between their mechanical characteristics demands close examination of the film stress that develops in a film stack that has ultralow- k mesoporous silica and barrier/etch stop

layers. The chapter discusses the effect of methylsilylation on the stress behavior of the mesoporous silica thin films and its film stack with an α -SiC:H upper layer. Trimethylsilylation relieved much of the tensile stress in the mesoporous silica thin film, and the compressive stress that developed in the α -SiC:H layer deposited by HDP-CVD could compensate for the intrinsic tensile stress of the mesoporous silica thin film, making the combination of these two dielectrics effective in the dual damascene process.

6.1 Volume Expansion by Spring-back Effect

The as-calcined mesoporous silica thin film has a very smooth film surface with a root-mean-squared roughness <1 nm according to atomic force microscopy (AFM) study. This facilitates the formation of a smooth and uniform interface when the HDP-CVD α -SiC:H thin film is deposited on the mesoporous silica thin film. Fig. 6.1 shows the cross-sectional SEM image of a film stack with the mesoporous silica/ α -SiC:H/mesoporous silica sandwich structure on the Si wafer. The sandwich structure was prepared to manifest the image contrast of the α -SiC:H layer and, in addition, simulate the dual-damascene structure, in which the α -SiC:H layer served as the etch stop. The thicknesses of the α -SiC:H and the mesoporous silica were about 50 nm and 250 nm, respectively. From the SEM image, the α -SiC:H layer was uniform in thickness without any observable microstructure flaw, suggesting that the uniform and unimpaired HDP-CVD α -SiC:H layer in the sandwich structure meets the preliminary requirement for the etch stop layer for the dual damascene process.

Trimethylsilylation has been widely used to improve hydrophobicity of porous low- k films [14-22]. Introduction of alkyl groups in the porous network can also enhance mechanical strength of the mesoporous silica thin film. The often adopted strategy to improve mechanical strength of porous low- k materials is to increase the extent of crosslinkage of the

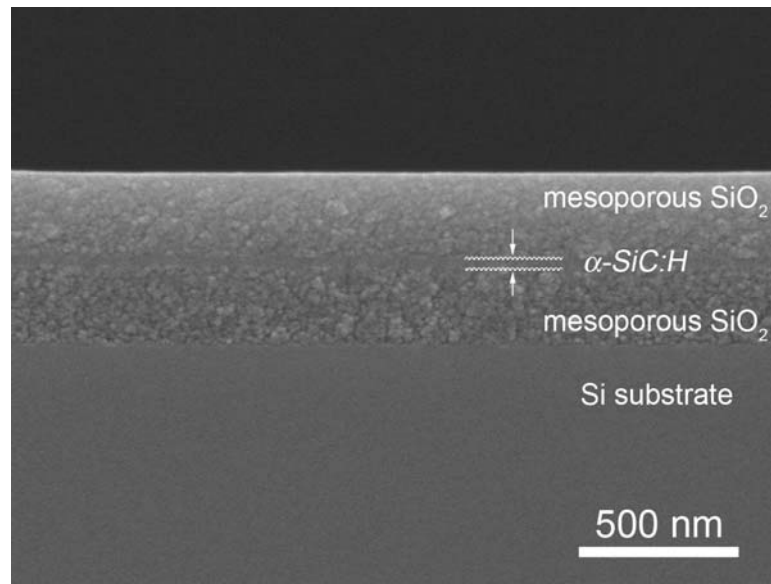


Figure 6.1 Cross-sectional SEM image of the mesoporous SiO₂/α-SiC:H/mesoporous SiO₂ sandwich film structure.

framework by thermal treatments [118]. However, this will increase the k value of the dielectric as a result of film densification during the thermal treatment, and moreover high temperature processes might also cause undesirable side effects to the dielectric. On the other hand, trimethylsilylation is carried out at relatively low temperatures, e.g., 165°C for the HMDS treatment, which is much lower than the calcination temperature of the mesoporous silica and, therefore, no further film contraction occurs. In contrast to high temperature processes, the HMDS treatment leads to a volume expansion of the trimethylsilylated thin film. As mentioned in Chap. 5, during the HMDS treatment, HMDS molecules can react with terminal Si-OH groups on the pore surface of the as-calcined mesoporous silica thin film, forming -O-Si-(CH₃)₃ surface groups on the pore surface. Bulky trimethylsilyl groups thus introduced into the mesoporous silica will lead to volume expansion of the porous silica thin film. Volume rebound has been reported for methylsilylated wet gels during the drying process, and the observation was designated as “spring-back effect” [174]. Figure 6.2 shows the variation of the film thickness of the HMDS treated mesoporous silica thin film after each

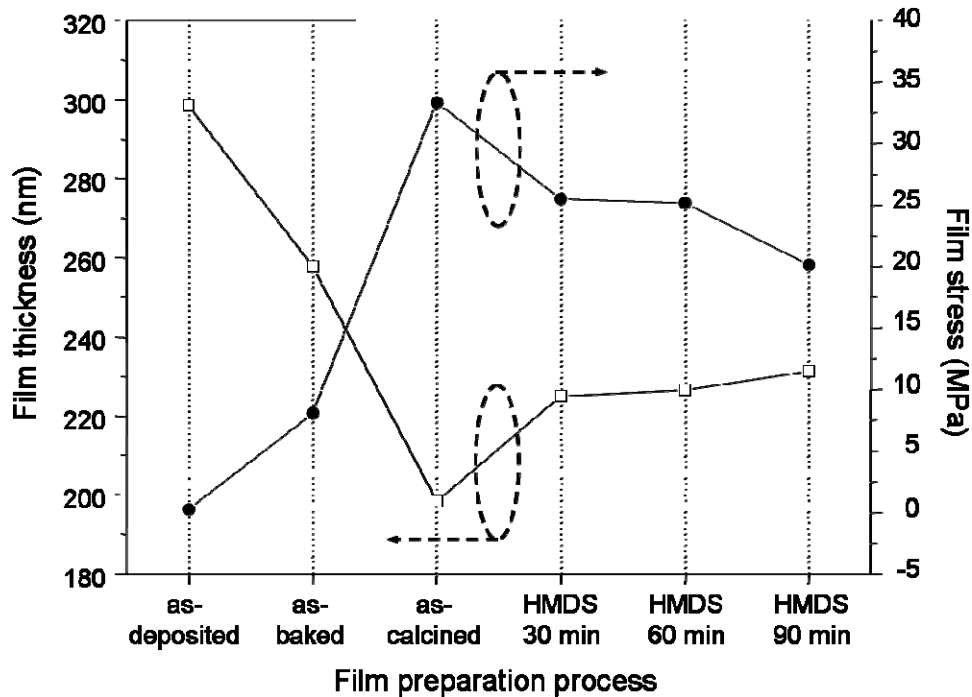


Figure 6.2 Film thickness of the mesoporous SiO₂ thin film after various steps of the film preparation process. The film thickness was examined by cross-sectional SEM. Also shown in the figure is the film stress of the mesoporous film.

film preparation step. The thickness was estimated by cross-sectional SEM. The film thickness slightly increased with the HMDS treatment time, and the mesoporous silica film exposed to HMDS vapor for 60 min shows a 15% increase in the film thickness as compared to the as-calcined thin film. Figure 6.3 shows the FTIR absorption band around 1258 cm⁻¹, which is due to the stretching vibration of Si-CH₃ groups on the pore surface, as a function of the HMDS treatment time. The intensity of the absorption band increased with the HMDS exposure time. Since the bond density is proportionate to the integrated absorbance, the FTIR analysis indicates that trimethylsilylation is more effective when the mesoporous film is subjected to a longer HMDS exposure, implying that the volume expansion of the porous silica thin film is a result of the introduction of the trimethylsilyl surface groups. Accompanied with the volume expansion of the HMDS treated mesoporous silica thin film is the enhancement of the mechanical strength. The electrostatic interaction among bulky

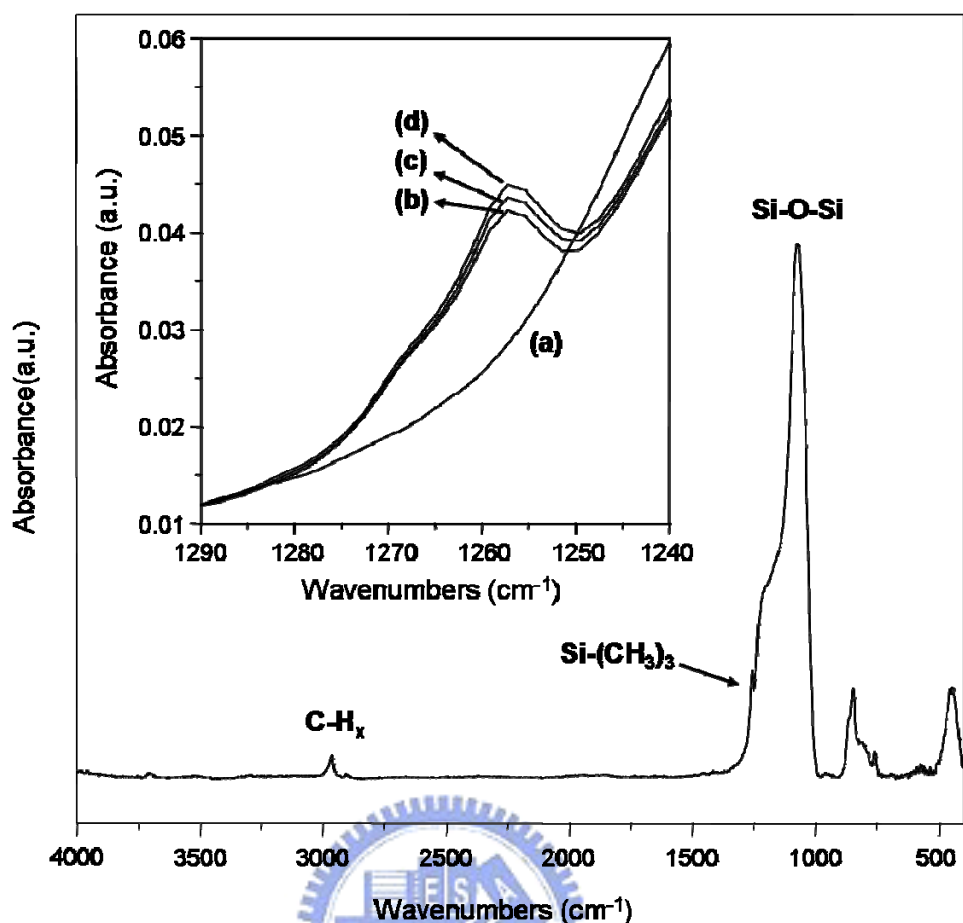


Figure 6.3 FTIR spectrum of the mesoporous silica thin film after the HMDS treatment for 30 minutes. The inset shows the absorption band around 1258 cm^{-1} , which is due to the $\text{Si}-(\text{CH}_3)_3$ stretch vibration, for (a) the as-calcined film, and for the mesoporous silica after the HMDS treatment for (b) 30 min, (c) 60 min, (d) 90 min.

trimethylsilyl groups on the pore surface causes significant expansion in the film volume, and the surface groups may behave like a cushion providing the silica network effective resistance against deformation under an applied load. Fig. 6.4 shows the dependence of elastic modulus and hardness of the trimethylsilylated mesoporous silica on the exposure time of the HMDS treatment. The mesoporous silica thin films with the HMDS treatment had a higher Young's modulus and hardness than that without the treatment. The Young's modulus increased from 11.3 GPa to 13.5 GPa, and the hardness increased from 0.4 GPa to 1.2 GPa with increasing the HMDS treatment time. Similar mechanical strength enhancement for HMDS treated

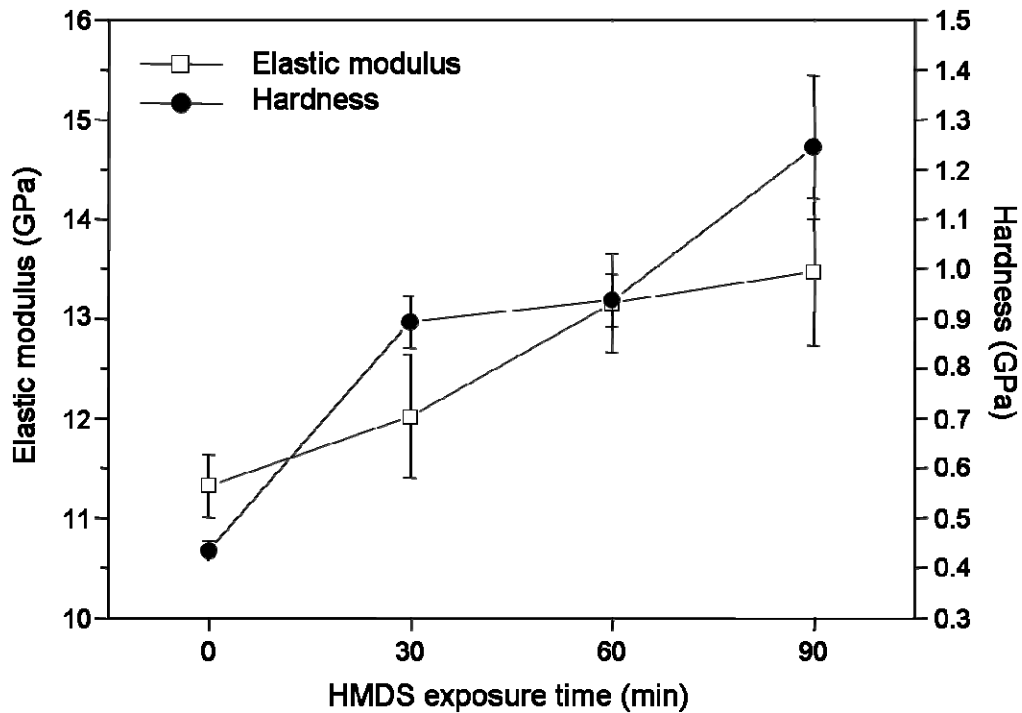


Figure 6.4 Elastic modulus and hardness of the mesoporous silica thin films as a function of the HMDS exposure time.

mesoporous silica films has been mentioned previously. The marked improvement in mechanical strength of the HMDS treated mesoporous silica thin film can be ascribed to the spring-back effect.

6.2 Film Stress Relaxation

The spring-back effect can also ease the tensile stress, which builds up in the mesoporous silica thin film during the baking and calcination processes. Also shown in Fig. 6.2, in addition to the film thickness, is the film stress of the mesoporous silica thin film measured after each step of the film preparation process. After the spin-coating deposition, a negligible tensile stress (0.27 MPa) developed in the mesoporous silica thin film. The tensile stress dramatically increased after the bake and calcination processes, and the increase of tensile stress is in accordance with the trend of decrease in the film thickness as shown in Fig. 6.2.

This agrees to the understanding that the film shrinkage, resulting from solvent evaporation and organic surfactant removal from the mesoporous silica thin film, leads to the development of the tensile stress [16]. The film stress becomes more tensile as more P123 surfactant is added in the precursor, as indicated in Fig. 6.5. On the other hand, the decrease in the magnitude of the tensile stress with increasing the HMDS treatment time is in compliance with the trend of increase in the film thickness (Fig. 6.2), revealing that the film expansion as a result of trimethylsilylation by the HMDS treatment can relieve the tensile stress in the mesoporous silica film.

The ease of the tensile stress was also observed for the mesoporous silica thin film coated by an HDP-CVD α -SiC:H thin layer. When the α -SiC:H film was deposited on the as-calcined mesoporous SiO₂ thin film, the tensile stress originally developed in the mesoporous layer exhibited a dramatic reduction, and the reduction, which was inversely related to the deposition temperature of the α -SiC:H thin film, was so large that the stress of the film stack even became compressive. As shown in Fig. 6.6, deposition of the α -SiC:H

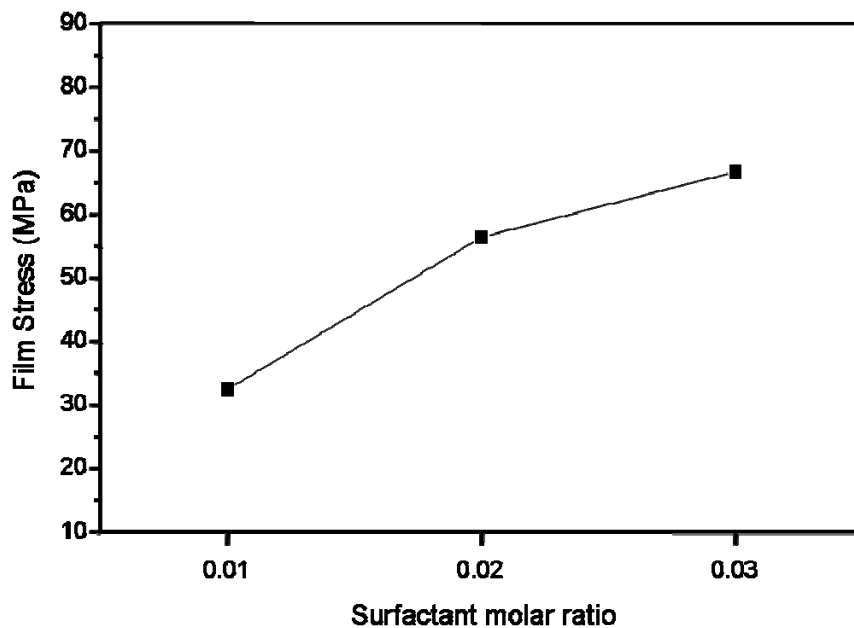


Figure 6.5 Film stress of the mesoporous SiO₂ as a function of surfactant/TEOS molar ratio.

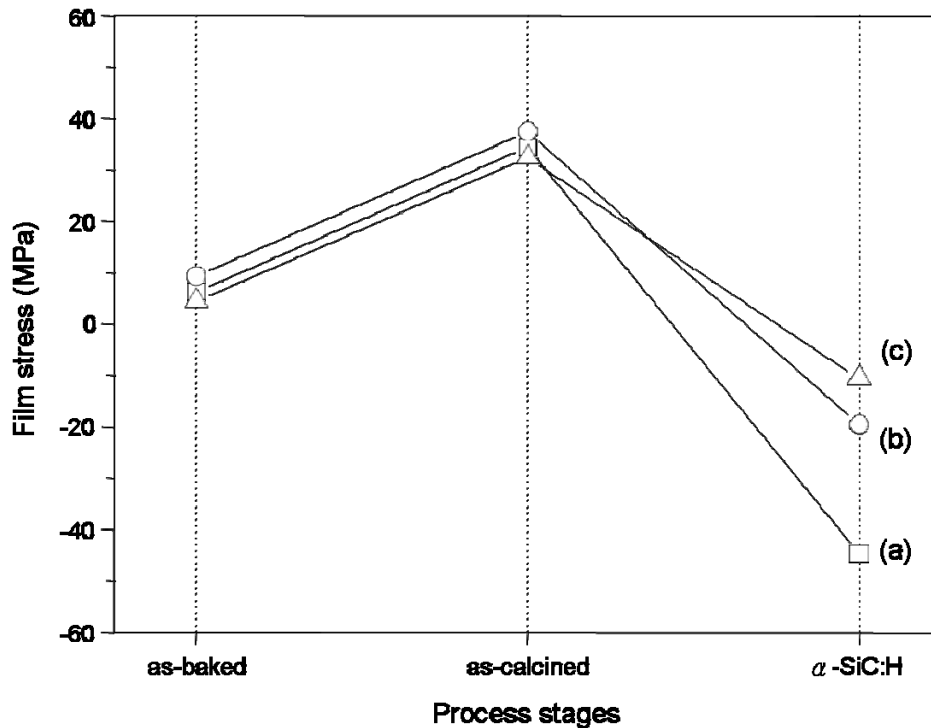


Figure 6.6 Film stresses of three mesoporous $\text{SiO}_2/\alpha\text{-SiC:H}$ film stacks at different preparation stages. The $\alpha\text{-SiC:H}$ capping layer was deposited at (a) 150°C , (b) 250°C , and (c) 350°C .

layer at 150°C caused the largest drop in the film stress, and that at 350°C resulted in the least. Silicon carbide films deposited on silicon substrates by PECVD without anneal are generally under a large compressive stress, which can be larger than -500 MPa [175-178]. Development of compressive stress also occurred to the HDP-CVD $\alpha\text{-SiC:H}$ thin film deposited on the silicon wafer as shown in Fig. 6.7. The stress in the $\alpha\text{-SiC:H}$ film became more compressive as the deposition temperature decreased. It has been reported that HDP-CVD $\alpha\text{-SiC:H}$ thin films deposited at higher temperatures had a higher film density [186, 187]. Also shown in Fig. 6.7 is the refractive index of the HDP-CVD $\alpha\text{-SiC:H}$ layer. The refractive index increased with increasing the deposition temperature, indicating that the $\alpha\text{-SiC:H}$ layer deposited at a lower temperature had a smaller mass density. During the $\alpha\text{-SiC:H}$ film growth, Si-C crosslinking was less effective at lower temperatures, leading to the formation of a

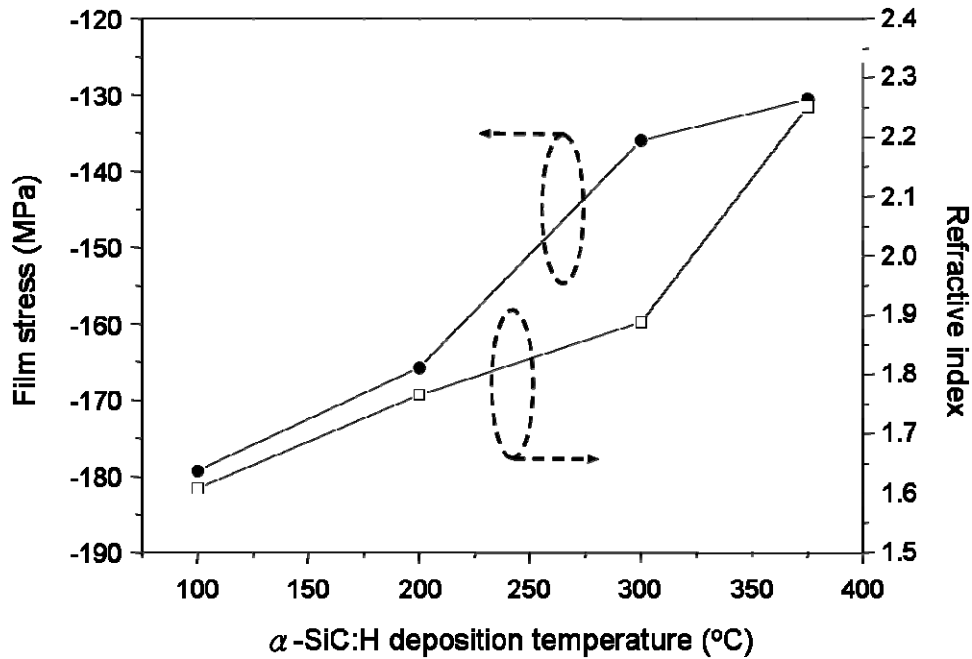


Figure 6.7 Film stress and refractive index of the α -SiC:H film deposited on the Si wafer as a function of deposition temperature.

carbide film full of microvoids, and thus with a smaller mass density [186]. As a result, a larger compressive stress developed in the low-temperature α -SiC:H film. When the α -SiC:H thin film was deposited on the mesoporous silica thin film, the intrinsic compressive stress of the carbide film could compensate for the tensile stress developed in the mesoporous silica layer, and even made the film stack compressive as a whole. The dependence of the film stress on the α -SiC:H deposition temperature shown in Fig. 6.6 can be ascribed to that the low-temperature α -SiC:H layer was more compressively stressed, and, therefore, could compensate for the tensile stress in the mesoporous silica layer more effectively. The compensation effect can reduce wafer bending of the mesoporous silica coated wafer, and thus might be important for the lithography process in nano-scaled IC technology nodes.

In addition to the stress compensation effect described above, there is possibly one more factor which can alleviate the tensile stress in the mesoporous silica thin film capped with the HDP-CVD α -SiC:H layer. According to our previous study, the porous structure of the

α -SiC:H thin film grown at low temperatures could trap gaseous process species and also provided gaseous species diffusion channels into the underlying mesoporous silica layer [186]. X-ray photoelectron spectra (XPS) and thermal desorption mass spectroscopy (TDS) analyses revealed that these residual gaseous species could react with the pore surface of the mesoporous silica layer forming alkoxy terminal surface groups with a chemical form of Si-O-C_nH_{2n+1}. The higher was the deposition temperature of the carbide layer, the less was the amount of the carbonaceous species found in the mesoporous silica layer according to Auger analysis (Fig. 6.8). The alkoxy terminal groups, similar to trimethylsilyl groups in the HMDS treated mesoporous silica, may produce the spring-back effect, and hence relief the tensile stress of the underlying mesoporous silica thin film. However, the alkoxy groups, mainly ethoxyl groups [186], have a smaller chemical structure, therefore the induced spring-back effect should not be as obvious as that by trimethylsilyl groups, and thus we believe that their

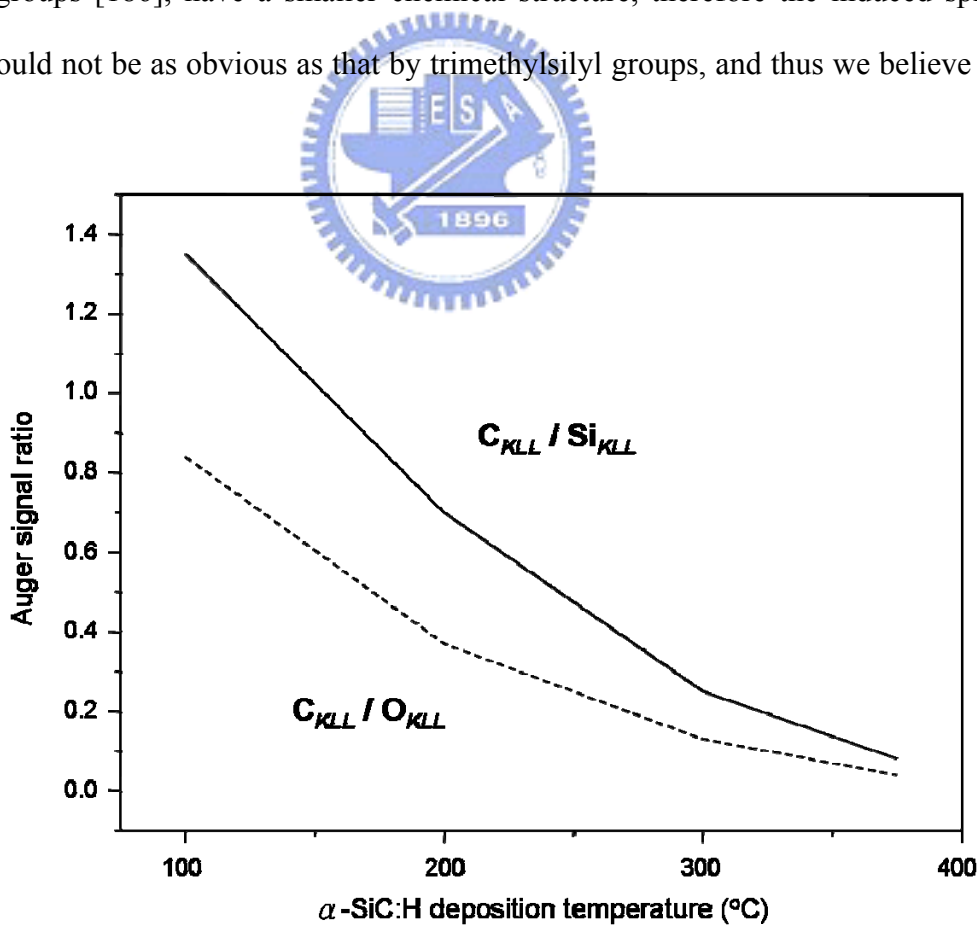


Figure 6.8 Auger intensity ratios of carbon to oxygen and to silicon for mesoporous silica/ α -SiC:H film stacks as a function of α -SiC:H deposition temperature.

contribution to the stress relief should be much smaller.

6.3 Thermomechanical Characteristics

Like the mechanical strength, the coefficient of thermal expansion (CTE) of the mesoporous silica film is important, since most of the stresses that arise in the interconnect are thermally induced, resulting from CTE mismatches between various materials in the interconnect structure. For instance, many organic dielectrics have $\text{CTE} > 50 \text{ ppm}/^\circ\text{C}$, and so the high-temperature process causes the development of high tensile stresses in the film. The film's CTE can be estimated from the stress-temperature curves of different substrates. Figure 6.9a plots the temperature-dependent stress of the mesoporous SiO_2 films during thermal cycling. The difference in stress between the heating and cooling curves may be caused by the presence of a large number of pores in the silica film, which does not change with further cycling. Reversible closed loop and an absence of stress hysteresis (the difference between the film stress at the start and the end of a complete thermal cycle) were evident in the second and third cycles, indicating that the composition or the structure of the film is stable. During cooling, the stress-temperature curve is almost linear, which fact can be accounted for thermal expansion. A slight transition is evident at approximately 200°C in the cooling curve. The reason is currently unclear, but it may involve the uptake of moisture by the film, since the temperature is very close to that of the desorption of hydrogen-bonded water (Fig. 4.6). Figure 6.9b plots the stress-temperature curve of the mesoporous SiO_2 film treated with HMDS. The HMDS-treated mesoporous film cools more linearly, supporting that the slope transition in the stress-temperature curve of the mesoporous SiO_2 film may cause by the physisorbed water. According to Eq. 3.4, the CTEs of the as-calcined mesoporous SiO_2 films are determined to be $1.21 \text{ ppm}/^\circ\text{C}$ in the range $50\text{-}200^\circ\text{C}$ and $2.20 \text{ ppm}/^\circ\text{C}$ in the range $200\text{-}450^\circ\text{C}$. HMDS treatment reduces the film's CTE to $1.09 \text{ ppm}/^\circ\text{C}$. Table 6.1 summarizes the CTEs of common

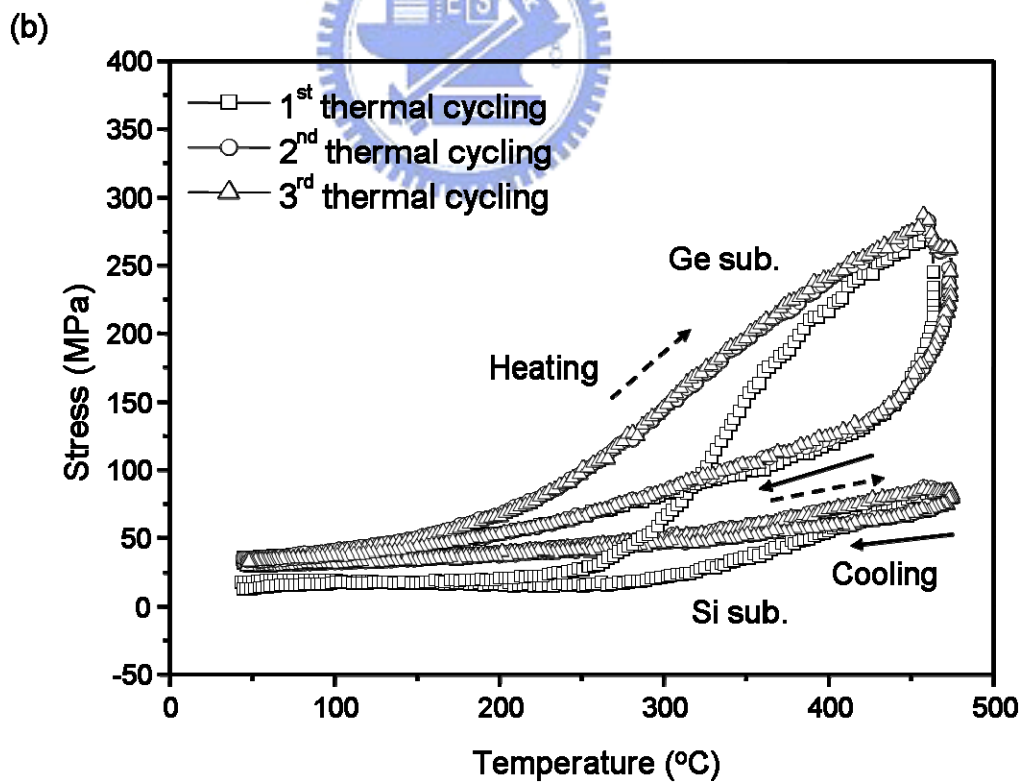
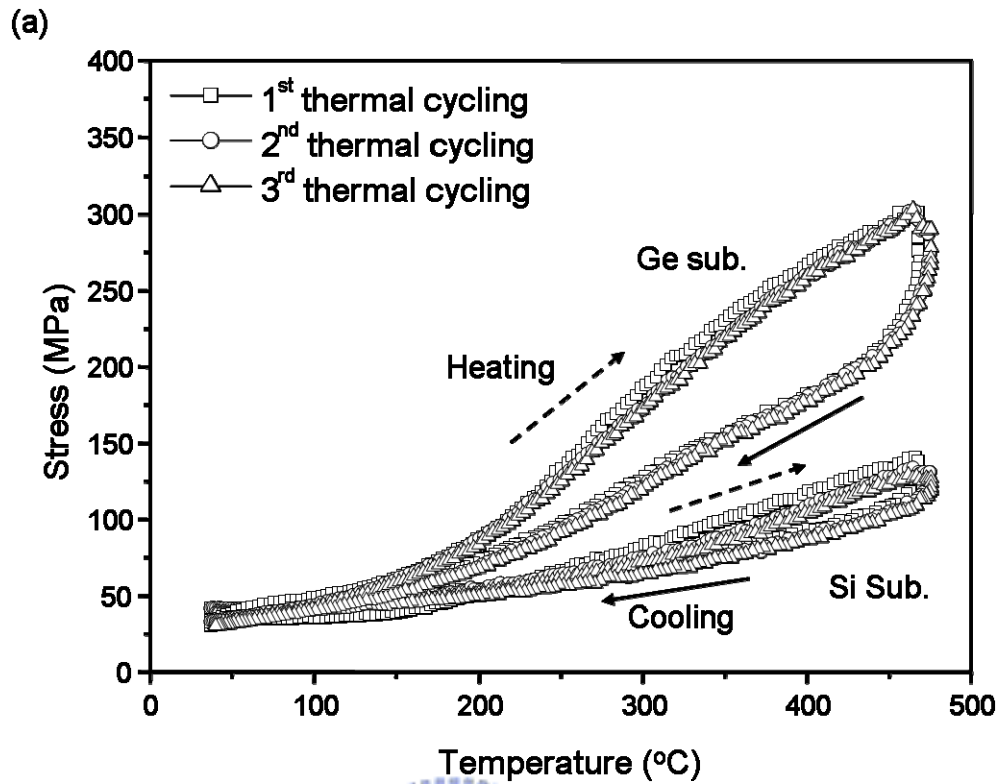


Figure 6.9 Stress as a function temperature during thermal cycling for mesoporous silica film on Si and Ge substrates; (a) the as-calcined film and (b) the methylsilylated film.

semiconductor and low-*k* materials [188-190]. The CTEs of the mesoporous SiO₂ films were very close to the reported values of TEOS oxide (1-2.67 ppm/°C) and Si (2.61 ppm/°C) and far lower than those of other low-*k* materials, such as HSQ (20-25 ppm/°C in 25-225°C), or SiLK (62 ppm/°C in 50-150°C). Additionally, the expansion of the HMDS-treated mesoporous SiO₂ film is less than that of the as-calcined film perhaps because stress is relieved by the spring-back effect in the trimethylsilylated film, reducing the degree of thermal mismatch with the substrate. It therefore has thermomechanical stability.

Table 6.1 Coefficients of thermal expansion for various interconnect materials.

Material	CTE 25-225°C (ppm/°C)
Si	2.61
Ge	5.84
Cu	17.7
Al	23.1
TaN	6
SiO ₂	0.5
TEOS oxide	1.0-2.67
PTFE	135
BPDA-PDA	3.8
Crosslinked PAE	52
Fluorinated PAE	52
BCB	62
SiLK	62
Parylene-N	55-100
Parylene-F	33
HSQ	20-25

6.4 Summary

In summary, the film stresses of mesoporous SiO₂ thin films and α -SiC:H/mesoporous SiO₂ film stacks were studied. Mesoporous silica thin films exhibit a tensile stress due to film shrinkage after the bake and calcination processes. As the mesoporous silica thin film receives the HMDS treatment, the tensile stress is greatly relieved, and the extent of the stress relaxation increases with the HMDS treatment time. This is ascribed to the so-called spring-back effect, which results from the formation of bulky trimethylsilyl surface groups in the nanopores. In addition to the film stress, the spring-back effect can also effectively improve elastic modulus and hardness of mesoporous silica thin films. When the HDP-CVD α -SiC:H thin film was deposited on the tensile-stressed mesoporous silica thin film, the measured film stress was found to be largely reduced, and the film stack even became compressively stressed. The alleviation of the tensile stress was dependent on the carbide microstructure, which varied with the deposition temperature. The α -SiC:H thin films deposited at lower temperatures had a smaller film density and showed a higher compressive film stress, which might counterbalance the tensile stress developed in the underlying mesoporous silica layer. Alkoxylation occurring in the mesoporous silica layer during α -SiC:H deposition at low temperatures is also suggested to provide spring-back effect to compensate for the tensile stress in the mesoporous silica layer. The coefficient of thermal expansion deduced from the thermal cycling stress shows that the CTE of the as-calcined mesoporous SiO₂ films are 1.21 ppm/°C in 50-200 °C and 2.20 ppm/°C in 200-450 °C. A smaller expansion value of 1.09 ppm/°C can be obtained after HMDS treatment indicating that trimethylsilylation can also improve the thermomechanical stability of the film.

Chapter 7

Thermal Stability of Trimethylsilylated Mesoporous Silica Thin Film as an Ultra-low k Dielectric in Copper Interconnects

The as-calcined mesoporous silica thin film is inherently hydrophilic because residual silanol terminal groups are present on the pore surface. The uptake of moisture by these silanol groups can greatly degrade the dielectric properties of the mesoporous silica thin film. The as-calcined mesoporous silica thin film was trimethylsilylated before Cu-metallization by exposing it to HMDS vapor at 165°C, to increase the hydrophobicity of the mesoporous dielectric layer. The chemical stability of the trimethylsilyl groups introduced into the porous dielectric layer strongly affects the thermal and mechanical stabilities of the Cu-metallized film stack, during subsequent high-temperature annealing treatments. The terminal trimethylsilyl groups may not be able to retain their integrity following postmetallization thermal cycles. Therefore, an understanding of the thermal properties of the surface terminal groups is very important to the implementation of mesoporous silica dielectrics in advanced copper interconnect technology. In this chapter, the thermal and dielectric stability of the HMDS-treated mesoporous silica thin film is studied, and its effect on the Cu-metallized mesoporous silica film stack is discussed.

7.1 Trimethylsilylation of the Mesoporous Silica Thin Film

Figure 7.1 shows thermal desorption spectra of CH₄ for the as-calcined and the

HMDS-treated mesoporous silica thin films. CH_4 ($m/e = 16$, solid line) molecules, which can be ascribed to be an associative desorption product of methyl groups, began to desorb from the mesoporous silica thin film at $\sim 375^\circ\text{C}$, but significant desorption did not occur until the sample temperature exceeded 400°C , and the desorption reached its maximum around 580°C . This suggests that trimethylsilyl surface groups in the HMDS-treated mesoporous film are thermally stable up to 400°C .

The FTIR study also indicated that notable decomposition of the trimethylsilyl surface groups took place at temperatures larger than 450°C . Figure 7.2(a) shows FTIR spectra of the as-calcined, the HMDS-treated, and the annealed mesoporous silica thin films. Figures 7.2(b) and 7.2(c) are the enlarged absorption spectrum windows for the C-H stretching and Si-O-Si stretching modes, respectively. The as-calcined mesoporous silica films [Fig. 7.2(a)(i)] are rich in residual OH groups ($\sim 3600\text{ cm}^{-1}$), and thus are liable to adsorb a large amount of water molecules ($\sim 3300\text{ cm}^{-1}$). As shown in Fig. 7.2(a)(ii), an absorption peak developed at

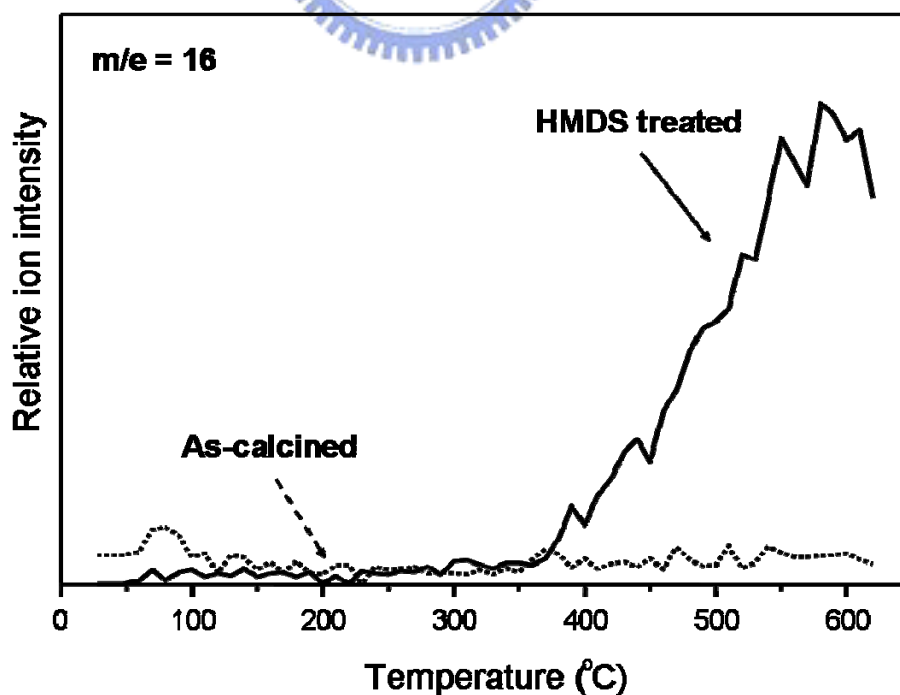


Figure 7.1 Thermal desorption spectra of CH_4 ($m/e = 16$) for the as-calcined (dash line) and the HMDS treated (solid line) mesoporous silica thin films.

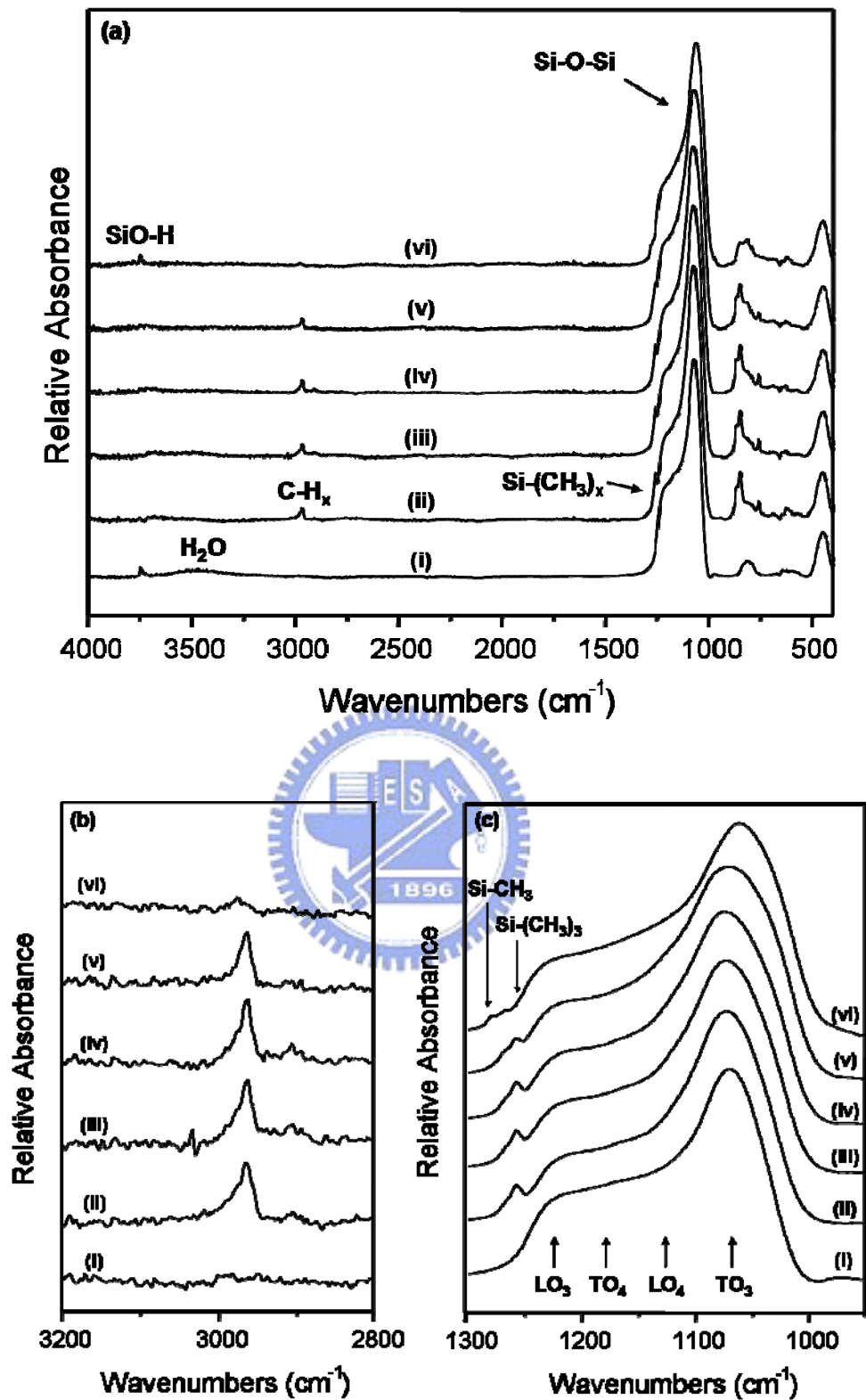


Figure 7.2 (a) FTIR spectra of (i) the as-calcined film, (ii) the HMDS treated film, and the HMDS treated film annealed at (iii) 300°C, (iv) 400°C, (v) 500°C, and (vi) 600°C. The enlarged absorption spectrum windows for the C-H stretching and the Si-O-Si asymmetric stretching modes are shown in (b) and (c), respectively.

1258 cm^{-1} , which is attributed to Si-CH₃ stretching vibration in the trimethylsilyl groups, and the methyl group-related C-H stretching peaks appeared around 2965 cm^{-1} after the HMDS vapor treatment, indicating that the mesoporous silica thin film was effectively methylsilylated. In addition, the disappearance of the OH absorption peak and the broad water absorption band in the FTIR spectrum suggests that the mesoporous dielectric became hydrophobic after the HMDS treatment. When the HMDS-treated mesoporous silica film was thermally annealed, the intensities of the CH_x and the Si-CH₃ absorption peaks did not show discernable decrease until the annealing temperature was higher than 400°C as revealed by Figs. 7.2(a)(iii) and 7.2(a)(v). The methylsilyl related absorption peaks shown in Figs. 7.2(b)(v) and 7.2(c)(v), which are for samples annealed at 500°C, exhibit a slight intensity decrease, as compared with Figs. 7.2(b)(ii) and 7.2(c)(ii), implying that decomposition of trimethylsilyl terminal groups on the pore surface did take place at 500°C, but the decomposition was rather moderate. On the other hand, the mesoporous silica annealed at 600°C lost most of the intensity of the two CH₃ absorption peaks, and the Si-CH₃ peak had obvious changes in the peak's shape and position. According to Fig. 7.2(c)(vi), the peak at 1258 cm^{-1} for the sample annealed at 600°C became vague, and two new absorption peaks emerged at 1268 cm^{-1} and 1278 cm^{-1} , which can be attributed to the Si-CH₃ stretching mode as well. It has been reported that a change in the number of the CH₃ moiety on the terminal Si-(CH₃)₃ group of the trimethylsilylated silica will cause slight shifts in the peak position of the Si-CH₃ stretching mode [191, 192]. The absorption peak centered at ~1278 cm^{-1} is attributed to the Si-CH₃ stretching of the monomethylsilyl group, and the absorption peak of the dimethylsilyl group is situated between the monomethylsilyl and trimethylsilyl peaks, around 1268 cm^{-1} . The obvious blueshift of the Si-CH₃ stretching absorption peak suggests that severe decomposition of terminal Si-(CH₃)₃ groups on the pore surface of the mesoporous silica thin film occurs at 600°C. In addition, the significant intensity loss and dramatic change

in the peak shape of the asymmetric $\text{CH}_3\text{-Si}$ rocking mode, which is situated in the $700\text{--}900\text{ cm}^{-1}$ range [158], also indicates the decomposition of terminal $\text{Si-(CH}_3)_3$ groups at the high annealing temperature. In addition to the intensity variation of the absorption peaks associated with the Si-CH_3 group, the asymmetric Si-O-Si stretching absorption band situated between 1000 and 1300 cm^{-1} also reveals that the chemical structure of the silica matrix became less ordered as the annealing temperature increased. The asymmetric Si-O-Si stretching absorption band is, in general, assigned to be the overlap of two pairs of transverse optical (TO) and longitudinal optical (LO) modes [167-169]. One of the two pairs, denoted as $\text{TO}_3\text{-LO}_3$, is due to the asymmetric stretching motion of oxygen atoms moving in phase with neighboring oxygen atoms, and has the associated TO and LO peaks situated at $\sim 1069\text{ cm}^{-1}$ and $\sim 1223\text{ cm}^{-1}$, respectively. The other pair, denoted as $\text{TO}_4\text{-LO}_4$, is due to the Si-O-Si vibration in which oxygen atoms execute stretching motion 180° out of phase with neighboring oxygen atoms, and has the TO_4 peak situated around 1177 cm^{-1} and the LO_4 peak around 1125 cm^{-1} . Previous studies suggested that the TO_4 and LO_4 modes in the SiO_2 matrix with a less ordered chemical structure have a greater absorption [168, 169]. By analyzing the intensity variation of the absorption band of the Si-O-Si stretching modes, one can evaluate the microstructure ordering of the silica skeleton in the mesoporous silica thin film (as referred to Chap. 5). From Fig. 7.2(c), the Si-O-Si stretching absorption band of the HMDS-treated mesoporous silica has an almost identical peak position and shape as the as-calcined one, except the additional peak at 1258 cm^{-1} due to the $\text{Si-(CH}_3)_3$ stretching. This implied that trimethylsilylation by the HMDS treatment introduces little change in the chemical structure of the silica matrix of the mesoporous films. On the other hand, as shown in Figs. 7.2(c)(v) and 7.2(c)(vi), the LO_4 peak of the mesoporous film is apparently enhanced after the anneal at 500°C , and a substantial change in the absorption shape of the Si-O-Si absorption band of the sample annealed at 600°C . Combining previous discussion on the absorption peaks associated with the $\text{Si-(CH}_3)_3$

surface group, the chemical structure of the mesoporous silica thin film becomes less ordered upon the anneal at temperatures $>450^{\circ}\text{C}$ due to the decomposition of terminal trimethylsilyl groups. The extensive decomposition of the trimethylsilyl surface group at 600°C will have a destructive impact on the mechanical strength of the mesoporous silica thin films.

Table 7.1 lists the dielectric constant and the leakage current density of the HMDS-treated mesoporous silica film after annealed at 400°C . For mesoporous silica films without the HMDS treatment, a rational capacitance-voltage ($C-V$) curve could not be obtained because the leakage current was enormously large. On the other hand, the mesoporous silica thin film receiving the HMDS treatment and 400°C anneal has a dielectric constant as low as 2.14 and a leakage current density smaller than $3.1 \times 10^{-8} \text{ A/cm}^2$ at 2 MV/cm. The significant decrease in the k value is ascribed to extensive elimination of water molecules physisorbed in the mesoporous silica film after the trimethylsilylation treatment. The trimethylsilylated mesoporous silica film is electrically reliable as shown by the dielectric property of the sample which was stored in cleanroom ambient for over 50 days. The trimethylsilylated mesoporous silica film shows little change in the dielectric constant and the leakage current density after the 50 shelf days, suggesting that bulky trimethylsilyl groups can effectively block further moisture uptake and, thus, the mesoporous silica thin film retains its hydrophobicity.

Table 7.1 Dielectric properties of the as-calcined and HMDS treated mesoporous silica thin films after 400°C anneal.

Film	Process conditions	k_{eff}	$J \text{ (A/cm}^2\text{) at 2 MV/cm}$
A	As-calcined	>20	1.5×10^{-3}
B	HMDS treated	2.14	3.1×10^{-8}
C	Storage for 50 days	2.16	3.6×10^{-8}

7.2 Thermal and Chemical Stability of the Cu/Ta(N)-metallized Mesoporous Silica Film Stack

When integrated into copper damascene process, the mesoporous silica dielectric faces many process challenges, such as solvent and gas penetrations via nanopores during cleaning, etch, and CVD processes. In particular, copper is a fast diffusing species in silicon dioxide and poorly adheres to most dielectric materials. This may become more severe when copper is bound to porous materials because a porous structure provides an effective path for surface diffusion and smaller contact area at the interface. Although a thin Ta or nitrided Ta [Ta(N)] barrier layer is always deposited between the Cu layer and the IMD layer to avoid Cu penetration, Cu can still diffuse into the IMD layer if any mechanical failure occurs to the barrier layer. Moreover, since trimethylsilylated mesoporous silica becomes chemically unstable at temperatures $>500^{\circ}\text{C}$ as discussed before, the deposited Cu/Ta(N) layers may suffer film crack or interfacial failure as they are annealed at temperatures $>500^{\circ}\text{C}$. Therefore, thermal stability of the Cu/Ta(N) metallized mesoporous silica thin film is particularly critical to the success of the integration of mesoporous silica dielectric into the Cu damascene structure. In order to study the impact of thermal instability of the trimethylsilylated mesoporous silica layer to the integrity of the Cu interconnect structure, a film stack with an SiN_x (30 nm)/Cu (100 nm)/Ta(N) (30 nm)/mesoporous silica (200 nm)/Si layer structure was prepared and annealed at various temperatures. The nitride capping layer was deposited on the Cu layer to prevent copper from oxidation during anneals. Figure 7.3 shows Auger depth profiles for the film stack after thermal anneals at 450°C and 600°C . The AES depth profiles show that carbon distributes evenly in the mesoporous silica layer, implying that trimethylsilylation by HMDS treatment is uniform through the mesoporous silica layer. From the AES depth profiles, Ta(N) seems to be able to effectively prevent Cu from penetrating into

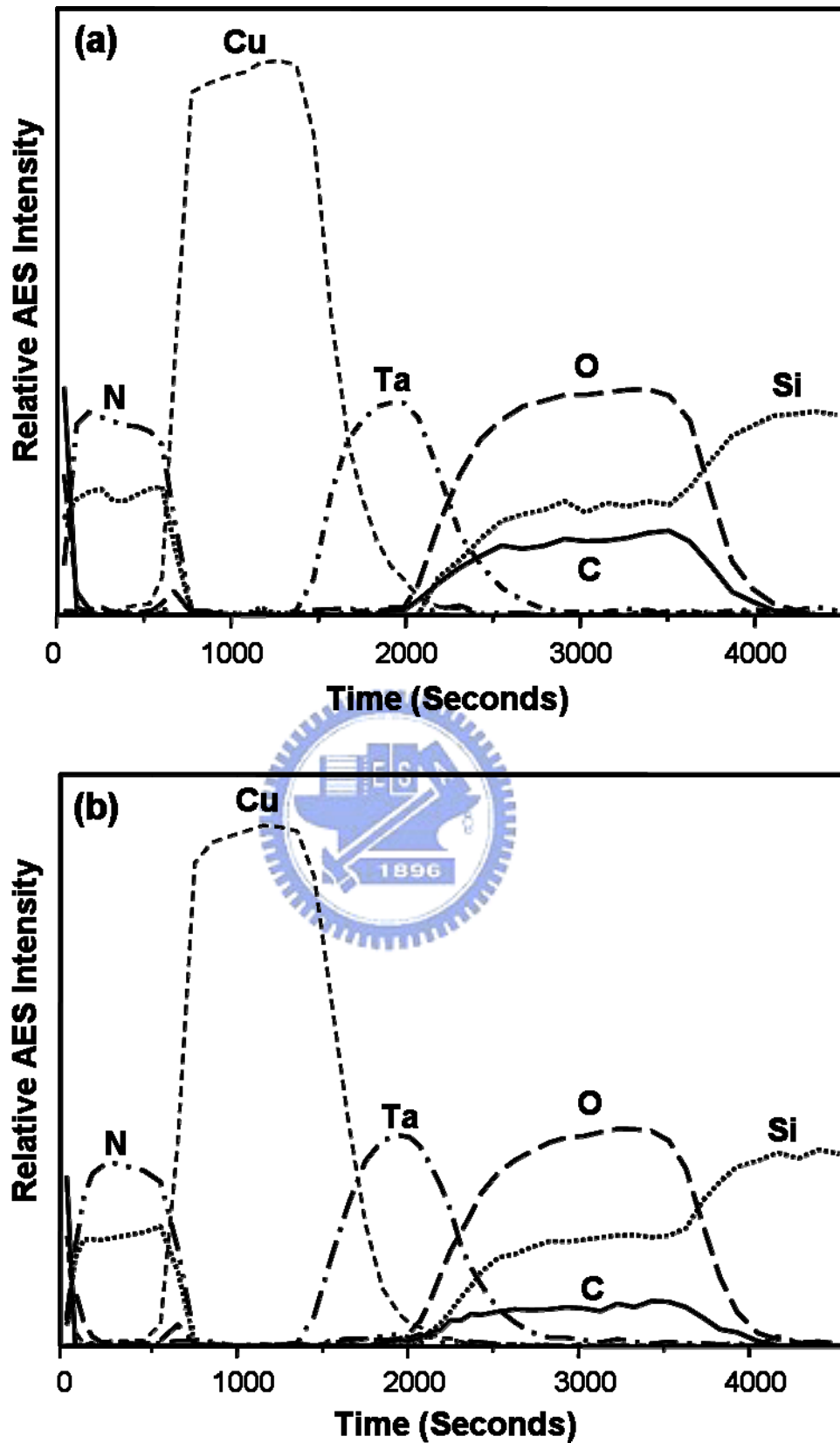


Figure 7.3 AES depth profiles of the Si_N_x/Cu/Ta(N)/mesoporous SiO₂/Si film stack after (a) 450°C annealed and (b) 600°C annealed.

the mesoporous silica layer. The tail of the Cu profile smoothly decaying into the mesoporous silica region is not due to copper diffusion, but is likely due to the ion mixing effect inevitably occurring during depth profiling. This will become clear when we discuss the BTS results later, which reveal no mobile ion drift in the mesoporous film. Compared with the sample annealed at 450°C, the AES depth profile of film stack annealed at 600°C shows a significant decrease in the carbon signal in the mesoporous silica layer. The heavy loss of the carbon content suggests that the decomposition of trimethylsilyl groups bounded on the pore surface is very severe at 600°C.

Although TDS results indicate that the decomposition of trimethylsilyl groups on the pore surface becomes significant at temperatures >450°C, the AES depth profiles shown in Fig. 7.3 seem not to reveal any discernible interfacial failure. Moreover, delamination at the interfaces in the metallized mesoporous silica film stack was not observed in scanning electron micrographs (not shown) even for the sample annealed at 600°C, in which the mesoporous silica has suffered serious decomposition of trimethylsilyl groups on the pore surface. Figures 7.4(a) and (b) show the cross-sectional TEM micrographs of the metallized mesoporous film stack annealed at 450 and 600°C, respectively. The TEM images clearly show that the interfaces between the neighboring layers in both samples are smooth and without separation. Since the decomposition of trimethylsilyl groups is severe at 600°C as revealed by the FTIR, Auger depth profile, and TDS analysis, the undamaged interfaces may lead to an intuitive suggestion that the gaseous decomposition products either are small in quantity compared with the pore volume in the mesoporous silica layer, or can easily diffuse out of the film stack through open pore channels in the porous layer. According to high-resolution TEM (HRTEM) study to be discussed, we found that decomposed alkyl species reacted with the Ta(N) barrier layer during the high-temperature anneal forming stable tantalum carbide at the interface between the barrier layer and the mesoporous silica layer.

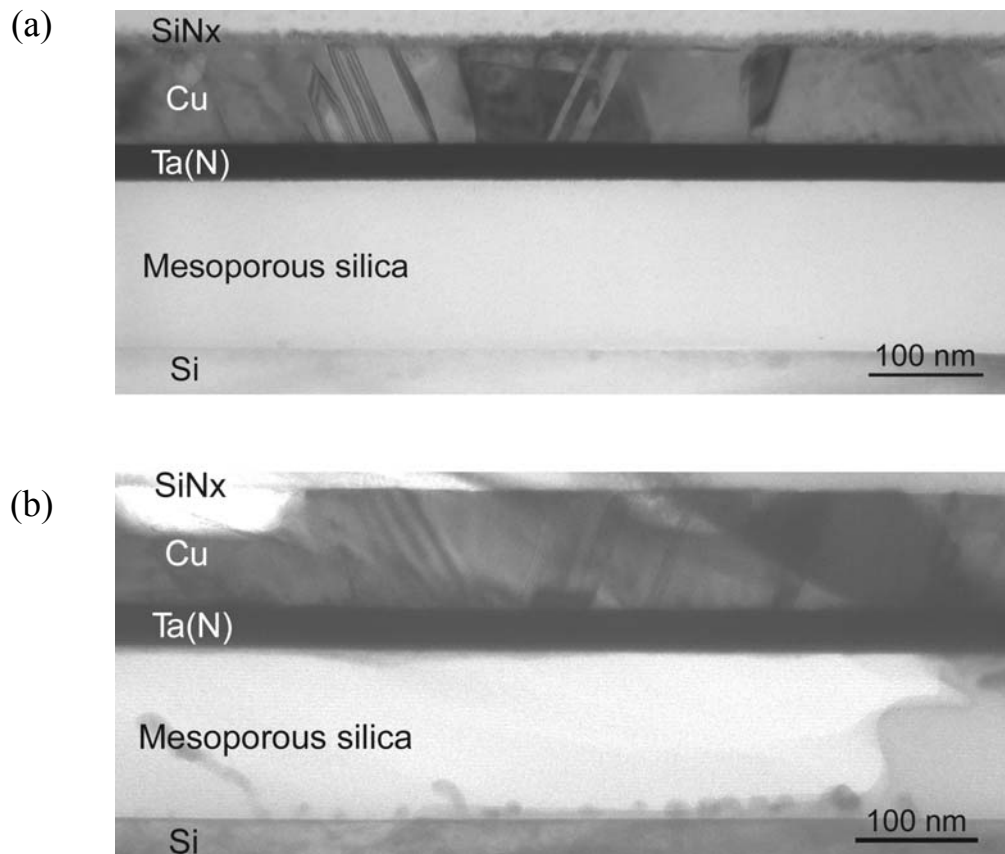


Figure 7.4 Cross-sectional TEM images of the metallized film stack after (a) 450°C annealed and (b) 600°C annealed.

Figure 7.5 is an HRTEM image for the film stack annealed at 600°C, and the image reveals the presence of a nanocrystal $\sim 20 \times 20 \text{ nm}^2$ in size at the interface between the Ta(N) and the mesoporous silica layers. The nanosized phase was only found at sparse locations along the interface. The microstructure of this nanophase was analyzed in terms of fast Fourier transformation images. The lattice spacing of the nanocrystal viewed along the [111] zone axis was estimated to be 2.36 Å in the $(10\bar{1})$ and $(0\bar{1}1)$ planes and 2.68 Å in the $(\bar{1}\bar{1}0)$ plane. The angles between the $(\bar{1}\bar{1}0)$ and $(0\bar{1}1)$ planes and between the $(\bar{1}\bar{1}0)$ and $(10\bar{1})$ planes were found to be 57.4° and 61.3° , respectively. The lattice parameters agree very well with the corresponding values for hexagonal Ta_2C structure ($p\bar{3}m1$) [193]. Combining the

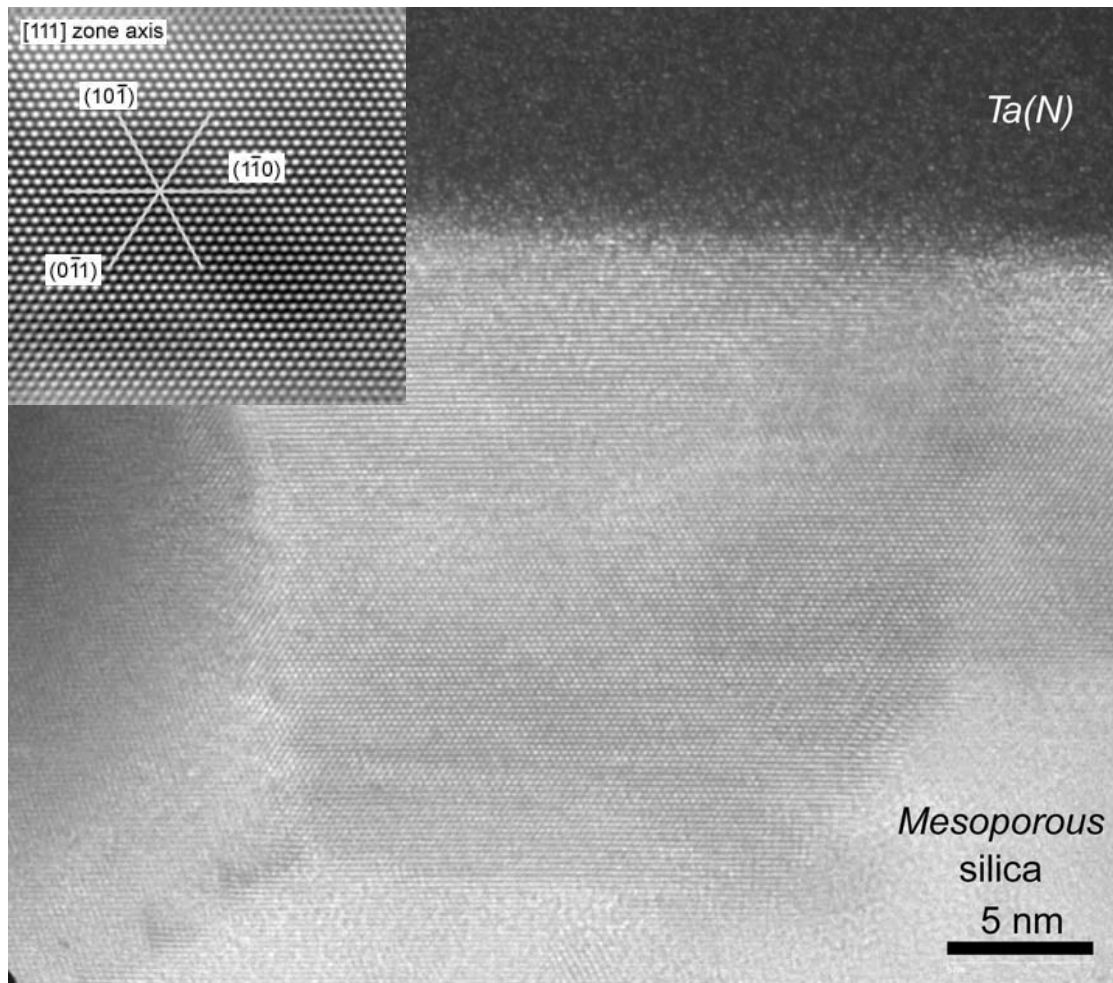


Figure 7.5 High resolution TEM micrograph of the Ta₂C nanocrystal at the Ta(N)/mesoporous silica interface of the sample annealed at 600°C for 30 minutes.

observations of the uniform decrease in the carbon content through the mesoporous silica layer and the undamaged interfaces strongly suggests that the Ta₂C nanocrystal was formed as a result of the reaction between the decomposed trimethylsilyl group and the Ta(N) barrier layer. It has been reported that gaseous species can diffuse through pore channels of nanoporous silica [186, 194, 195]. As gaseous decomposed alkyl species suddenly evolve from the pore surface and diffuse through the porous silica layer to the interface, they can quickly react with Ta forming the stable carbide nanocrystal, thereby alleviating the tendency to mechanically damage the film stack during high-temperature anneals. Because of many desirable properties, such as excellent thermal stability, high melting temperature (~3980°C),

high hardness (≥ 20 GPa), and chemical inertness, tantalum carbide has been proposed to be a potential diffusion barrier for Cu interconnect technology [196]. Although the presence of Ta_2C is a result of the decomposition of trimethylsilyl groups, it does not cause apparent mechanical and electrical degradation in the metallized mesoporous silica film stack. Moreover, formation of the nanocrystal occurs at temperatures far above the typical process temperature of copper interconnect, and will not cause any integration difficulty for the trimethylsilylated mesoporous silica. The loss of the trimethylsilyl surface groups during annealing may change the effective dielectric constant of the film stack, we believe, however, the change is insignificant since these surface groups occupied only a small fraction of the pore volume.

Because AES has a relatively high detection limit, the Auger depth profiles shown in Fig. 7.3 cannot provide conclusive proof that Cu penetration into the mesoporous silica layer was completely retarded. In order to study if Cu ions diffused into the mesoporous silica layer after a typical interconnect annealing process at 400°C , BTS measurement was carried out. The Cu-metallized mesoporous silica film stacks with and without the anneal treatment were biased at 20 V at 150°C for 15 min so that Cu ions, if any, diffusing into the porous dielectric during the film stack process could be drifted to the dielectric/Si substrate or dielectric/gate electrode interfaces, depending on the bias polarity. The accumulated Cu ions would create uncompensated positive space charges at the interface. The positive space charges will result in a negative flat-band voltage shift in the $C-V$ curve at a positive gate bias and the magnitude of the voltage shift depends on the amount of charges. Because of the high porosity, the mesoporous silica dielectric has a much smaller cross-sectional area available for Cu diffusion than dense oxides, and the enormously large pore surface and the tortuous silica skeleton might lead to a complex Cu diffusion path under the vertical bias field in the film stack. This might lead to a smaller Cu diffusion rate in the porous dielectric than in dense oxide under the

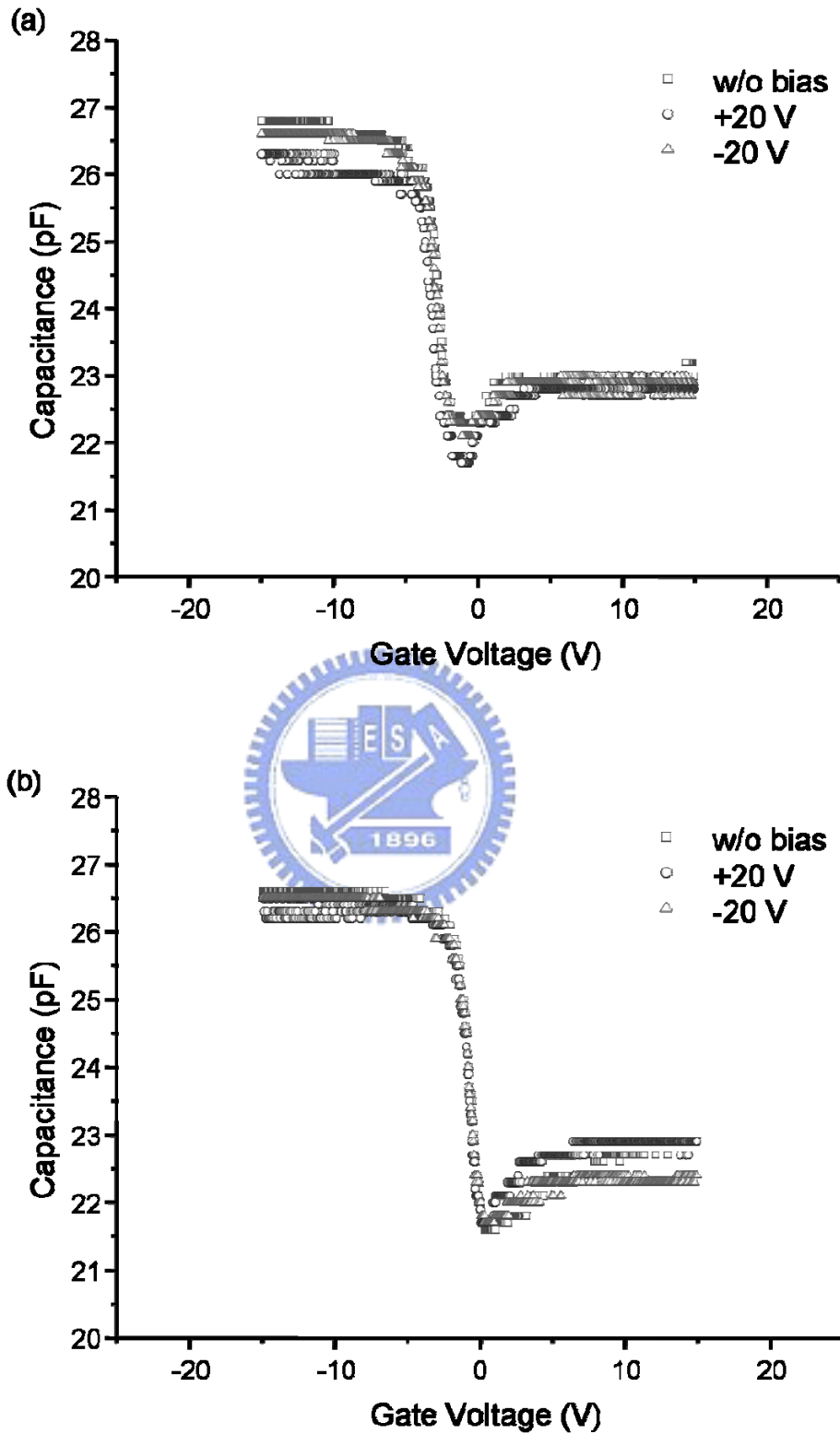


Figure 7.6 C-V traces of Cu-MIS capacitors stressed under various gate biases at 150°C for 15 min: (a) unannealed capacitor, and (b) capacitor annealed at 400°C.

same BTS condition. Nevertheless, BTS measurement, combined with other characterization techniques, has been successfully used to study Cu ion diffusion in xerogel dielectric revealing that Cu ion diffusion was retarded in nanoporous silica [197-199]. In the study, the BTS result of the unannealed sample shows little flat-band voltage shift under a constant positive or negative gate bias stress (± 20 V) as shown in Fig. 7.6(a). Figure 7.6(b) shows the BTS result for the film stack annealed at 400°C, and little flat-band voltage shift was observed as well, suggesting that Cu diffusion into the trimethylsilylated mesoporous silica dielectric layer after the 400°C anneal was negligible.

7.3 Summary

In summary, thermal and electrical stability of a Cu/Ta(N)/mesoporous silica/Si film stack was studied. Hydrophobicity of the as-calcined mesoporous silica films spin coated on Si wafers was significantly improved by trimethylsilylation with HMDS vapor treatment. The presence of hydrophobic trimethylsilyl groups on the pore surface greatly enhances the resistance to moisture uptake, hence improving the dielectric property of the mesoporous film. According to FTIR, TDS, and AES studies, the trimethylsilylated mesoporous silica dielectric is thermally stable up to 400°C, and reliable over 50 days in terms of the dielectric and chemical properties. Decomposition of trimethylsilyl groups in the trimethylsilylated mesoporous silica thin film becomes obvious around 450°C, and the mesoporous silica suffers serious degradation in chemical structure when the annealing temperature reaches 600°C. However, decomposition-induced chemical degradation seemed not to cause any film crack and interfacial failure in the Cu-metallized mesoporous silica film stack, even for the sample annealed at 600°C. HRTEM study reveals that a small number of Ta₂C nanocrystals were formed at the interface between the Ta(N) barrier layer and the mesoporous silica layer. The Ta₂C nanocrystal is suggested to be the reaction product of the decomposed alkyl species in

the mesoporous silica layer and the Ta barrier layer during the high-temperature annealing process. The formation of the nanocrystal can relieve the tendency of possible film damage induced by the rapid evolution of gaseous decomposed species in the mesoporous silica layer. BTS measurements indicate that Cu diffusion into the mesoporous silica layer can be completely retarded in the Cu/Ta(N) metallize film stack annealed at 400°C. The study shows that the trimethylsilylated mesoporous silica thin film is thermally and electrically stable up to 400°C, and is a potential candidate as an ultralow- k dielectric for Cu damascene structure.



Chapter 8

Conclusions and Suggestions for Future Work

8.1 Conclusions

Mesoporous silica low- k films with a periodic pore structure were successfully fabricated by self-assembled molecularly templation. The mesoporous silica films were deposited by spin-coating. The as-calcined films have small pores (4-6 nm) and a narrow pore size distribution. The thickness of the as-calcined films is well controlled within the range 250-450 nm, and the mean surface roughness was estimated to be ≤ 1 nm. The dielectric and mechanical properties and the thermal stability of mesoporous silica low- k thin films were studied herein. The primary results are as follows.

- a. Mesoporous silica thin films have a tunable/extendable dielectric constant from 1.5 to 2.5, depending on the method of preparation of the precursor solution and modification of methylsilylation agents.
- b. Trimethylsilylation significantly improves the hydrophobicity of the mesoporous silica thin films. Stable dielectric properties thus can be obtained.
- c. Self-assembled templated mesoporous silica thin films with P123 have a well-ordered hexagonal pore channel structure and, therefore, have better mechanical properties than other porous low- k dielectrics.
- d. When TMCS agent was added to the silica precursor solution, the resulting mesoporous films were mechanically weakened. The pore channel structure and the chemical structure of the solid matrix of the porous network of the TMCS-derivatized mesoporous films are less ordered than that of the as-calcined films.

- e. Unlike TMCS, trimethylsilylation by HMDS vapor treatment effectively improves the mechanical strength of mesoporous silica thin films. This fact is explained in terms of the pore microstructure of the mesoporous silica network and the spring-back effect associated with the presence of trimethylsilyl groups in the nanopores.
- f. The as-calcined mesoporous silica thin films have tensile stress, because of film shrinkage following the bake and calcination processes. HMDS treatment markedly relieves this tensile stress by the spring-back effect.
- g. The deposition of low-temperature HDP-CVD α -SiC:H films can also relieve the tensile stress in a mesoporous silica thin film, causing the film stack to become compressively stressed due to the stress compensation and alkoxylation-induced spring-back effect.
- h. The trimethylsilylated mesoporous silica dielectric is thermally and electrically stable up to 400°C, and its dielectric and chemical properties remain stable for 50 days.

8.2 Suggestions for Future Work

Several topics warrant further study.

- a. Some etching-related problems may cause integration failures; (i) etch rate and selectivity control; (ii) killer pores, which result in low- k voiding; (iii) etching profile associated with the pore distribution; (iv) loading and microloading effects; (v) etch species traps, and (vi) post-clean damage.
- b. Other film characteristics, including thermal conductivity and fracture toughness, should be studied. New characterization approaches may be required.
- c. Current advanced Cu/barrier deposition techniques involve atomic layer deposition (ALD). Low- k dielectrics combined with Cu/barrier ALD should be developed in the future.
- d. When porous ultralow- k dielectrics are integrated in the Cu damascene architecture, using advanced metallic barriers, the metallic barrier precursors may diffuse into porous

dielectrics. A credible pore sealing treatment must thus be developed to close the surface porosity of the trench sidewalls before the barrier is deposited.

- e. Future studies should examine the mechanical reliability of mesoporous silica films with a dual damascene structure during the CMP process.



References

1. J. Singh, *Semiconductor Devices: Basic Principles* (John Wiley & Sons, New York, 2001), Chap. 10.
2. M. T. Bohr, Tech. Digest IEEE Int. Electronic Device Meeting, 241 (1995).
3. *National Technology Roadmap for Semiconductors (NTRS)*, 1997 edition (Semiconductor Industry Association, San Jose, California).
4. <http://www.spectrum.ieee.org/WEBONLY/publicfeature/feb03/film.html>.
5. *International Technology Roadmap for Semiconductors (ITRS)*, 2005 edition (<http://public.itrs.net/>).
6. S. J. Martin, J. P. Godschalx, M. E. Mills, E. O. Shaffer II, and P. H. Townsend, *Adv. Mater.*, **12**, 1769 (2000).
7. R. S. List, A. Singh, A. Ralston, and G. Dixit, *Mat. Res. Soc. Bull.*, **22**, 61 (1997).
8. N. Aoi, *Jpn. J. Appl. Phys.*, **36**, 1355 (1997).
9. T. Ramos, K. Roderick, A. Maskara, and D. M. Smith, *Mat. Res. Soc. Symp. Proc.*, **443**, 91 (1997).
10. M. H. Jo, H. H. Park, D. J. Kim, S. H. Hyun, S. Y. Choi, and J. T. Paik, *J. Appl. Phys.*, **82**, 1299 (1997).
11. J. J. Kim, S. B. Jung, H. H. Park, and S. H. Hyun, *Thin Solid Films*, **377**, 467 (2000).
12. S. V. Nitta, A. Jain, P. C. Wayner, Jr., W. N. Gill, and J. L. Plawsky, *J. Appl. Phys.*, **86**, 5870 (1999).
13. D. Y. Zhao, P. Yang, N. Melosh, J. L. Feng, B. F. Chmelka, and G. D. Stucky, *Adv. Mater.*, **10**, 1380 (1998).
14. S. Baskaran, J. Liu, K. Domansky, N. Kohler, X. Li, C. Coyle, G. E. Fryxell, S. Thevuthasan, and R. E. Williford, *Adv. Mater.*, **12**, 291 (2000).
15. T. G. Tsai, A. T. Cho, C. M. Yang, F. M. Pan, and K. J. Chao, *J. Electrochem. Soc.*, **149**,

- F116 (2002).
16. C. M. Yang, A. T. Cho, F. M. Pan, T. G. Tsai, and K. J. Chao, *Adv. Mater.*, **13**, 1099 (2001).
 17. H. Miyoshi, H. Matsuo, Y. Oku, H. Tanaka, K. Yamada, N. Mikami, S. Takada, N. Hata, and T. Kikkawa, *Jpn. J. Appl. Phys.*, **43**, 498 (2004).
 18. J. Y. Chen, F. M. Pan, A. T. Cho, K. J. Chao, T. G. Tsai, B. W. Wu, C. M. Yang, and L. Chang, *J. Electrochem. Soc.*, **150**, F123 (2003).
 19. J. Y. Chen, F. M. Pan, L. Chang, A. T. Cho, and K. J. Chao, *J. Vac. Sci. Technol. B*, **23**, 2034 (2005).
 20. A. T. Cho, T. G. Tsai, C. M. Yang, K. J. Chao, and F. M. Pan, *Electrochem. Solid-State Lett.*, **4**, G35 (2001).
 21. S. V. Nitta, V. Pisupatti, A. Jain, P. C. Wayner, Jr., W. N. Gill, and J. L. Plawsky, *J. Vac. Sci. Technol. B*, **17**, 205 (1999).
 22. V. M. Gunko, M. S. Vedamuthu, G. L. Henderson, and J. P. Blitz, *J. Colloid Interface Sci.*, **228**, 157 (2000).
 23. P. Atkins and J. de Paula, *Atkins' Physical Chemistry*, 7th ed. (Oxford University Press, New York, 2002).
 24. S. O. Kasap, *Principles of Electrical Engineering Materials and Devices* (McGraw-Hill, New York, 1997), Chap. 7.
 25. K. J. Miller, H. B. Hollinger, J. Grebowicz, and B. Wunderlich, *Macromolecules*, **23**, 3855 (1990).
 26. G. Hougham, G. Tesoro, A. Viehbeck, and J. D. Chapple-Sokol, *Macromolecules*, **27**, 5964 (1994).
 27. L. W. Hrubesh, L. E. Keene, and V. R. Latorre, *J. Mater. Res.*, **8**, 1736 (1993).
 28. J. W. Coburn and H. F. Winters, *J. Appl. Phys.*, **50**, 3189 (1979).

29. R. H. Baney, A. Itoh, A. Sakakibara, and T. Suzuki, *Chem. Rev.*, **95**, 1409 (1995).
30. R. F. Cook, E. G. Liniger, D. P. Klaus, E. E. Simonyi, and S. A. Cohen, *Mater. Res. Soc. Symp. Proc.*, **511**, 33 (1998).
31. P. T. Liu, T. C. Chang, Y. S. Mor, and S. M. Sze, *Jpn. J. Appl. Phys.*, **38**, 3482 (1999).
32. H. C. Liou, and J. Pretzer, *Thin Solid Films*, **335**, 186 (1998).
33. H. C. Liou, and J. Pretzer, *Mater. Res. Soc. Symp. Proc.*, **565**, 239 (1999).
34. N. P. Hacker, *Mater. Res. Soc. Bull.*, **22**, 33 (1997).
35. E. T. Ryan, A. J. McKerrow, J. Leu, and P. S. Ho, *Mater. Res. Soc. Bull.*, **22**, 49 (1997).
36. S. L. Rosen, *Fundamental Principles of Polymeric Materials*, 2nd ed. (John Wiley & Sons, New York, 1993).
37. J. H. Lai, S. A. Jenekhe, R. J. Jensen, and M. Roer, *Solid State Technol.*, **27**, 39 (1984).
38. B. Cruden, K. Chu, K. Gleason, and H. Sawin, *J. Electrochem. Soc.*, **146**, 4590 (1999).
39. L. G. Jacobsohn, D. F. Franceschini, M. E. H. Maia da Costa, and F. L. Jr. Freire, *J. Vac. Sci. Technol. A*, **18**, 2230 (2000).
40. M. Ohring, *Engineering Materials Science* (Academic Press, San Diego, 1995).
41. M. E. Mills, P. Townsend, D. Castillo, S. Martin, and A. Achen, *Microelectron. Eng.*, **33**, 327 (1997).
42. A trademark of Dow Chemical (<http://www.dow.com>).
43. P. H. Townsend, S. J. Martin, J. Godschal, D. R. Romer, D. W. Jr. Smith, D. Castillo, R. DeVries, G. Buske, N. Rondan, S. Froelicher, J. Marshall, E. O. Shaffer, and J. H. Im, *Mater. Res. Soc. Symp. Proc.*, **476**, 9 (1997).
44. A trademark of Honeywell (<http://www.electronicmaterials.com>).
45. G. D. Goldblatt, B. Agarwala, M. B. Anand, E. P. Barth, G. A. Biery, Z. G. Chen, S. Cohen, J. B. Connolly, A. Cowley, T. Dalton, S. K. Das, C. R. Davis, A. Deutsch, C. DeWan, D. C. Edelstein, P. A. Emmi, C. G. Faltermeier, J. A. Fitzsimmons, J. Hedrick, J.

- E. Heindenreich, C. K. Hu, J. P. Hummel, P. Jones, E. Kaltalioglu, B. E. Kastenmeier, M. Krishnan, W. F. Landers, E. Liniger, J. Liu, N. E. Lustig, S. Malhotra, D. K. Manger, V. McGahay, R. Mih, H. A. Nye, S. Purushothaman, H. A. Rathore, S. C. Seo, T. M. Shaw, A. H. Simon, T. A. Spooner, M. Stetter, R. A. Wachnik, J. G. Ryan, *Proc. Int. Interconnect Tech. Conf.*, 261 (2000).
46. <http://www.eetimes.com/news/semi/showArticle.jhtml?articleID=10807823>.
47. <http://www.eet.com/news/latest/showArticle.jhtml?articleID=18308274>.
48. K. Endo, T. Tatsumi, *J. Appl. Phys.*, **78**, 1370 (1995).
49. K. Endo, *Mater. Res. Soc. Bull.*, **22**, 55 (1997).
50. H. Yang, D. J. Tweet, Y. Ma, T. Nguijen, D. R. Evans, and S. T. Hsu, *Mater. Res. Soc. Symp. Proc.*, **511**, 233 (1998).
51. A. Grill, V. Patel, K. L. Saenger, C. Jahnes, S. A. Cohen, A. G. Schrott, D. C. Edelstein, and J. R. Paraszczak, *Mater. Res. Soc. Symp. Proc.*, **443**, 155 (1997).
52. A. Grill, C. Jahnes, V. Patel, and J. Ott, *Mater. Res. Soc. Symp. Proc.*, **511**, 223 (1998).
53. Y. Matsumoto and M. Ishida, *Sens. Actuators*, **83**, 179 (2000).
54. E. Korczynski, *Solid State Technol.*, **42**, 22 (1999).
55. M. Uhlig, A. Bertz, M. Rennau, S. E. Schulz, T. Werner, and T. Gessner, *Microelectron. Eng.*, **50**, 7 (2000).
56. K. Endo, K. Shinoda, and T. Tatsumi, *J. Appl. Phys.*, **86**, 2739 (1999).
57. S. S. Han, H. R. Kim, and B. S. Bae, *J. Electrochem. Soc.*, **146**, 3383 (1999).
58. J. M. Shieh, S. C. Suen, K. C. Tsai, B. T. Dai, Y. C. Wu, and Y. H. Wu, *J. Vac. Sci. Technol. B*, **19**, 780 (2001).
59. S. Agraharam, D. W. Hess, P. A. Kohl, and S. A. B. Allen, *J. Electrochem. Soc.*, **148**, F102 (2001).
60. M. J. Loboda, *Microelectron. Eng.*, **50**, 15 (2000).

61. H. G. P. Lewis, D. J. Edell, and K. Gleason, *Chem. Mater.*, **12**, 3488 (2000).
62. Q. Wu and K. Gleason, *J. Vac. Sci. Technol. A*, **21**, 388 (2003).
63. A. Grill, *Thin Solid Films*, **398-399**, 527 (2001).
64. A. Grill and V. Patel, *Appl. Phys. Lett.*, **79**, 803 (2001).
65. C. C. Chiang, M. C. Chen, L. J. Li, Z. C. Wu, S. M. Jang, and M. S. Liang, *J. Electrochem. Soc.*, **151**, G612 (2004).
66. M. L. O'Neill, R. N. Vrtis, J. L. Vincent, A. S. Lukas, E. J. Karwacki, B. K. Peterson, and M. D. Bitner, *Mater. Res. Soc. Symp. Proc.*, **766**, E8.17.1 (2003).
67. <http://www.reed-electronics.com/semiconductor/index.asp?layout=articlePrint&articleID=CA218635>.
68. A trademark of Novellus Systems (<http://www.novellus.com>).
69. A trademark of Applied Materials (www.appliedmaterials.com).
70. <http://www.tsmc.com.tw>.
71. <http://www.reed-electronics.com/semiconductor/index.asp?layout=articlePrint&articleID=CA279106>.
72. T. Ramos, K. Roderick, A. Maskara, and D. M. Smith, *Mater. Res. Soc. Symp. Proc.*, **443**, 47 (1997).
73. S. Acosta, A. Ayril, C. Guizard, C. Lecornec, G. Passemar, and M. Moussavi, *Mater. Res. Soc. Symp. Proc.*, **612**, D5.26.1 (2000).
74. P. J. Bruinsma, N. J. Hess, J. R. Botha, J. Liu, and S. Baskaran, *Mater. Res. Soc. Symp. Proc.*, **443**, 105 (1997)
75. H. Fan, H. R. Bentley, K. R. Kathan, P. Clem, Y. Lu, and C. J. Brinker, *J. Non-Cryst. Solids*, **285**, 79 (2001).
76. S. Seraji, Y. Wu, M. Forbess, S. J. Limmer, T. Chou, and G. Cao, *Adv. Mater.*, **12**, 1695 (2000).

77. Z. Wang, H. Wang, A. Mitra, L. Huang, and Y. Yan, *Adv. Mater.*, **13**, 746 (2001).
78. R. M. A. Azzam, N. M. Bashara, *Ellipsometry and Polarized Light* (Elsevier, Amsterdam, 1977).
79. A trademark of JSR microelectronics (<http://www.jsrusa.com>).
80. A trademark of Dow Corning (<http://www.dowcorning.com>).
81. C. J. Brinker and G. W. Scherer, *Sol-Gel Science: The Physics and Chemistry of Sol-Gel Processing* (Academic Press, San Diego, 1990).
82. A. M. Buckley and M. Greenblatt, *J. Non-Cryst. Solids*, **143**, 1 (1992).
83. S. Acosta, A. Ayral, C. Guizard, C. Lecornec, G. Passemard, and M. Moussavi, *Mater. Res. Soc. Symp. Proc.*, **612**, D5.26.1 (2000).
84. C. T. Kresge, M. E. Leonowicz, W. J. Roth, J. C. Vartuli, and J. S. Beck, *Nature*, **359**, 710 (1992).
85. J. S. Beck, J. C. Vartuli, W. J. Roth, M. E. Leonowicz, C. T. Kresge, K. D. Schmitt, C. T. W. Chu, D. H. Olson, E. W. Sheppard, S. B. McCullen, J. B. Higgins, and J. L. Schlenker, *J. Am. Chem. Soc.*, **114**, 10834 (1992).
86. J. Jarupatrakorn and J. D. Tilley, *J. Am. Chem. Soc.*, **124**, 8380 (2002).
87. M. A. Markowitz, J. Klaehn, R. A. Hendel, S. B. Qadriq, S. L. Golledge, D. G. Castner, and B. P. Gaber, *J. Phys. Chem. B*, **104**, 10820 (2000).
88. J. W. Zhao, F. Gao, Y. L. Fu, W. Jin, P. Y. Yang, and D. Y. Zhao, *Chem. Commun.*, 752 (2002).
89. P. D. Yang, G. Wirnsberger, H. C. Huang, S. R. Cordero, M. D. McGehee, B. Scott, T. Deng, G. M. Whitesides, B. F. Chmelka, S. K. Buratto, and G. D. Stucky, *Science*, **287**, 465 (2000).
90. T. Yamada, H. S. Zhou, H. Uchida, M. Tomita, Y. Ueno, T. Ichino, I. Honma, K. Asai, and T. Katsube, *Adv. Mater.*, **14**, 812 (2002).

91. S. H. Joo, S. J. Choi, I. Oh, J. Kwak, Z. Liu, O. Terasaki, and R. Ryoo, *Nature*, **412**, 169 (2001).
92. A. Sayari, I. Moudrakovski, J. S. Reddy, C. I. Ratcliffe, J. A. Ripmeester, and K. F. Preston, *Chem. Mat.*, **8**, 2080 (1996).
93. J. M. Thomas, O. Terasaki, P. L. Gai, W. Zhou, and J. Gonzalez-Calbet, *Accounts Chem. Res.*, **34**, 583 (2001).
94. Y. H. Sakamoto, M. Kaneda, O. Terasaki, D. Y. Zhou, J. M. Kim, G. Stucky, H. J. Shin, and R. Ryoo, *Nature*, **408**, 449 (2000).
95. M. Kruk, M. Jaroniec, Y. Sakamoto, O. Terasaki, R. Ryoo, and C. H. Ko, *J. Phys. Chem. B*, **104**, 292 (2000).
96. M. S. Wong, H. C. Huang, and J. Y. Ying, *Chem. Mat.*, **14**, 1961 (2002).
97. T. R. Pauly and T. J. Pinnavaia, *Chem. Mat.*, **13**, 987 (2001).
98. M. S. Wong, E. S. Jeng, and J. Y. Ying, *Nano. Lett.*, **1**, 637 (2001).
99. Q. Huo, D. I. Margolese, U. Ciesla, D. G. Demuth, P. Feng, T. E. Gier, P. Sieger, A. Firouzi, B. F. Chmelka, F. Schüth, and G. D. Stucky, *Chem. Mat.*, **6**, 1176 (1994).
100. Q. Huo, D. I. Margolese, U. Ciesla, P. Feng, T. E. Gier, P. Sieger, R. Leon, P. M. Petroff, F. Schüth, and G. D. Stucky, *Nature*, **368**, 317 (1994).
101. P. T. Tanev and T. J. Pinnavaia, *Science*, **267**, 865 (1995).
102. S. A. Bagshaw, E. Prouzet, and T. J. Pinnavaia, *Science*, **269**, 1242 (1995).
103. D. Y. Zhao, J. L. Feng, Q. S. Huo, N. Melosh, G. H. Fredrickson, B. F. Chmelka, and G. D. Stucky, *Science*, **279**, 548 (1998).
104. D. Y. Zhao, Q. S. Huo, J. L. Feng, B. F. Chmelka, and G. D. Stucky, *J. Am. Chem. Soc.*, **120**, 6024 (1998).
105. M. S. Wong and J. Y. Ying, *Chem. Mat.*, **10**, 2067 (1998).
106. M. R. Porter, *Handbook of Surfactants* (Chapman and Hall, New York, 1991).

107. T. Adachi and S. Sakka, *J. Mater. Sci.*, **25**, 4732 (1990).
108. C. M. Flannery, C. Murray, I. Streiter, and S. E. Schulz, *Thin Solid Films*, **388**, 1 (2001).
109. T. Woignier, J. Reynes, A. H. Alaoui, I. Beurroies, and J. Phalippou, *J. Non-Cryst. Solids*, **241**, 45 (1998).
110. L. A. Chow, B. Dunn, K. N. Tu, and C. Chiang, *J. Appl. Phys.*, **87**, 7788 (2000).
111. J. H. Zhao, Y. Du, M. Morgen, and P. S. Ho, *J. Appl. Phys.*, **87**, 1575 (2000).
112. M. Moner-Girona, A. Roig, E. Molins, E. Martinez, and J. Esteve, *Appl. Phys. Lett.*, **75**, 653 (1999).
113. B. D. Fabes and W. C. Oliver, *J. Non-Cryst. Solids*, **121**, 348 (1990).
114. W. D. Nix, *Metall. Trans. A*, **20**, 2217 (1989).
115. C. Chiang, A. S. Mack, C. Pan, Y. Ling, and D. Fraser, *Mater. Res. Soc. Symp. Proc.*, **381**, 123 (1995).
116. A. Jain, S. Rogojevic, W. N. Gill, J. L. Plawsky, I. Matthew, M. Tomozawa, and E. Simonyi, *J. Appl. Phys.*, **90**, 5832 (2001).
117. H. Miyoshi, H. Matsuo, Y. Oku, H. Tanaka, K. Yamada, N. Mikami, S. Takada, N. Hata, and T. Kikkawa, *Jap. J. Appl. Phys.*, **43**, 498 (2004).
118. S. Takada, N. Hata, Y. Seino, K. Yamada, Y. Oku, and T. Kikkawa, *Jap. J. Appl. Phys.*, **43**, 2453 (2004).
119. Y. Oku, K. Yamada, T. Goto, Y. Seino, A. Ishikawa, T. Ogata, K. Kohmura, N. Fujii, N. Hata, R. Ichikawa, T. Yoshino, C. Negoro, A. Nakano, Y. Sonoda, S. Katada, H. Miyoshi, S. Oike, H. Tanaka, H. Matsuo, K. Kinoshita, and T. Kikkawa, *IEEE International Electron Devices Meeting Technical Digest*, 139 (2003).
120. B. P. Gorman, R. A. Orozco-Teran, J. A. Roepsch, H. Dong, R. F. Reidy, and D. W. Mueller, *Appl. Phys. Lett.*, **79**, 4010 (2001).
121. J. B. Vella, A. A. Volinsky, I. S. Adhietty, N. V. Edwards, and W. W. Gerberich, *Mater.*

- Res. Soc. Symp. Proc.*, **716**, B12.13.1 (2002).
122. N. Fujii, K. Yamada, Y. Oku, N. Hata, Y. Seino, C. Negoro, and T. Kikkawa, *Mater. Res. Soc. Symp. Proc.*, **812**, F4.10.1 (2004).
123. Y. Toivola, J. Thurn, and R. F. Cook, *J. Electrochem. Soc.*, **149**, F9 (2002).
124. R. W. Rice, *J. Am. Ceram. Soc.*, **76**, 1801 (1993).
125. R. W. Rice, *J. Mater. Sci.*, **31**, 102 (1996).
126. R. W. Rice, *J. Mater. Sci.*, **31**, 1509 (1996).
127. E. J. Garboczi and A. R. Day, *J. Mech. Phys. Solids*, **43**, 1349 (1995).
128. A. P. Roberts and E. J. Garboczi, *J. Am. Ceram. Soc.*, **83**, 3041 (2000).
129. D. Edelstein, C. Uzoh, C. Cabral, Jr., P. DeHaven, P. Buchwalter, A. Simon, E. Cooney, S. Malholtra, D. Klaus, H. Rathore, B. Ararwala and D. Nguyen, *Proc. of the IEEE 2001 International Interconnect Technology Conference*, 9 (2001).
130. A. Kumar, H. Bakhru, C. Jin, W. W. Lee, and T. M. Lu, *J. Appl. Phys.*, **87**, 3567 (2000).
131. S. Rogojevic, A. Jain, F. Wang, W. N. Gill, P. C. Wayner, Jr., J. L. Plawsky, T. M. Lu, G. R. Yang, W. A. Lanford, A. Kumar, H. Bakhru, and A. N. Roy, *J. Vac. Sci. Technol. B*, **19**, 354 (2001).
132. H. Windischmann, *J. Vac. Sci. Technol. A*, **9**, 2459 (1991).
133. M. A. El Khakani, M. Chaker, A. Jean, S. Boily, H. Pépin, J. C. Kieffer, and S. C. Gujrathi, *J. Appl. Phys.*, **74**, 2834 (1993).
134. P. M. Sarro, C. R. deBoer, E. Korkmaz, and J. M. W. Laros, *Sens. Actuat. A*, **67**, 175 (1998).
135. A. Klumpp, U. Schaber, H. L. Offereins, K. Kühl, and H. Sandmaier, *Sens. Actuat. A*, **41-42**, 310 (1994).
136. P. R. McCurdy, J. M. Truitt, and E. R. Fisher, *J. Vac. Sci. Technol. A*, **17**, 2475 (1999).
137. M. S. Lee, and S. F. Bent, *J. Vac. Sci. Technol. A*, **16**, 1658 (1998).

138. M. J. Loboda, J. A. Seifferly, and F. C. Dall, *J. Vac. Sci. Technol. A*, **12**, 90 (1994).
139. M. T. Kim, and J. Lee, *Thin Solid Films*, **303**, 173 (1997).
140. T. Stapinski, G. Ambrosone, U. Coscia, F. Giorgis, and C. F. Pirri, *Physica B*, **254**, 99 (1998).
141. J. Seekamp, and W. Bauhofer, *J. Non-Cryst. Solids*, **227-230**, 474 (1998).
142. F. Giorgis, F. Giuliani, C. F. Pirri, E. Tresso, J. P. Conde, and V. Chu, *J. Non-Cryst. Solids*, **227-230**, 465 (1998).
143. T. E. F. M. Standaert, M. Schaepkens, N. R. Rueger, P. G. M. Sebel, G. S. Oehrlein, and J. M. Cook, *J. Vac. Sci. Technol. A*, **16**, 239 (1998).
144. T. E. F. M. Standaert, P. J. Matsuo, S. D. Allen, G. S. Oehrlein, and T. J. Dalton, *J. Vac. Sci. Technol. A*, **17**, 741 (1999).
145. T. E. F. M. Standaert, E. A. Joseph, G. S. Oehrlein, A. Jain, W. N. Gill, P. C. Wayner, Jr., and J. L. Plawsky, *J. Vac. Sci. Technol. A*, **18**, 2742 (2000).
146. T. E. F. M. Standaert, C. Hedlund, E. A. Joseph, G. S. Oehrlein, and T. J. Dalton, *J. Vac. Sci. Technol. A*, **22**, 53 (2004).
147. C. J. Brinker, Y. Lu, A. Sellinger, and H. Fan, *Adv. Mater.*, **11**, 579 (1999).
148. S. Rogojevic, A. Jain, F. Wang, W. N. Gill, J. L. Plawsky, and T. M. Lu, *J. Electrochem. Soc.*, **149**, F122 (2002).
149. W. C. Oliver and G. M. Pharr, *J. Mater. Res.*, **7**, 1564 (1992).
150. A. C. Fischer-Cripps, *Nanoindentation* (Springer-Verlag, New York, 2002).
151. G. G. Stoney, *Proc. R. Soc. Lond. A*, **82**, 172 (1909).
152. J. H. Zhao, I. Malik, T. Ryan, E. T. Ogawa, and P. S. Ho, *Appl. Phys. Lett.*, **74**, 944 (1999).
153. M. Ohring, *The Materials Science of Thin Films*, (Academic Press, San Diego, 1992).
154. J. H. Zhao, I. Malik, T. Ryan, E. T. Ogawa, P. S. Ho, W. Y. Shih, A. J. McKerrow, and K.

- J. Taylor, *Appl. Phys. Lett.*, **74**, 944 (1999).
155. L. W. Hrubesh and J. F. Poco, *Mater. Res. Soc. Symp. Proc.*, **371**, 195 (1995).
156. <http://www.sigmaaldrich.com/catalog/search/ProductDetail/ALDRICH/435465>.
157. J. J. Kim, H. H. Park, and S. H. Hyun, *Thin Solid Films*, **377-378**, 525 (2000).
158. B.C. Smith, *Infrared Spectral Interpretation: A Systematic Approach* (CRC Press, Boca Raton, Florida, 1999).
159. P. Innocenzi, *J. Non-Cryst. Solids*, **316**, 309 (2003).
160. T. C. Chang, P. T. Liu, Y. S. Mor, S. M. Sze, Y. L. Yang, M. S. Feng, F. M. Pan, B. T. Dai and C. Y. Chang, *J. Electrochem. Soc.*, **146**, 3802 (1999).
161. S. Yu, T. K. S. Wong, K. Pita, X. Hu, and V. Ligatchev, *J. Appl. Phys.*, **92**, 3338 (2002).
162. V. M. Gun'ko, M. S. Vedamuthu, G. L. Henderson, and J. P. Blitz, *J. Colloid Interface Sci.*, **228**, 157 (2000).
163. T. Kikkawa, R. Yagi, S. Chikaki, M. Shimoyama, T. Ono, N. Fujii, K. Kohmura, H. Tanaka, T. Nakayama, A. Ishikawa, H. Matsuo, Y. Sonoda, N. Hata, Y. Seino, T. Yoshino, and K. Kinoshita, *Proc. of SPIE*, **6002**, 60020M (2005).
164. E. Kondoh, T Asano, H. Arao, A. Nakashima and M. Komatsu, *Jpn. J. Appl. Phys.*, **39**, 3919 (2000).
165. M. Yoshimaru, S. Koizumi, K. Shimokawa, and J. Ida, *IEEE Reliability Phys. Symp.*, 234 (1997).
166. D. R. Lide and H. P. R. Frederikse, *CRC Handbook of Physics and Chemistry: A Ready-reference Book of Chemical and Physical Data*, 76th ed. (CRC Press, Boca Raton, Florida, 1995-1996).
167. C. Vautey, M. Burgos, and M. Langlet, *Thin Solid Films*, **347**, 184 (1999).
168. C. T. Kirk, *Phys. Rev. B*, **38**, 1255 (1988).
169. P. H. Gaskell and D. W. Johnson, *J. Non-Cryst. Solids*, **20**, 171 (1976).

170. N. Primeau, C. Vautey and M. Langlet, *Thin Solid Films*, **310**, 47 (1997).
171. H. G. P. Lewis, T. B. Casserly and K. K. Gleason, *J. Electrochem. Soc.*, **148**, F212 (2001).
172. D. M. Smith, D. Stein, J. M. Anderson and W. Ackerman, *J. Non-Cryst. Solids*, **186**, 104 (1995).
173. X. E. Guo and L. J. Gibson, *International J. Mech. Sci.*, **41**, 85 (1999).
174. S. S. Prakash, C. J. Brinker, A. J. Hurd, and S. M. Rao, *Nature*, **374**, 439 (1995).
175. H. Windischmann, *J. Vac. Sci. Technol. A*, **9**, 2459 (1991).
176. M. A. El Khakani, M. Chaker, A. Jean, S. Boily, H. Pépin, J. C. Kieffer, and S. C. Gujrathi, *J. Appl. Phys.*, **74**, 2834 (1993).
177. P. M. Sarro, C. R. deBoer, E. Korkmaz, and J. M. W. Laros, *Sens. Actuat. A*, **67**, 175 (1998).
178. A. Klumpp, U. Schaber, H. L. Offereins, K. Kühl, and H. Sandmaier, *Sens. Actuat. A*, **41-42**, 310 (1994).
179. P. R. McCurdy, J. M. Truitt, and E. R. Fisher, *J. Vac. Sci. Technol. A*, **17**, 2475 (1999).
180. M. S. Lee, and S. F. Bent, *J. Vac. Sci. Technol. A*, **16**, 1658 (1998).
181. M. J. Loboda, J. A. Seifferly, and F. C. Dall, *J. Vac. Sci. Technol. A*, **12**, 90 (1994).
182. M. T. Kim, and J. Lee, *Thin Solid Films*, **303**, 173 (1997).
183. T. Stapinski, G. Ambrosone, U. Coscia, F. Giorgis, and C. F. Pirri, *Physica B*, **254**, 99 (1998).
184. J. Seekamp, and W. Bauhofer, *J. Non-Cryst. Solids*, **227-230**, 474 (1998).
185. F. Giorgis, F. Giuliani, C. F. Pirri, E. Tresso, J. P. Conde, and V. Chu, *J. Non-Cryst. Solids*, **227-230**, 465 (1998).
186. F. M. Pan, B. W. Wu, A. T. Cho, K. C. Tsai, T. G. Tsai, K. J. Chao, J. Y. Chen, and L. Chang, *J. Vac. Sci. Technol. B*, **22**, 1067 (2004).

187. J. M. Shieh, K. C. Tsai, and B. T. Dai, *Appl. Phys. Lett.*, **81**, 1294 (2002).
188. J. N. Bremmer, Y. Liu, K. G. Gruszynski, and F. C. Dall, *Mater. Res. Soc. Symp. Proc.*, **476**, 37 (1997).
189. G. Garlotti, L. Doucet, and M. Dupeux, *J. Vac. Sci. Technol. B*, **14**, 3460 (1996).
190. J. H. Zhao, T. Ryan, P. S. Ho, A. J. Mckerrow, and W. Y. Shih, *J. Appl. Phys.*, **85**, 6421 (1999).
191. M. L. O'Neill, Y. L. Cheng, A. S. Lukas, Y. L. Wang, E. J. Karwacki, M. S. Feng, R. N. Vrtis, J. L. Vincent, B. K. Peterson, and M. D. Bitner, *Mat. Res. Soc. Symp. Proc.*, **766**, E7.3.1 (2003).
192. D. D. Burkey and K. K. Gleason, *Mat. Res. Soc. Symp. Proc.*, **766**, E6.7.1 (2003).
193. P. Villars and L. D. Calvert, *Pearson's Handbook of Crystallographic Data for Intermetallic Phases*, 2nd ed. (ASM International, 1991), pp. 2012, **2**.
194. R. Leyva-Ramos and C. J. Geankoplis, *Chem. Eng. Sci.*, **40**, 799 (1985).
195. W. C. Reyes, J. H. Sinfelt, and G. J. DeMartin, *J. Phys. Chem. B*, **104**, 5750 (2000).
196. H. Y. Tsai, S. C. Sun, and S. J. Wang, *J. Electrochem. Soc.*, **147**, 2766 (2000).
197. B. G. Willis, and D. V. Lang, *Thin Solid Films*, **467**, 284 (2004).
198. T. Yoshino, N. Hata and T. Kikkawa, *Mat. Res. Soc. Symp. Proc.*, **766**, E1.7.1 (2003).
199. S. Rogojevic, A. Jain, W. N. Gill, and J. L. Plawsky, *J. Electrochem. Soc.*, **149**, F122 (2002).

Vita

基本資料

- 姓名：陳致宇 (Jr-Yu Chen)
- 性別：男
- 出生年月日：民國 66 年 11 月 14 日
- 籍貫：台北市
- 電子信箱：jryu.mse89g@nctu.edu.tw

學歷

- 國立交通大學 材料科學與工程系博士班
(民國 90 年 9 月 至 民國 95 年 7 月)
- 國立交通大學 材料科學與工程系碩士班
(民國 89 年 9 月 至 民國 90 年 6 月)
- 私立大同大學 材料工程學系
(民國 85 年 9 月 至 民國 89 年 6 月)

經歷

- 國立交通大學日語研習社現任社員
- 國立交通大學材料所材料表面科學以及相變化課程助教
- 八十七學年度私立大同大學材料工程學系班代
- 八十六學年度私立大同大學跆拳道社社長

專長

- 材料特性與結構分析
- 積體電路製程技術

✚ 學位論文

- 介孔洞二氧化矽超低介電薄膜在積體電路技術之應用積體電路製程技術
Mesoporous Silica Thin Films as Ultralow- k Dielectrics for ULSI Applications

✚ 著作

● 國際期刊論文

1. Jr-Yu Chen, Fu-Ming Pan, An-Thung Cho, Kuei-Jung Chao, Tzeng-Guang Tsai, Bo-Wei Wu, Chia-Min Yang, and Li Chang, “Microstructure and mechanical properties of surfactant templated nanoporous silica thin films: Effect of methylsilylation,” *J. Electrochem. Soc.*, **150**, F123 (2003).
2. Fu-Ming Pan, Bo-Wei Wu, An-Thung Cho, Kuo-Chiang, Tzeng-Guang Tsai, Kuei-Jung Chao, Jr-Yu Chen, and Li Chang, “Alkylation of nanoporous silica thin films by high density plasma chemical vapor deposition of a-SiC:H,” *J. Vac. Sci. Technol. B*, **22**, 1067 (2004).
3. Jr-Yu Chen, Fu-Ming Pan, Li Chang, An-Thung Cho, and Kuei-Jung Chao, “Thermal stability of trimethylsilylated mesoporous silica thin films as the ultralow- k dielectric for copper interconnects,” *J. Vac. Sci. Technol. B*, **23**, 2034 (2005).
4. An-Thung Cho, Fu-Ming Pan, Kuei-Jung Chao, P. H. Liu, and Jr-Yu Chen, “The preparation of mesoporous silica ultralow- k film using ozone ashing treatment,” *Thin Solid Films*, **483**, 283 (2005).
5. Jr-Yu Chen, Fu-Ming Pan, Da-Xien Lin, An-Thung Cho, Kuei-Jung Chao, and Li Chang, “Effect of trimethylsilylation on the film stress of mesoporous silica ultralow- k film stacks,” *Electrochem. Solid-State Lett.*, **9**, G215 (2006).

● 研討會論文

1. Jr-Yu Chen, Fu-Ming Pan, An-Thung Cho, Bo-Wei Wu, Tzeng-Guang Tsai, Li Chang, Chia-Min Yang, and Kuei-Jung Chao, “Microstructure and mechanical properties of surfactant templated nanoporous silica thin films,” presented in 2002 International Electron Devices and Materials Symposium, December, 2002, National Taiwan University, Taipei, Taiwan, R.O.C.
2. Jr-Yu Chen, Fu-Ming Pan, An-Thung Cho, Li Chang, and Kuei-Jung Chao, “Thermal and

electrical stabilities of molecularly templated nanoporous silica thin films,” presented in 2003 Electron Devices and Materials Symposium, November, 2003, National Taiwan Ocean University, Jilong, Taiwan, R.O.C.

3. An-Thung Cho, Fu-Ming Pan, Jr-Yu Chen, Li Chang, Tzeng-Guang Tsai, and Kuei-Jung Chao, “Dry etching of nanoporous silica thin films as an ultralow- k dielectric for sub-100 nm technologies,” presented in Symposium on Nano Device Technology 2003, May, 2003, National Chiaotung University, Hsinchu, Taiwan, R.O.C.
4. Chin-Wei Yen, An-Thung Cho, Fu-Ming Pan, H. Y. Hwang, Jr-Yu Chen, and Kuei-Jung Chao, “X-ray reflectivity and mechanical properties of different microstructure of nanoporous silica low- k films,” presented in Symposium on Nano Device Technology 2005, May, 2005, National Chiaotung University, Hsinchu, Taiwan, R.O.C.

科技研討會議經歷

- 2002年國際電子元件暨材料研討會，2002年12月於台灣台北台灣大學（英語口頭發表）
2002 International Electron Devices and Materials Symposium, December, 2002, National Taiwan University, Taipei, Taiwan, R.O.C. (Oral in English).
- 2003年奈米元件技術研討會，2003年5月於台灣新竹交通大學（口頭發表）
Symposium on Nano Device Technology 2003, May, 2003, National Chiaotung University, Hsinchu, Taiwan, R.O.C. (Oral).
- 2003年電子元件暨材料研討會，2003年11月於台灣基隆海洋大學（口頭發表）
2003 Electron Devices and Materials Symposium, November, 2003, National Taiwan Ocean University, Jilong, Taiwan, R.O.C. (Oral).
- 2004年材料研究協會之春季研討會，2003年4月於美國加州舊金山市（海報發表）
2004 Materials Research Society Spring Meeting, April, 2004, San Francisco, C.A., U.S.A. (Poster).
- 2005年奈米元件技術研討會，2005年5月於台灣新竹交通大學（口頭發表）
Symposium on Nano Device Technology 2005, May, 2005, National Chiaotung University, Hsinchu, Taiwan, R.O.C. (Oral).